An X-ray study of cluster vicinities and observational constraints on the warm-hot intergalactic medium

Yoh Takei

Department of Physics, Graduate School of Science,
The University of Tokyo

Institute of Space and Astronautical Science,
Japan Aerospace Exploration Agency

Dec 20, 2005
revised on Feb 3, 2006

Abstract

A large amount (30–50%) of baryons in the universe is believed to reside in the warm-hot intergalactic medium (WHIM) with temperature $T = 10^{5-7}$ K and hydrogen density $n_{\rm H} = 10^{-6}$–10^{-4} cm^{-3}. We present X-ray observations of the WHIM in three cluster vicinities: the Coma cluster, the Virgo cluster and A2218. A bright quasar exists behind the Virgo and Coma cluster. We observed these two clusters with *XMM-Newton* since it has a capability for both fine spectroscopy of a point source with grating spectrometers and imaging spectroscopy of diffuse emission with CCD cameras. On the other hand, we observed A2218 with *Suzaku* because it equips a CCD camera with much better energy resolution than those onboard *XMM-Newton* below 1 keV, where the emission lines from the warm-gas reside.

We detected a Ne IX absorption line (2.7σ) in the Coma vicinity, as well as weak O VII, O VIII and Ne X lines. The combined significance was 3.0σ. We also detected a Ne IX emission line with 3.4σ significance. Since these ions exist in thermal plasma of $T = (2-4)\times 10^6$ K, our results suggest the detection of the WHIM. Combining absorption and emission with an assumption of uniform distribution, we determined the column density $N_{\rm NeIX}$ of the absorption line, temperature kT, $Z\ EM$, where Z is the abundance of metals and EM is the emission measure, hydrogen density $n_{\rm H}$ and ZL, where L is the path length, to be $N_{\rm NeIX} = 4.7^{+2.6}_{-2.9} \times 10^{16}$ cm^{-2}, $kT \sim 0.28$ keV (0.17–0.51 keV), $Z\ EM = 4.1 \pm 2.0 \times 10^{15}$ cm^{-5} $Z_{\rm ISM}$, $n_{\rm H} = 0.2-8.0 \times 10^{-5}$ cm^{-3}, and $ZL = 0.7-300$ $Z_{\rm ISM}$ Mpc, where $Z_{\rm ISM}$ is the interstellar abundance in our Galaxy.

In the Virgo vicinity, we detected an O VIII absorption line with 96.4% significance. We also detected soft excess emission from thermal plasma in the spectrum of the cluster vicinity. Although the contribution of Galactic emission in the soft excess is not trivial compared to the Coma case, the parameters of the WHIM were determined assuming all the soft excess is due to the WHIM to be $N_{\rm OVIII} = 6.2^{+3.3}_{-4.4} \times 10^{16}$ cm^{-2}, $kT = 0.21 \pm 0.01$ keV, $Z\ EM = 1.4 \pm 0.2 \times 10^{16}$ cm^{-5} $Z_{\rm ISM}$, $n_{\rm H} = 3.6^{+2.8}_{-0.9} \times 10^{-5}$ cm^{-3} (1σ), and $ZL = 3.1^{+2.3}_{-2.1}$ $Z_{\rm ISM}$ Mpc (1σ).

Although we did not detect clear O VII or O VIII emission lines around A2218, we set tight upper limits on their intensities. From these upper limits we constrained $n_{\rm H}$ of $T \sim 2 \times 10^6$ K to be less than 7.8×10^{-5} cm^{-3}.

A similarity of the determined parameters of the WHIM around the Coma and Virgo clusters suggests that these properties are universal of the WHIM in cluster vicinities. Assuming that all the clusters accompany the WHIM of similar parameters to that in the Coma and Virgo cluster vicinities and assuming a cylindrical distribution of the WHIM, we further estimated the abundance and mass $M_{\rm WHIM}$ of the WHIM of $kT > 0.2$ keV. We obtained $L/R_{\rm WHIM} \lesssim 10$, $L \gtrsim 6$ Mpc, $R_{\rm WHIM} \gtrsim 0.6$ Mpc, $M_{\rm WHIM} \gtrsim 9.3 \times 10^{12}$ $M_\odot$, $\Omega_{\rm WHIM} \gtrsim 0.02\%$, and $Z \gtrsim 0.1$ $Z_{\rm ISM}$, where $R_{\rm WHIM}$ is a radius of a cylindrical region of the WHIM. These values are consistent with the predictions of numerical simulations.

Acknowledgment

I have been supported by many people in the five years for this work. The first person I would like to thank is my supervisor Prof. Kazuhisa Mitsuda, who has given me a lot of advice and knowledge about astrophysics and physical point of view. I feel that I could not learn so much without his teaching. He is very strict about treatment of data for deriving scientifically interesting and correct results at the most, from which I learned much about the attitude to research.

Dr. Ryuichi Fujimoto, a professor assistant, taught me a basic of analysis of X-ray astrophysics data and carefully reviewed the manuscript of not only this thesis but also other papers for journals. I would like to express my gratitude for his invaluable help. He also encouraged me whenever I was depressed. I was really helped with his gentle words and suggestions.

I am grateful to Prof. J. Patrick Henry. He gave me a lot of advice and suggestions about a main part of this thesis, as if he had been a direct supervisor of me. Also he is the principal investigator of some of the observation proposals. I could not even analyzed the data without his attractive proposal.

Prof. Takaya Ohashi and associate professor Noriko Y. Yamasaki gave me suggestions about observation using Suzaku and also gave me an opportunity to analyze it very soon. Their comments on my work were always useful. I appreciate their help and kindness very much. Professor Dan McCammon has knowledge and experience over many fields: interstellar medium, X-ray emission mechanisms, X-ray spectrometers, and so on. He gave me many useful comments, suggestions and encouragements. I would like to express my appreciation for his assistance.

This work is based on a collaboration with many scientists. The discussion with Drs. Takayuki Tamura, Alexis Finoguenov and Prof. Ulrich G. Briel in regards to Coma cluster outskirts was very fruitful and helped the discussion of this work. The chapter of Virgo cluster vicinity could not be written without suggestions by Drs. Ryo Shibata, Naomi Ota, Michael D. Audley, Richard L. Kelley and Caroline A. Kilbourne. I would like to thank them.

Secretaries of ISAS/JAXA and U. Tokyo, Ms. Sachiko Itoh and Ms. Kuniko Kono always tried hard when I needed their help. I could not travel abroad and might not be able to graduate without their kindness. Sweet hand-cooked cake by Itoh-san filled my heart with ease and peace when I was exhausted. I really appreciate their tenderness and kindness.

I thank colleagues and friends at ISAS: Tai Oshima, Yuichiro Ezoe, Kazuo Futamoto, Ryo Iizuka, Takefumi Mitani, Taro Ichitsubo, Kiyonori Yoshida, Kensuke Masui, Tomotaka Yoshino, Akihiro Tsuchiya, Shunsuke Kimura, Masaki Koshiishi, Toshishige Hagihara. All discussions, talks, having a meal with them were very joyful. I enjoyed them very much. I hope we are friends even after graduation. Other people at ISAS/JAXA also helped and pleased me. I would like to say thank you to all of them.

Finally, I acknowledge my families. I am very grateful to my wife, Mieko Takei, for her tenderness and patience during PhD period. My parents are always available when I need their help. I cannot be what I am without their help and discipline.

Contents

Abbreviation

β:	β parameter of the β model
δ:	Overdensity relative to the mean baryon density; $\delta \equiv \rho_{\rm b}/\overline{\rho_{\rm b}} = n_{\rm H}/\overline{n_{\rm H}} = \rho/\overline{\rho_{\rm m}}$
ϵ:	Plasma volume emissivity
$\Lambda(T,Z)$:	Cooling function as a function of the temperature and abundance of the gas
$\Lambda'_{\rm line}(T)$:	Cooling function of a single emission line normalized to unit Z; $\sum Z\Lambda'_{\rm line}(T) = \Lambda(T,Z)$ when line emission dominates over the continuum
ΛCDM :	Cold dark matter model with a cosmological constant
$\sigma_{\rm gal}$:	Standard deviation of the galaxies in clusters converted to redshift in the observed frame.
$\sigma_{\rm align}$:	Net cross section of an aligned filament.
Ω_Λ:	Vacuum energy density, i.e., cosmological constant
$\Omega_{\rm b}$:	Baryon density of the Universe; $0.0457 \pm 0.0018 h_{70}^{-2}$ (*WMAP* estimate)
$\Omega_{\rm cluster}$:	Baryon density residing in the clusters of galaxies of the Universe
$\Omega_{\rm m}$:	Matter density of the Universe $0.276^{+0.016}_{-0.018} h_{70}^{-2}$ (*WMAP* estimate)
$\Omega_{\rm total}$:	Total density of the Universe; a flat Universe corresponds to $\Omega_{\rm total} = 1$; 1.02 ± 0.02 (*WMAP* estimate)
$\Omega_{\rm WHIM}$:	Baryon density residing in the WHIM of the Universe
$\rho_{\rm crit}$:	Critical density of the universe; $\rho_{\rm crit} \equiv 3H(z)^2/8\pi G = 9.21 \times 10^{-30}\ h_{70}^2 (1+z)^3$ g cm^{-3}
$\overline{\rho_{\rm b}}$:	Mean baryon density; $\overline{\rho_{\rm b}} \equiv \Omega_{\rm b}\rho_{\rm crit} = 4.13 \times 10^{-31}(1+z)^3$ g cm^{-3}
$\overline{\rho_{\rm m}}$:	Mean mass density; $\overline{\rho_{\rm m}} \equiv \Omega_{\rm m}\rho_{\rm crit} = 2.54 \times 10^{-30}(1+z)^3$ g cm^{-3}
BI:	Back-illuminated CCD of XIS onboard *Suzaku*
c:	Light speed; 3.00×10^8 m s^{-1}
COR:	Cut off rigidity of the cosmic rays
CTE:	Charge transfer efficiency of a pixel of a CCD
CTI:	Charge transfer inefficiency of a pixel of a CCD
CXB:	Cosmic X-ray background
Dec:	Declination
e:	Elementary charge; 1.60×10^{-19} C
EA:	Effective area of a detector

EEF:	Encircled energy function of an X-ray telescope.
EM:	Emission measure of the absorption line; $EM = \int n_\mathrm{e} n_\mathrm{H}\, dL$
EPIC:	European Photon Imaging Camera onboard *XMM-Newton*
EUV:	Extreme ultraviolet
EUVE:	Extreme ultraviolet explorer
EW :	Equivalent width of an absorption
FI:	Front-illuminated CCDs of XIS onboard *Suzaku*
f_ion:	Ionization fraction of an ion
f_os:	Oscillator strength of an absorption line
FOV:	Field of view of a telescope
FUSE:	Far Ultraviolet Spectroscopic Explorer
f_vol:	Volume filling factor of a material
G:	Gravitational constant; 6.67×10^{-11} Nm^2 kg^{-2}
h:	Planck constant; 6.63×10^{-34} Js
h_{100}:	Hubble constant normalized to 100 km s^{-1} Mpc^{-1}
h_{70}:	Hubble constant normalized to 70 km s^{-1} Mpc^{-1}
H_0:	Hubble constant at $z = 0$; $H_0 = 71^{+4}_{-3}$ km s^{-1} Mpc^{-1} (*WMAP* estimate)
$H(z)$:	Hubble constant at redshift z; $H(z) = H_0(1+z)^3$ in a flat universe
HEW:	Half energy width of a telescope.
HPD:	Half power diameter of a telescope
HST:	Hubble Space Telescope
HXD:	Hard X-ray detector onboard *Suzaku*
I:	Surface brightness of emission or an emission line
ICM:	Intracluster medium
ISM:	Interstellar medium
L:	Path length of the WHIM in cluster vicinities
L_X:	Luminosity of an emission line
LHB:	Local hot bubble
LETG:	Low energy transmission grating onboard *Chandra*
$M_\odot$:	Solar mass; $M_\odot = 1.99 \times 10^{33}$ g
M_Abell:	The mass of the hot gas in the cluster within the Abell radius $2.1 h_{70}^{-1}$ Mpc
m_e:	Electron mass; 9.11×10^{-28} g
M_hot:	The mass of the hot gas in the cluster
m_p:	Proton mass; 1.66×10^{-24} g
M_total:	The mass of the total (dark matter and baryons) in the cluster
MWH:	Milky-way halo
M_WHIM:	The mass of the WHIM around a cluster
n_cluster:	Number density of clusters

$n_{\rm e}$:	Electron density
$N_{\rm H}$:	Hydrogen column density
$n_{\rm H}$:	Hydrogen density
$\overline{n_{\rm H}}$:	Mean hydrogen number density; $\overline{n_{\rm H}} \equiv X\overline{\rho_{\rm m}}/m_{\rm p} = 1.77\times10^{-7}(1+z)^3$ cm^{-3}
$N_{\rm ion}$:	Column density of an ion
OBF:	Optical blocking filter installed between a telescope and a CCD
PSF:	Point spread function of a telescope
r_{200}:	Radius within which the average density is 200 times $\rho_{\rm crit}$.
RA:	Right ascension
RASS:	*ROSAT* All-Sky Survey
$R_{\rm C}$:	Core radius of a β profile
RGS:	Reflection grating spectrometer onboard *XMM-Newton*
$R_{\rm WHIM}$:	The radius of a cylindrical region that contains the WHIM
$r_{\rm vir}$:	The virial radius of a cluster
$r_{\rm QSO}$:	Projected distance of the quasar from a cluster center
SAA:	South Atlantic anomaly
UV:	Ultraviolet
WMAP:	Wilkinson Microwave Anisotropy Probe
WHIM:	Warm-hot intergalactic medium
X:	Hydrogen-to-baryon mass ratio; 0.71
XIS:	X-ray imaging spectrometer; the CCDs onboard *Suzaku*
XMM:	An European X-ray satellite; X-ray Multi-Mirror Mission (*XMM-Newton*)
XRT:	X-ray telescope
Z:	Metal abundance relative to H
$Z_\odot$:	Metal abundance of the Sun relative to H determined by Anders & Grevesse (1989); widely used in X-ray astronomy community; 8.51×10^{-4} for O, 1.23×10^{-4} for Ne, and 4.68×10^{-5} for Fe as $Z_{\rm ISM}$.
$Z_{\rm ISM}$:	Metal abundance relative to H, which we adopted in this thesis; 4.57×10^{-4} for O, 1.87×10^{-4} for Ne, and 2.82×10^{-5} for Fe as $Z_{\rm ISM}$.
$Z_{\rm Mewe}$:	Metal abundance relative to H used in Mewe et al. (1985).
z:	Redshift

Chapter 1

Introduction

Recent observations of distant universe show that the ΛCDM model of a flat universe represents the universe well (e.g., Spergel et al., 2003). The model expects a hierarchical clustering scenario of the structure formation of the universe. However, our observational knowledge of the structure of the local universe is so limited that about half of the baryons have not yet observed, i.e., missing. Where is the baryons? How is the real structure of the local universe? Numerical simulations based on the ΛCDM model predicted answers of such questions; a significant (30–50%) amount of baryons in their simulations resides in a form of gas in 'warm-hot' phase ($T = 10^{5-7}$ K), which is hard to detect with currently existent detectors (e.g., Cen & Ostriker, 1999; Davé et al., 2001; Chen et al., 2003).

This warm-hot gas, whose density is 10^{-6}–10^{-4} cm^{-3}, is called warm-hot intergalactic medium (WHIM). The WHIM may be detected via emission or absorption lines of highly ionized elements in the X-ray spectrum. So far, there are only two significant detections of the WHIM (Nicastro et al., 2005a); they detected absorption lines in the spectra of a blazars in strong outbursts. Possible emission from the WHIM was also reported. However, no WHIM was detected via both emission and absorption.

In this thesis, we searched three cluster vicinities for the WHIM associated with the cluster to make a breakthrough. The most prominent advantage of our strategy is that we can constrain the density and geometry by combining absorption and emission lines from the same ion. We present the properties of the WHIM in cluster vicinities derived by these observations. We also discuss the contribution on baryon budget of the WHIM associated with the clusters, assuming that the WHIM we studied is typical for other cluster vicinities.

This thesis is organized in the following order. In the next chapter, Chapter 2, we will review the current knowledge of the hierarchical large-scale structure formation and past study of the WHIM by observations and numerical simulations. We will describe our observation strategy and the targets in Chapter 3. Chapter 4 is devoted to the description of the instruments onboard the satellites we used: *XMM-Newton* and *Suzaku*. Chapters 5, 6 and 7 show observational results and the physical properties of the WHIM in the vicinities of the Coma cluster, the Virgo cluster, and A2218, respectively. We will discuss in Chapter 8 the properties of the WHIM in cluster vicinities combining the results of the three clusters. Finally, we will show the conclusion of this thesis in Chapter 9.

We use $H_0 = 70$ km s^{-1}, $\Omega_\mathrm{m} = 0.3$, and $\Omega_\Lambda = 0.7$ throughout the thesis. Errors are quoted at 90% confidence level in the text and tables, while they are at 68% (1σ) confidence level in the figures, unless otherwise described.

Chapter 2

Review

2.1 Structure and constituents of the universe

2.1.1 ΛCDM model as a picture of the universe

It has been known for the past two decades that the universe has a hierarchical structure: stars gather to be a galaxy ($\sim$ 100 kpc scale), galaxies make an ensemble to be a cluster of galaxies ($\sim$ 1 Mpc scale), and clusters of galaxies make a large-scale structures such as superclusters and voids ($\sim$ 10 Mpc scale). After the first discoveries of these structures with optical light, our knowledge of structures has been enriched with observations at various wavelengths. In particular, X-ray observations of clusters of galaxies revealed the existence of large amounts of hot gas whose mass is $\sim$ 10 times that of stars. The temperature of the X-ray gas also suggested non-baryonic matter (dark matter) whose mass is $\sim$ 10 times the baryonic mass. This means that we had seen only a few percent of the mass in optical light, and that only $\sim$ 10% of the matter is seen even with light of any wavelength.

By observing the distant universe, it was found that most energy of the universe is not in baryons nor dark matter. The combination of observations of Type Ia supernovae, cosmic microwave background anisotropy, and the gas mass fraction inside clusters of galaxies provided evidence for a flat accelerating universe dominated by dark energy, or a cosmological constant. This universe is represented by "ΛCDM model". This model contains cold dark matter, dark energy and baryonic matter, and is parameterized by Hubble constant H_0 (or normalized Hubble constant such as $h_{100} \equiv H_0/100$ km s^{-1} Mpc^{-1} or $h_{70} \equiv H_0/70$ km s^{-1} Mpc^{-1}), total density $\Omega_{\rm total}$, matter density $\Omega_{\rm m}$, baryon density $\Omega_{\rm b}$ and vacuum energy density Ω_Λ. Recent cosmic microwave background (CMB) observations of Wilkinson Microwave Anisotropy Probe (*WMAP*) have showed that the ΛCDM model of a flat universe explains the observations well. Combined with other observations, *WMAP* determined many cosmological parameters: $h_{100} = 0.71^{+0.04}_{-0.03}$, $\Omega_{\rm total} = 1.02 \pm 0.02$, $\Omega_{\rm m} h_{70}^2 = 0.276^{+0.016}_{-0.018}$, and $\Omega_{\rm b} h_{70}^2 = 0.0457 \pm 0.0018$ (Spergel et al., 2003).

Here we define some values which represent the mean densities of the universe assuming a flat universe and Ω values. The critical density of the universe $\rho_{\rm crit}$ is defined as

$$\rho_{\rm crit} \equiv \frac{3H(z)^2}{8\pi G} = \frac{3H_0^2\ (1+z)^3}{8\pi G} = 9.21 \times 10^{-30}\ h_{70}^2 (1+z)^3\ {\rm g\ cm^{-1}}, \tag{2.1}$$

where $H(z)$ is the Hubble constant at redshift z and G is the gravitational constant. Mean

Table 2.1: The Baryon Budget observed at $z \simeq 0$ (Fukugita et al., 1998)

	Component	Central	Maximum	Minimum	Grade[a]
1	stars in spheroids	$0.0026h_{70}^{-1}$	$0.0043h_{70}^{-1}$	$0.0014h_{70}^{-1}$	A
2	stars in disks	$0.00086h_{70}^{-1}$	$0.00129h_{70}^{-1}$	$0.00051h_{70}^{-1}$	A–
3	stars in irregulars	$0.000069h_{70}^{-1}$	$0.000116h_{70}^{-1}$	$0.000033h_{70}^{-1}$	B
4	neutral atomic gas	$0.00033h_{70}^{-1}$	$0.00041h_{70}^{-1}$	$0.00025h_{70}^{-1}$	A
5	molecular gas	$0.00030h_{70}^{-1}$	$0.00037h_{70}^{-1}$	$0.00023h_{70}^{-1}$	A–
6	plasma in clusters	$0.0026h_{70}^{-1.5}$	$0.0044h_{70}^{-1.5}$	$0.0014h_{70}^{-1.5}$	A
7a	warm plasma in groups	$0.0056h_{70}^{-1.5}$	$0.0115h_{70}^{-1.5}$	$0.0029h_{70}^{-1.5}$	B
7b	cool plasma	$0.002h_{70}^{-1}$	$0.003h_{70}^{-1}$	$0.0007h_{70}^{-1}$	C
$7'$[b]	plasma in groups	$0.014h_{70}^{-1}$	$0.030h_{70}^{-1}$	$0.0072h_{70}^{-1}$	B
8	sum (at $h_{100} = 0.7$ and $z \simeq 0$)	0.021	0.041	0.007	

[a]: Confidence of evaluation from A (robust) to C (highly uncertain).
[b]: Scaling from the plasma mass in clusters; not an observed value.

mass density, mean baryon density and mean hydrogen (number) density are represented as

$$\overline{\rho_{\rm m}} \equiv \Omega_{\rm m}\ \rho_{\rm crit} = 2.54 \times 10^{-30}\ (1+z)^3\ \text{g cm}^{-1}, \tag{2.2}$$

$$\overline{\rho_{\rm b}} \equiv \Omega_{\rm b}\ \rho_{\rm crit} = 4.13 \times 10^{-31}\ (1+z)^3\ \text{g cm}^{-1}, \tag{2.3}$$

$$\overline{n_{\rm H}} \equiv \frac{X\ \overline{\rho_{\rm m}}}{m_{\rm p}} = 1.77 \times 10^{-7}\ (1+z)^3\ \text{cm}^{-3}, \tag{2.4}$$

respectively, where $X = 0.71$ is the hydrogen-to-baryon mass ratio and $m_{\rm p}$ is the proton mass. We also define overdensity δ relative to the mean baryon density as

$$\delta \equiv \rho_{\rm b}/\overline{\rho_{\rm b}} = n_{\rm H}/\overline{n_{\rm H}} = \rho/\overline{\rho_{\rm m}}, \tag{2.5}$$

in which all of the definitions would represent the same value in this thesis. Note that 'over density' is defined as $\rho/\rho_{\rm crit}$ in some references, which is a little confusing.

2.1.2 Baryon content in the universe

WMAP and other recent observations show the universe dominated by dark matter and dark energy, whose natures are completely unknown. Moreover, there remain unknowns in even baryonic matter. Not only *WMAP*, but also other independent theory and measurements indicate similar baryon amounts in the universe: $\Omega_{\rm b}h_{70}^2 \sim 0.045$. Primordial deuterium-to-hydrogen ratio and Big Bang nucleosynthesis theory suggest $\Omega_{\rm b}h_{70}^2 = 0.041 \pm 0.004$ (Burles et al., 2001), and Lyα forest absorption at high redshift ($z \sim 3$) shows the baryon content is $\Omega_{\rm b}h_{70}^2 > 0.043$ (Rauch et al., 1997). In contrast, the baryon budget observed in the local universe appears far lower than these indications (Fukugita et al., 1998; Bristow & Phillipps, 1994; Persic & Salucci, 1992). A summary of the observed local baryon budget by Fukugita et al. (1998) is shown in Table 2.1. Note that $7'$ in the table shows the calculated values by scaling from the plasma mass in the clusters of galaxies. Therefore, the sum of the baryons that were observed is about half of that obtained with *WMAP* or other observations of distant universe. Even the maximum of the values in Table 2.1 do not reach the *WMAP* value. This discrepancy has been called "missing baryon problem".

2.1.3 Hierarchical structure formation

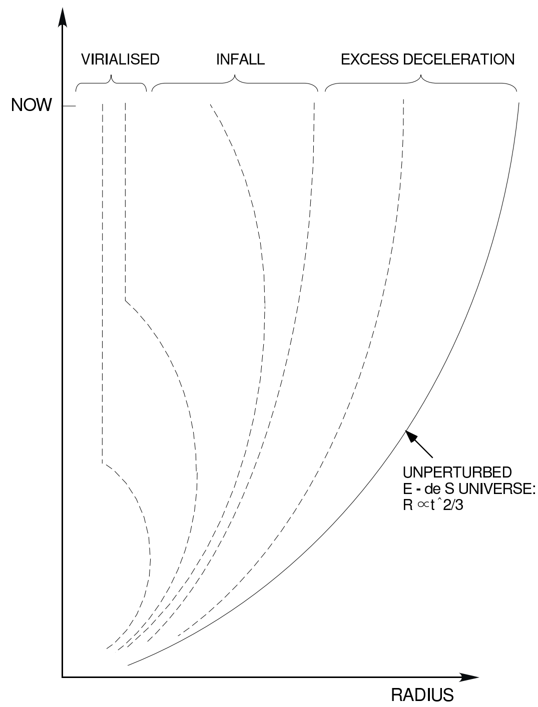

Figure 2.1: The dynamics of overdense spheres in the expanding universe. Larger initial overdensity results in earlier infall and virialization (Rees, 1992).

At present, a hierarchical clustering scenario is widely supported, since it is naturally expected from ΛCDM model. In this scenario, small systems such as stars were first formed from small density perturbations at the early universe, and then they condensed into larger structures through gravitational interactions. Figure 2.1 shows the dynamics of overdense spheres. A system would expand spherically without self-gravitation in an acceralating universe, while gravity stops the expansion and collapses it into a virialized system with sufficiently high density. A system with larger initial overdensity collapses earlier into smaller virialized system. The clusters of galaxies, which are the largest virialized systems, have $\rho/\rho_{\rm crit} > 200$ or $\delta > 1500$.

In order to understand the large-scale structure and its formation history, many numerical simulations have been intensively carried out based on the ΛCDM model (e.g., Cen & Ostriker, 1999; Davé et al., 2001; Chen et al., 2003). The most amazing result of these simulations is that all of them predicted a significant amount of mass in a form of gas in 'warm-hot' phase ($T = 10^{5-7}$ K) at $z = 0$. Figure 2.2 shows the evolution of gases of four temperature ranges. While warm ($T < 10^5$ K) gas dominates in volume fraction, its mass decreases with time and is dominated at current epoch by warm-hot ($T = 10^{5-7}$ K) gas; the warm-hot gas contains 30–40% of total baryons. The low density of the warm-hot gas and low sensitivity of detectors to gas of this temperature makes its detection very difficult; the gas is 'missing'. Thus, it is naturally thought that the 'missing baryons' must reside in the

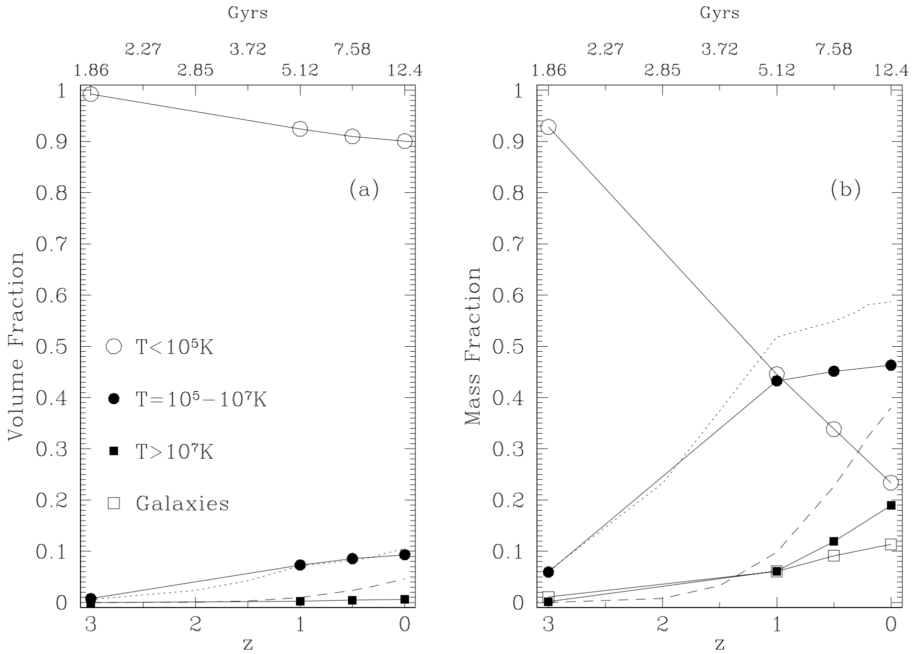

Figure 2

Figure 2.2: Evolution of warm ($T < 10^5$ K; open circle ○), warm-hot ($T = 10^{5-7}$ K; filled circle •), hot ($T > 10^7$; open square □) and cold gas (condensed into stellar objects; filled square ■) (Cen & Ostriker, 1999). (a) Volume fractions, and (b) mass fractions.

warm-hot gas, the so-called Warm-Hot Intergalactic Medium (WHIM).

The simulations also give predictions of the distribution of matter. One example of simulated WHIM distributions is shown in Figure 2.3. The whim resides in filamentary shapes that are associated with structures of the non-baryonic dark matter. The distributions of dark matter, the WHIM, hot gas and galaxies are compared in Figure 2.4. All the distributions are similar, and the WHIM best represents the dark matter distribution. Therefore, a study of the WHIM is important for the understanding of large-scale structure formation, as well as for solving the missing baryon problem.

2.2 Warm-hot intergalactic medium

[

2.2.1 Physical properties predicted from numerical simulations

The properties of the WHIM are poorly known from observations and hence are based on the predictions of numerical simulations. The WHIM has a temperature of $T = 10^{5-7}$ K, and comprises 30–40% of the baryonic mass of the universe. Its density is $n_{\rm H} \sim 10^{-(4-5)}$ cm^{-3} around clusters and $n_{\rm H} \sim 10^{-6}$ cm^{-3} in other regions along filaments. These properties are well reproduced in several independent simulations (e.g., Cen & Ostriker, 1999; Davé

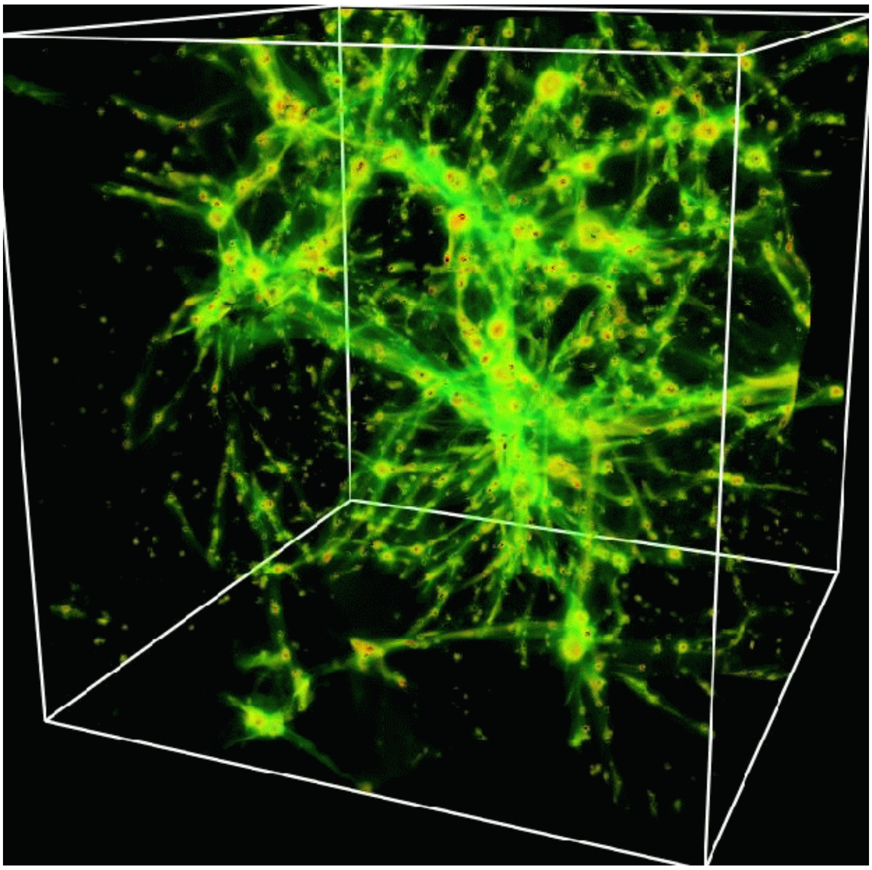

Figure 2.3: A simulated distribution of the WHIM in $(100h_{100}^{-1}$ Mpc$)^3$ cube. Green represents overdensity $\delta \sim 10$, while red shows $\delta \sim 10^4$. (Davé et al., 2001).

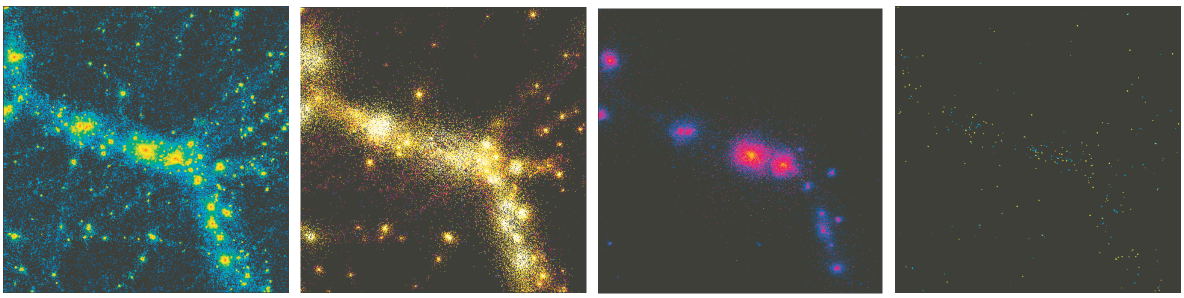

Figure 2.4: Simulated distributions of matter in a $(15h_{100}^{-1}$ Mpc$)^2$ region (Yoshikawa et al,, private communication). From left to right, the distributions of non-baryonic dark matter, WHIM, hot gas and galaxies are shown.

et al., 2001), since these characteristics are mostly determined by gravitational interaction processes. From the density and temperature distribution of baryonic mass, column densities of various ion features along a typical line of sight can be predicted (Davé et al., 2001; Chen et al., 2003; Fang et al., 2002). Figure 2.5 displays one example in Fang et al. (2002). The maximum column densities of O VII and O VIII are $\sim 10^{17}$ cm^{-2}.

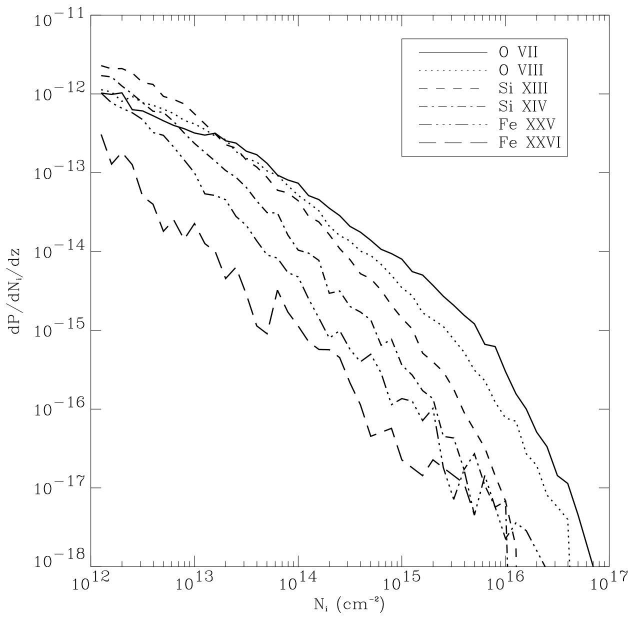

Figure 2.5: The number of absorption systems along the line of sight with a column density between $N_{\rm ion}$ and $N_{\rm i} + dN_{\rm i}$ per unit redshift (Fang et al., 2002)

.

In contrast to the good agreement of the mass fraction and density of the WHIM between simulations, there is little consensus in metal abundance distribution or temperature gradients in proximities of clusters, because they are too much affected by interactions with galaxies and clusters of galaxies: the output of thermal energy and photons from supernovae and active galactic nuclei, mass ejection and metal pollution due to galactic winds, etc. The abundance of metals relative to hydrogen (Z) is expected to be similar to or less than that in clusters of galaxies, i.e., $Z \lesssim 0.3\ Z_\odot$, where $Z_\odot$ is the solar metallicity, but there are still uncertainties of a factor of two or three. In addition to the difficulty of understanding temperatures around the clusters, Yoshida et al. (2005) pointed out a possibility of a different electron and ion temperatures.

2.2.2 Observation history

2.2.2.1 Absorption due to the ions in the WHIM

The very low density of the WHIM makes its detection difficult in emission, since the emission strength is proportional to square of the density. Therefore, most searches for the WHIM has been attempted using absorption of the highly ionized ions in the WHIM, by observing distant ($z \gtrsim 0.1$) bright sources. The equivalent width EW of the absorption line due to an ion with column density $N_{\rm ion}$ is written as

$$EW = \frac{\pi h e^2}{m_{\rm e} c(1+z)} f_{\rm os} N_{\rm ion} = 1.10\ {\rm eV}\ \frac{f_{\rm os}}{1+z} \left(\frac{N_{\rm ion}}{10^{16}\ {\rm cm}^{-2}} \right) \tag{2.6}$$

in the case of no saturation (i.e., small column density), where $m_{\rm e}$ is the electron mass, c is the light speed, h is the Planck constant, e is the elementary charge and $f_{\rm os}$ is the oscillator strength of the absorption line (Sarazin, 1989). Thus, a filament that contains ions of $N_{\rm ion} \gtrsim 10^{16}$ cm^{-2} can make an absorption of $EW \gtrsim 1$ eV, which can be detected by existing spectrometers onboard *Chandra*, *XMM-Newton*, *Hubble Space Telescope (HST)* and *Far Ultraviolet Spectroscopic Explorer (FUSE)* satellites.

Because of their high abundance, highly ionized O, Ne, C, N, and Fe are detection candidates via resonance lines. The ionization fraction $f_{\rm ion}$ of a gas in ionization equilibrium is determined by its temperature as shown in Figure 2.6. The WHIM with $T \sim 10^{5-5.5}$ K can be observed using absorption of O VI, N V or C IV lines, which are in ultraviolet (UV) range, while X-ray observations are sensitive to the WHIM with $T \sim 10^{6-7}$ K via O VII, O VIII, Ne IX, Ne X and Fe XVII lines.

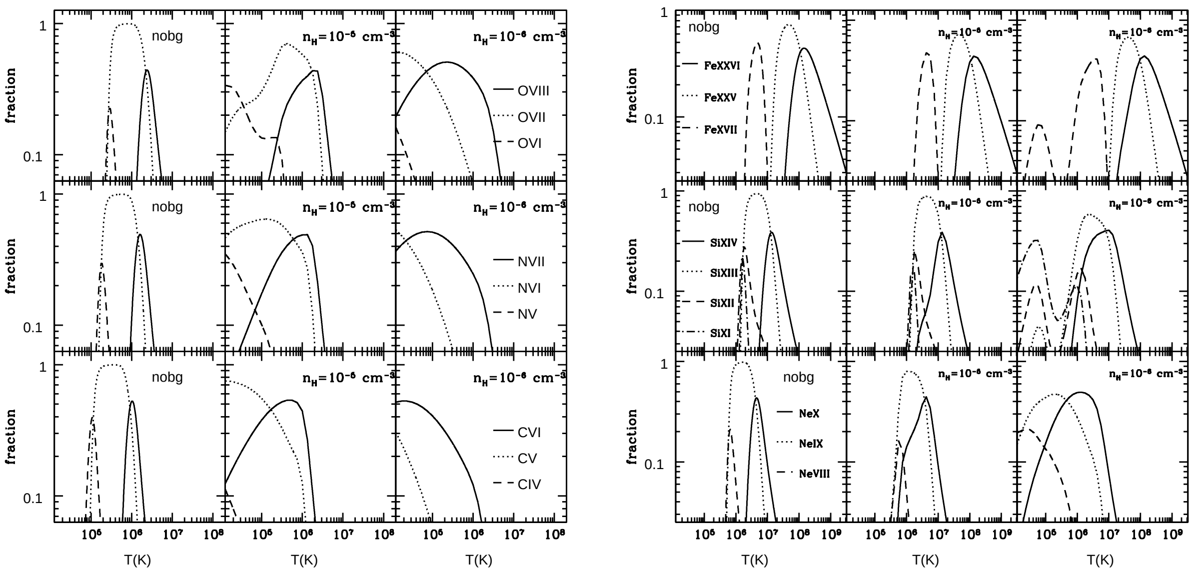

Figure 2.6: Ionization fraction vs. temperature (Chen et al., 2003). In the left figure, O (top), N (middle) and C (bottom) are shown, while Fe (top), Si (middle) and Ne (bottom) are on the right. From left to right, the cases of collisional ionization equilibrium, photo- and collisional ionization equilibrium with $n_{\rm H} = 10^{-5}$ cm^{-3}, and photo- and collisional ionization equilibrium with $n_{\rm H} = 10^{-6}$ cm^{-3} are shown, for each species.

The first detection of the WHIM was through redshifted O VI doublets (1091.926 and 1037.617 Å) at $z = 0.22497, 0.22637, 0.24531$, and 0.26659 in a spectrum of QSO H1821+643 utilizing a UV spectrometer with a very high wavelength resolution onboard *FUSE* satellite (Tripp et al., 2000). The column densities of the O VI were $(2-20)\times 10^{13}$ cm^{-2}. Since then, over 40 systems with an O VI absorber have been detected using *FUSE* and *HST*. Danforth & Shull (2005) constrained the baryon density of the WHIM with $T = 10^{5-6}$ K to be at least

$$\Omega_{\rm b}(T = 10^{5-6}\ {\rm K}) = (0.0022 \pm 0.0003)\ h_{70}^{-1} \left(\frac{Z_{\rm O}}{0.1 Z_\odot}\right)^{-1} \left(\frac{f_{\rm ion\ OVI}}{0.2}\right)^{-1} \tag{2.7}$$

from the number of absorbers per unit redshift, assuming an O abundance $Z_{\rm O}$, and O VI ionization fraction $f_{\rm ion\ OVI}$. This density corresponds to $4.8 \pm 0.9\%$ of the total baryonic mass.

Hotter WHIM with a temperature of $T = 10^{6-7}$ K is more difficult to detect due to a poorer wavelength resolution of X-ray spectrometers relative to UV ones. Its study is now just at a starting point. Although detections of O VII, O VIII and Ne IX absorptions possibly due to the WHIM were claimed several years ago by Nicastro et al. (2002) and Fang et al. (2002) in spectra of blazars, their redshift were consistent with zero, and hence hard to distinguish from Galactic warm-hot gas. Recent studies (Futamoto et al., 2004; Yao & Wang, 2005) actually show the existence of sufficient Galactic warm-hot gas to explain almost all $z = 0$ absorption columns.

The only detection so far of $z > 0$ absorption for which $> 3\,\sigma$ significance was claimed was O VII and C V Kα resonance lines in spectra of Mkn 421 and 1ES 1028+511 observed with grating spectrometers (Low Energy Transmission Grating Spectrometer; LETGS) onboard *Chandra* (Nicastro et al., 2005b,a,c). The observations were performed when these two blazars were in strong outbursts; they were then among the brightest objects in the sky. Although they observed absorption lines from gases of $N_{\rm ion} \sim 10^{15}$ cm^{-2}, detections of ions with $N_{\rm ion} \lesssim 10^{16}$ cm^{-2} are impossible except with such extraordinarily bright sources. Figure 2.7 shows two figures of Nicastro et al. (2005a), one of which is a spectrum of Mkn 421 containing redshifted O VII absorption lines, and the other of which shows the number of O VII absorbers per unit redshift. Nicastro et al. (2005b) estimated the density of the WHIM of $T \sim 1.3 \times 10^6$ K to be

$$\Omega_{\rm b}(T \sim 1.3 \times 10^6 \text{ K}) = (0.027^{+0.038}_{-0.019}) \left(\frac{Z_{\rm O}}{0.1 Z_\odot}\right)^{-1}. \tag{2.8}$$

These UV and X-ray results are consistent with the prediction of numerical simulations within their errors (e.g., Davé et al., 2001). However, after one year from the report of these detections, the signifiacnce of the detection became controversial. The abosrption lines were not confirmed with more statistical observations with RGS spectrometers onboard *XMM-Newton* (Rasmussen et al., 2007). Moreover, Kaastra et al. (2006) re-analyzed the data of Nicastro et al. (2005b) and re-examined the statistical significance using Monte Carlo technique to find that the significance of the lines are at most 94%; since the wavelength range Nicastro et al. (2005b) searched is quite wide compared to the wavelength resolution of LETG, such a significant-looking absorption feature may arise with 6% probability in an *arbitrary* position.

2.2.2.2 Emission from the WHIM

Emission from the WHIM is being investigated despite the observational difficulties. The plasma volume emissivity ϵ, i.e., X-ray radiation energy emitted from a unit volume in a unit time, is given by

$$\epsilon = n_{\rm e}^2 \Lambda(T, Z), \tag{2.9}$$

where $n_{\rm e}$ is the electron number density, and $\Lambda(T, Z)$ is the cooling function as a function of the gas abundance Z and the gas temperature T. The temperature dependence of the cooling function is shown in Figure 2.8. Most of the emission is from characteristic lines of ionized metals such as O, C, N, Ne and Fe below 10^7 K. In the case of line-dominated emission, the cooling function is proportional to Z. Assuming a spatially uniform density, abundance and temperature, the luminosity $L_{\rm X}$ and surface brightness I (in the number of

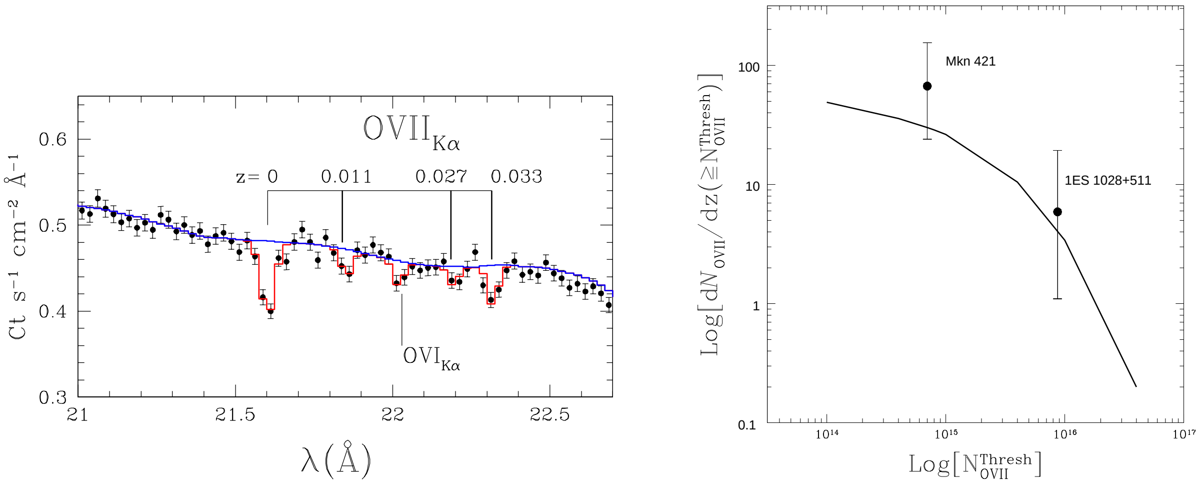

Figure 2.7: Left: a spectrum of Mkn 421 observed with *Chandra* LETGS. Right: cumulative number of O VII WHIM systems per unit redshift as a function of the minimum O VII column density. The solid line is a model predicted by numerical simulation of Fang et al. (2002). Both figures are from Nicastro et al. (2005a).

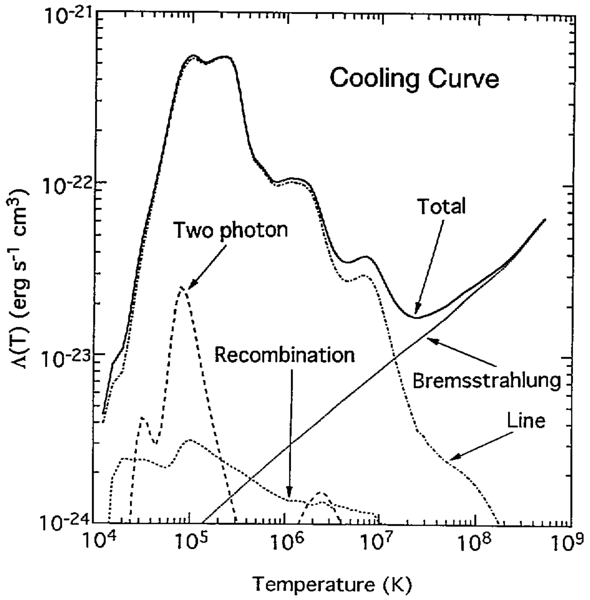

Figure 2.8: Temperature dependence of the cooling function and its components for a optically thin plasma containing cosmic abundance of elements (Gehrels & Williams, 1993)

photons, not energy) of an emission line can be written as

$$L_{\rm X} = \int \epsilon \; dV = EM \;\; S \;\sum Z \;\Lambda'_{\rm line}(T), \;\; \text{and} \tag{2.10}$$

$$I = \frac{EM \;\; Z \;\Lambda'_{\rm line}(T)}{4\pi \; (1+z)^3 E}, \tag{2.11}$$

where S is the geometrical area of the emitting zone, E is the energy of the emission line, $\Lambda'_{\rm line}(T)$ is a cooling function *for a single line* normalized to unit Z, and EM is an emission measure defined as

$$EM = \int n_{\rm e} n_{\rm H} \, dL, \tag{2.12}$$

in which L is the line-of-sight length of the plasma. The sum is taken for every emission line and $\Lambda(T, Z) = \sum Z\Lambda'_{\rm line}(T)$.

The dependence of ϵ on $n_{\rm e}^2$ implies a relatively high detectability near the clusters of galaxies, where the WHIM has the highest density. Since high resolution spectroscopy using grating spectrometers cannot be utilized for diffuse objects, studies of the emission from the WHIM have been investigated using X-ray CCDs and proportional counters.

Before the possible existence of the WHIM was realized, detections of soft emission ($E < 0.3$ keV) around nearby clusters of galaxies had been reported in extreme ultraviolet (EUV) and X-ray band using *Extreme-Ultraviolet Explorer (EUVE)* and *ROSAT* satellites (e.g., Lieu et al., 1996; Lieu et al., 1996; Mittaz et al., 1998). At that time, two interpretations were proposed: thermal emission from warm gas within clusters (Fabian, 1997), and non-thermal inverse-Compton scattering between the cosmic microwave background (CMB) and intracluster relativistic electrons (Hwang, 1997). Either interpretations required, however, unnatural physical conditions for clusters. The former interpretation requires too much heat input to keep the temperature of the warm gas high against radiative cooling, while the latter needs too many cosmic-ray electrons (Bonamente et al., 2002). It is more likely that the soft excess comes from the WHIM around clusters of galaxies.

Kaastra et al. (2003) detected O VII emission lines as well as soft X-ray ($E < 0.5$ keV) excesses in spectra of five clusters of galaxies out of 14 clusters using the much better energy resolution of *XMM-Newton*. This detection supported a thermal origin for the soft excesses. The redshifts of the lines were marginally larger than zero so that their cluster origin is suggested, though the possibility of the Galactic origins was not definitely excluded. Finoguenov et al. (2003) also reported a detection of O VII and O VIII emission lines in spectra of the outskirts of the Coma cluster obtained with CCDs on *XMM-Newton*. They carefully modeled Galactic emission to show that the soft excess was far above the possible maximum of the Galactic model. Furthermore, they estimated the density of warm gas with an assumption of the path length. Spectra of soft emission by Kaastra et al. (2003) and Finoguenov et al. (2003) are shown in Figure 2.9.

2.3 Galactic warm-hot sources

We need to carefully consider Galactic (interstellar) warm-hot emission to study the (extragalactic) warm-hot intergalactic medium, because they are not separable except by a difference of the redshift sufficiently large compared to the energy resolution of the detector. Although the soft X-ray background due to a hot or warm-hot interstellar medium has been studied since the 1970's (Inoue et al., 1979; Tanaka & Bleeker, 1977), the distribution or origin of these gases has not yet fully understood. Here I summarize briefly the spectral shape and distribution of soft X-ray emission. See reviews by e.g., McCammon & Sanders (1990), Ferrière (2001), and Cox (2005), for current understanding of interstellar medium.

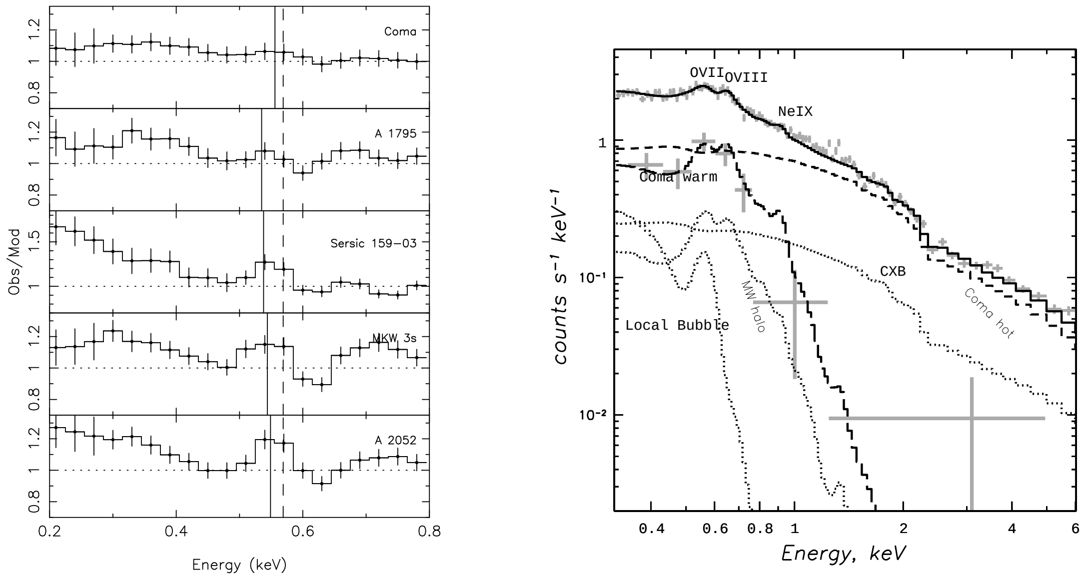

Figure 2.9: Observed soft emission around clusters of galaxies. Left: Fit residuals with respect to the cluster emission model of five clusters by Kaastra et al. (2003). Solid vertical lines show the cluster rest frame energy of O VII line, while dashed lines show it in the rest frame of our Galaxy. Right: A spectrum of the Coma outskirts showing the fitted model and its components.

ROSAT provided a great information on the warm-hot interstellar medium utilizing its good angular resolution and large throughput (the effective area times the field of view) in soft X-ray band. Maps of *ROSAT* All-sky Survey (RASS) in 0.1–0.3 keV (1/4 keV band) and 0.5–1.0 keV (3/4 keV band) are shown in Figure 2.10. Features seen in the figures are a mixture of the following origins: variations in extent of local bubble, halo emission, super bubbles in Galactic disk, Galactic bulge. Extragalactic bright sources and variations of interstellar absorption due to neutral atoms also contributes observed structure. Modeling of diffuse soft X-ray background (without bright sources) have been attempted. McCammon et al. (2002) used a model of a sum of three components for ~ 1 sr field observed in their experiment with sounding rocket (see Figure 2.10 for the field of view): one power-law component for cosmic X-ray background (CXB) due to unresolved point sources and two thermal plasma components, which represents Milky-way Halo (MWH) and local hot bubble (LHB) emission, respectively. Lumb et al. (2002) used the same model with slightly different parameters for an average of eight fields at high galactic latitude observed with *XMM-Newton*. I summarize models in their paper in Table 2.2. Lumb et al. (2002) reported that mean deviation of 0.2–1.0 keV intensity is $\sim 35\%$ from field to field, which strongly suggests a difference of both temperature and absorption column between each field. The discrepancy would be much larger in a field of apparent excess or absorption structure.

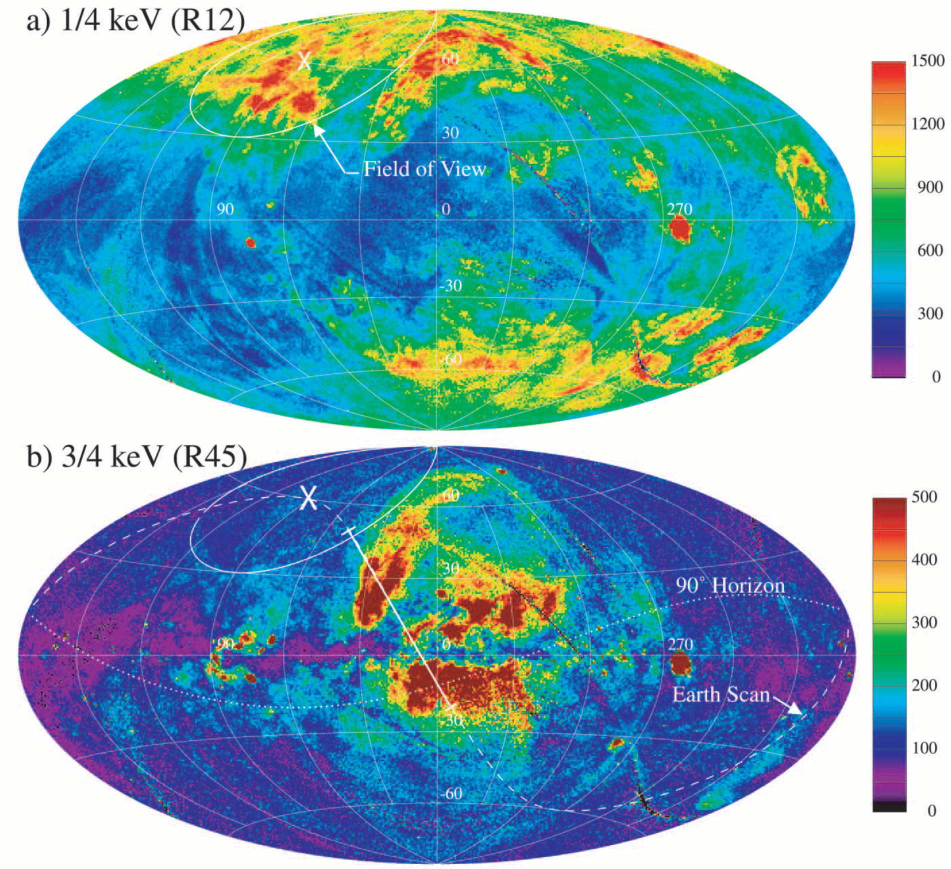

Figure 2.10: *ROSAT* maps of the (a) 1/4 keV band and (b) 3/4 keV diffuse background in Galactic coordinates by McCammon et al. (2002) (originally Snowden et al., 1995). *ROSAT* intensity units are 10^{-6} counts s^{-1} $arcmin^{-2}$. The field of view of their sounding rocket experiment is also shown.

2.4 Abundance of the ISM

The metal abundance is an important parameter for the understanding of the chemical evolution of the universe. However, large uncertainties remain in our knowledge of the abundance, even for that in the solar system or interstellar medium (ISM). The solar abundance of Anders & Grevesse (1989) is sometimes regarded as the average of our Galaxy. However, UV absorption lines due to interstellar gas and optical absorption lines in the atmosphere of young B-stars have indicated that the metal abundance in the ISM of our Galaxy is on average about two thirds of the solar abundance (Savage & Sembach, 1996; Snow & Witt, 1996). Moreover, the solar abundance itself is not determined well. Grevesse & Sauval (1998) and Holweger (2001) reported significantly lower O solar abundance than the value of Anders & Grevesse (1989). X-ray spectroscopy of interstellar absorption edges (Takei et al., 2002) also supports the lower O abundance than Anders & Grevesse (1989).

Recently, Asplund et al. (2005) compiled revised solar abundance using improved modeling of solar photosphere lines, which yielded lower abundance for some elements including O. The abundance of Asplund et al. (2005) is consistent with the observations of ISM and

Table 2.2: Model parameters of soft X-ray background in 1 sr field of view.

Parameter	McCammon et al. (2002) with solar abundance[a]	McCammon et al. (2002) with depleted abundance[b]	Lumb et al. (2202)
Power-law component (CXB)			
Exponent	1.52	1.52	1.42
Normalization[c]	12.3	12.3	9.03
$N_{\rm H}$ (H atoms cm^{-2})	1.8×10^{20}	1.8×10^{20}	—[d]
Absorbed thermal component (MWH)			
Temperature kT (keV)	0.225	0.317	0.204
EM (cm^{-6} pc)	3.7×10^{-3}	5.3×10^{-3}	3.1×10^{-3}
$N_{\rm H}$ (H atoms cm^{-2})	1.8×10^{20}	1.8×10^{20}	—[d]
Unabsorbed thermal component (LHB)			
Temperature kT (keV)	0.099	0.107	0.074
EM (cm^{-6} pc)	8.8×10^{-3}	5.3×10^{-2}	4.7×10^{-2}

[a]: Anders & Grevesse (1989).
[b]: Savage & Sembach (1996) for cool clouds toward ζ Ophiuchi (their Table 5).
[c]: in a unit of ph keV^{-1}cm^{-2}s^{-1} at 1keV.
[d]: different from a field of view to another.

Table 2.3: Abundance of O, Ne and Fe

	$Z_{\rm ISM}$	$Z_\odot$	$Z_{\rm ISM}/Z_\odot$
O/H	4.57×10^{-4}	8.51×10^{-4}	0.54
Ne/H	1.87×10^{-4}	1.23×10^{-4}	1.52
Fe/H	2.82×10^{-5}	4.68×10^{-5}	0.60

B-star abundance for most elements. However their values lead to disagreement between solar interior models and helioseismology results.

The models can be brought back into agreement with observations if the Ne abundance is higher than previously thought (Antia & Basu, 2005). Indeed, Ne abundance should be determined by other observations since Ne abundance is not directly determined by solar photosphere due to lack of strong solar photospheric lines. Drake & Testa (2005) showed that O/Ne ratio could be lower than Asplund et al. (2005) ratio using X-ray spectroscopy of solar-like stars. It is the value required for agreement between solar interior models and observations. Note that an overabundance of Ne is also suggested in other measurements of warm-hot absorption (Nicastro et al., 2002; Nicastro et al., 2005c) and emission from cluster cool cores (Peterson et al., 2003).

Considering these observations, we adopt in this thesis Asplund et al. (2005) values for O and Ne, and use O/Ne ratio of Drake & Testa (2005) to calculate the Ne abundance. This may be confusing because people in X-ray astronomy community usually uses Anders & Grevesse (1989) values and quote the abundance in units of 'solar' abundance. To clearly distinguish old widely-used solar abundance and the abundance we adopted, we define $Z_\odot$ as Anders & Grevesse (1989) values and $Z_{\rm ISM}$ as the abundance values we adopted. O, Ne and Fe abundance of $Z_{\rm ISM}$ and $Z_\odot$ are summarized in Table 2.3.

Chapter 3

Clusters of galaxies studied in this thesis

3.1 Strategy of target selection

The study of the WHIM in this thesis is concentrated on the vicinities of clusters of galaxies. One of the reasons why we chose clusters is that detections of both absorption and emission are expected with existent detectors since the WHIM is thought to have high density around clusters; we need no extraordinarily bright source behind it to detect the absorption. If both are observed, we can measure the density of the gas, as well as constraining the geometry of the emitting zone directly (Krolik & Raymond, 1988; Sarazin, 1989). Another reason is that we can easily distinguish the absorption of the WHIM from that of the Galactic warm-hot gas since grating spectrometers have a capability of separating the redshift of the clusters from Galactic one. Additionally, studies of the WHIM near clusters would provide unique information on the ongoing interaction between the WHIM and the cluster. The expected temperature of the WHIM is higher than the WHIM in the low-density region. Thus, this study is fully complementary to a 'random search' for absorption in the spectra of extraordinarily bright blazars (e.g., Nicastro et al., 2005b).

We investigated the most feasible targets as follows. First we picked clusters that are elongated in the line-of-sight direction. The long filament and large projected length expected in these clusters enhances the absorption and emission, and thus makes detections more plausible. Next, we searched the RASS bright source catalogue (Voges et al., 1999) for bright quasars behind the clusters to study the WHIM in absorption. We selected two clusters of galaxies that have a bright background quasars: the Coma cluster with X Comae behind it and the Virgo cluster with LBQS 1228+1116 behind it. We also studied another elongated cluster Abell 2218 (A2218). Though no bright object was behind the cluster, i.e., absorption study was impossible, the large redshift of the cluster, $z = 0.1756$, allows us to distinguish emission lines from the WHIM from Galactic lines even with the energy resolution of X-ray CCDs. To summarize, our observation targets were three clusters of galaxies: the Coma cluster, the Virgo cluster and A2218.

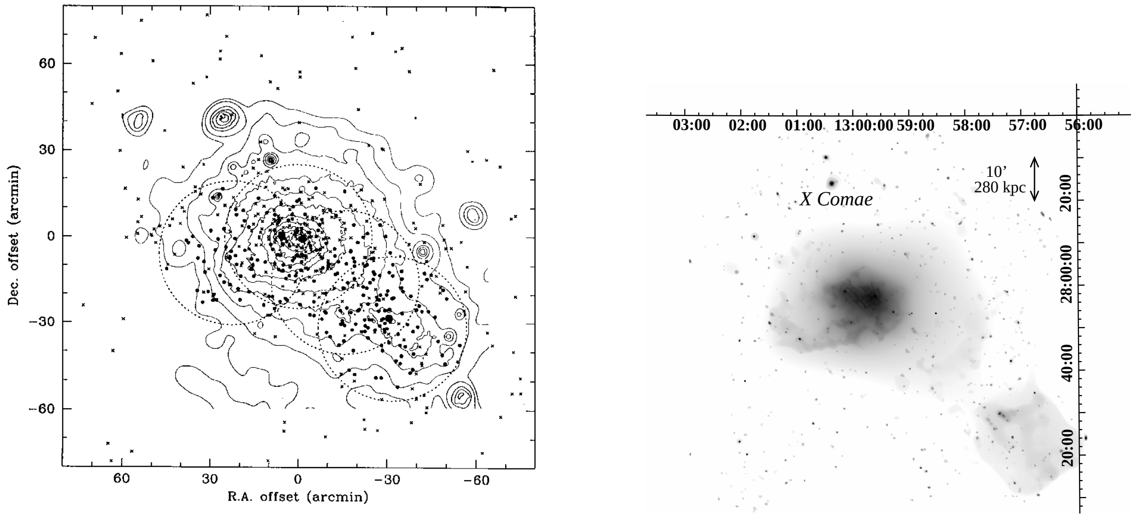

Figure 3.1: Maps of the Coma cluster. Left: positions of galaxies (dots and crosses) overlaid with the X-ray contours of a *ROSAT* observation (Colless & Dunn, 1996). Right: an X-ray image in the 0.5–2.0 keV band observed with *XMM-Newton* (Finoguenov et al., 2003).

3.2 The Coma cluster and X Comae

The Coma cluster, also known as A1656, is a nearby cluster located near the north Galactic pole. The distribution of the galaxies in the Coma cluster and an X-ray emission map are shown in Figure 3.1. Two substructures are clearly seen in both galaxy distribution and X-ray images. The bigger one in the northeast is centered on NGC 4874, and the southeast one is centered on NGC 4839. The location of NGC 4874 is ($12^{\rm h}59^{\rm m}35^{\rm s}.7$, $+27°57'33''.8$) in equatorial coordinates (J2000.0) or ($58°.0872$, $88°.0100$) in Galactic coordinates.

It is also known that the Coma cluster together with another cluster, A1367, form a structure called the Coma–A1367 chain or the Coma supercluster. The three-dimension distribution of galaxies in the Coma–A1357 chain is shown in Figure 3.2 at the left. Not only do the cluster appear connected by a bridge of galaxies in the sky plot, the wedge plot also shows that the galaxies are at the same distance as the two clusters and therefore represent a physical connection. A histogram of line-of-sight velocities of the galaxies in the Coma cluster is shown in Figure 3.2-right. The mean of the redshift is $z = 0.0231$, and the standard deviation is $\sigma_{\rm gal} = 3.23 \times 10^{-3}$, where $\sigma_{\rm gal}$ is converted to redshift in the observed frame (Struble & Rood, 1999). The distribution of the velocities is asymmetric and better fitted with a double-Gaussian model rather than a Gaussian model. This extension in the line of sight direction is also seen in the wedge plot (Figure 3.2-left). The galaxies in the plot appears to form a shell-like structure. Therefore, an elongated structure is indicated in the direction of the Coma cluster.

The large scale (over 1°) X-ray structure is studied with the *ROSAT*, *ASCA* and *XMM-Newton* satellites. The X-ray surface brightness is represented for r up to $\sim 3°$ by a β model with $\beta = 0.75 \pm 0.03$ and $R_{\rm C} = 10.5 \pm 0.6$ arcmin (Briel et al., 1992). The temperature of the cluster is on average 8.67 keV (White, 2000), which implies the radius within which the cluster's average density is 200 times $\rho_{\rm crit}$, r_{200}, is 2.5 h_{70}^{-1} Mpc. Complicated structures

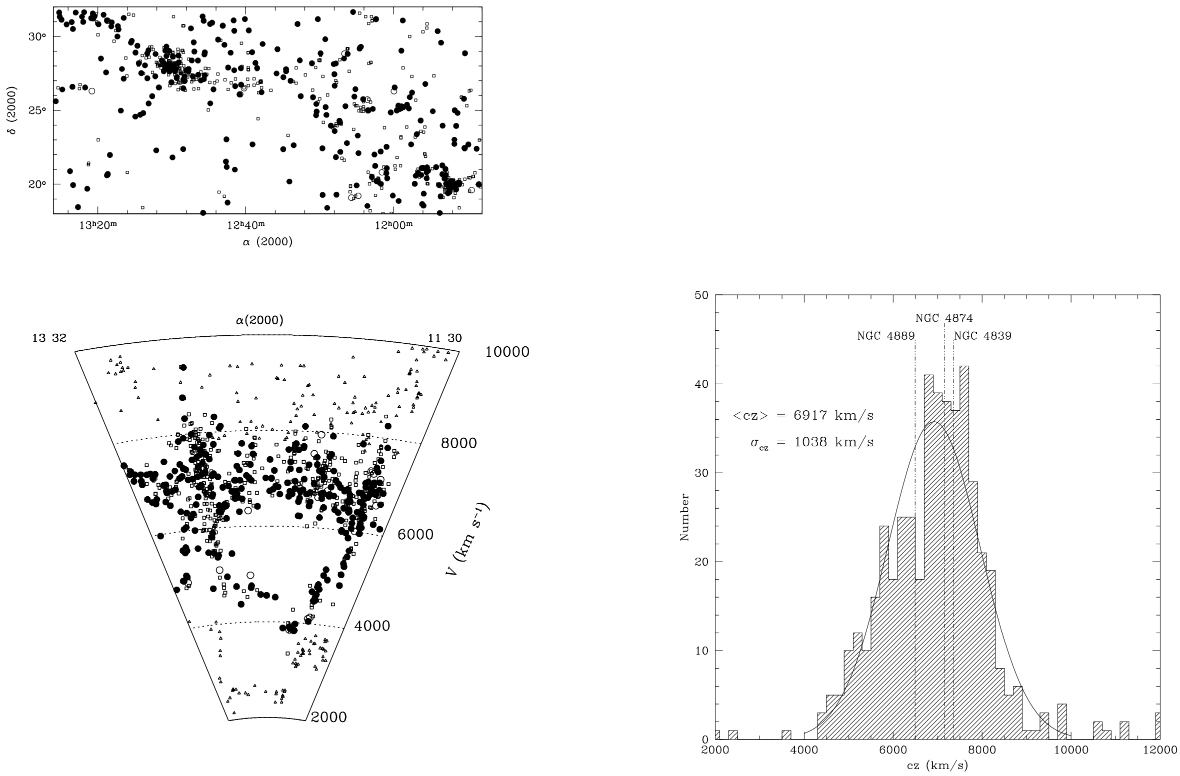

Figure 3.2: Distributions of galaxies in the Coma cluster and in the Coma–A1367 supercluster. Left: distributions of galaxies from Gavazzi et al. (2006). The top panel is a sky projection view, while the bottom panel is a wedge diagram in the declination interval $18° < \mathrm{Dec} < 32°$. The left clustering is the Coma cluster, and right one is A1367. Right: distribution of line-of-sight velocities of galaxies in the Coma cluster from Colless & Dunn (1996).

are, however, observed in the temperature map as shown in Figure 3.3 ; there is a region in which the temperature is as high as 14 keV in the northwest, while the southeast region near NGC 4911 and southwest region near NGC 4839 have a temperatures of ~ 5 keV (Watanabe et al., 1999). These structures show convincing evidence of ongoing dynamical evolution of the cluster. Neumann et al. (2003) showed that NGC 4839 and NGC 4911 are falling onto the cluster using *XMM-Newton* observations. Another note for the Coma cluster is a detection of soft excess in its outskirts. Finoguenov et al. (2003) detected a significant soft excess in the spectrum of the northwest outskirt (see Figure 2.9 for the spectrum).

X Comae, the Seyfert 1 AGN, is the brightest object behind the Coma cluster. It is located at ($13^{\mathrm{h}}00^{\mathrm{m}}22^{\mathrm{s}}.17$, $+28°24'2''.6$) in equatorial coordinates (J2000.0) or ($66°.2306$, $87°.6500$) in Galactic coordinates. As shown in Figure 3.1-right, it is $26.5'$ or $0.74 h_{70}^{-1}$ Mpc or 0.31 r_{200} north of NGC 4874. Its redshift is 0.091 ± 0.001 (Branduardi-Raymont et al., 1985). Galactic N_{H} is $N_{\mathrm{H}} = 9.3 \times 10^{19}$ cm^{-2} (Dickey & Lockman, 1990).

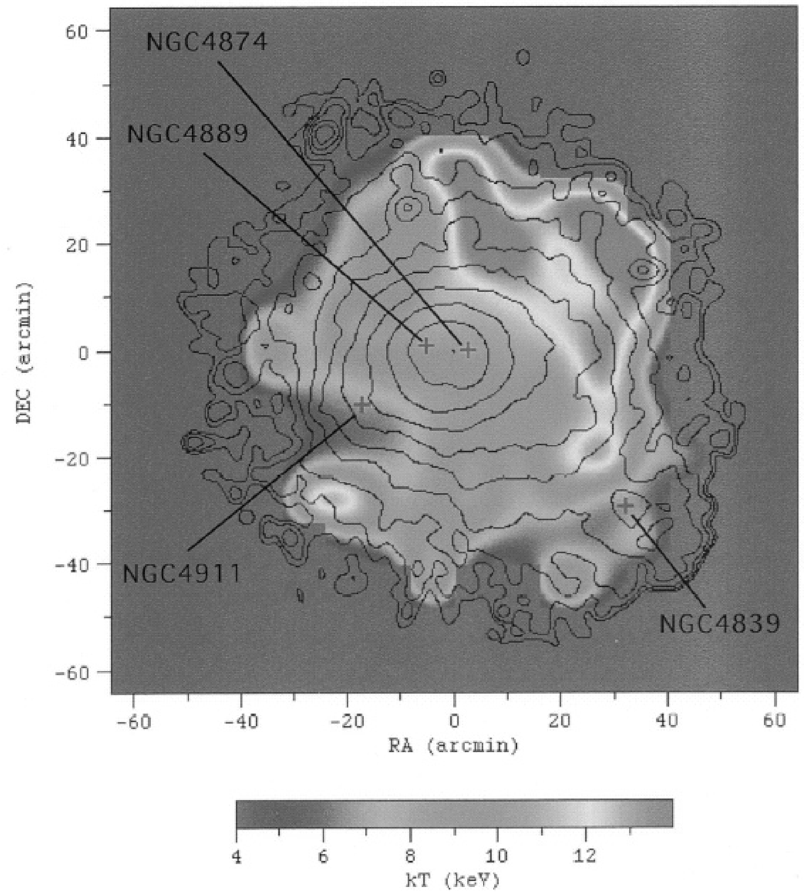

Figure 3.3: Color-coded temperature map superposed on the contour map of the total band surface brightness from Watanabe et al. (1999).

3.3 The Virgo cluster and LBQS 1228+1116

The Virgo cluster is one of the nearest clusters of galaxies. Its distance is $\sim$ 20 Mpc, so near that the cluster has a physical connection to the Local Group, which is a small group of galaxies that includes our own. The angular size of the cluster is $\sim 4^\circ$ in radius as shown in Figure 3.4. It has a highly irregular shape, elongated in the north-to-south direction. The position of a cD galaxy, M87, is ($12^{\rm h}30^{\rm m}49^{\rm s}.4$, $+12^\circ23'28''.04$) in Equatorial coordinates (J2000.0) and ($283^\circ.7778$, $74^\circ.4912$) in Galactic coordinates.

The three-dimension structure of the cluster has been investigated with the Tully-Fisher relation (e.g., Yasuda et al., 1997; Gavazzi et al., 1999; Solanes et al., 2002). Using information of the distances, galaxies in the cluster were found to be divided into several subclusters, for example one around the big cD galaxy M87, and one around M49 (Gavazzi et al., 1999). Histograms of distances for galaxies in the cluster are shown in Figure 3.5. The distribution of the galaxies is not symmetric around the center of the distribution; a 'tail' is seen in the backside of the center. The line-of-sight length is $\sim$ 15 Mpc, which is about five times the apparent size. This suggests a filament lying along the line-of-sight direction.

X-ray surface brightness is also shown in Figure 3.4. The surface brightness around

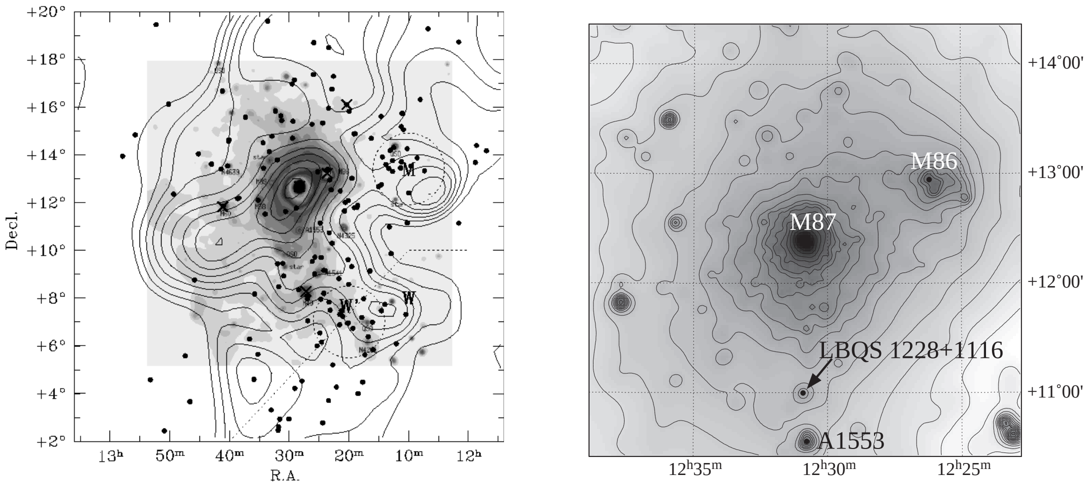

Figure 3.4: Maps of the Virgo cluster. Left panel (Solanes et al., 2002) shows a distributions of the 161 members of the 21 cm sample (points •), overlaid with a contour map of the distance-independent H I deficiency parameter and with a gray-scaled X-ray image. Right panel is a close-up view of X-ray image around M87 taken from Fujimoto et al. (2004). The quasar LBQS 1228+1116 observed in this thesis is also indicated.

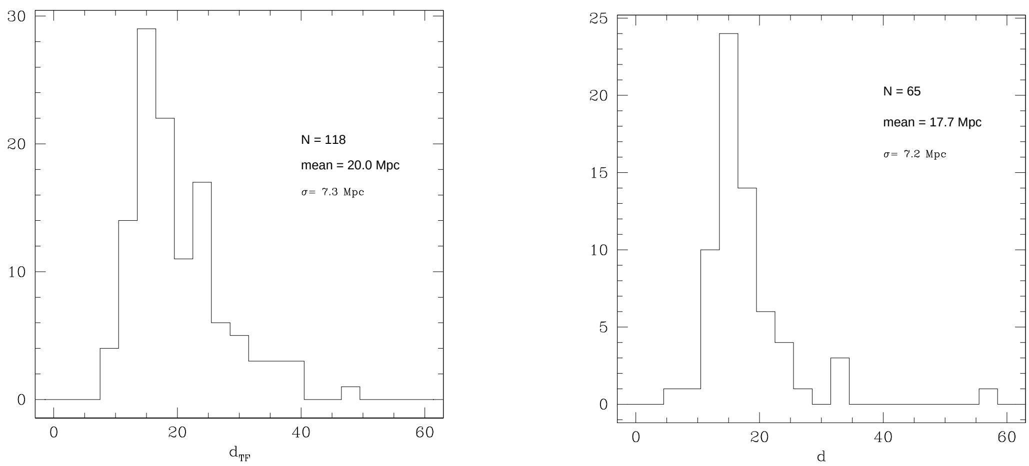

Figure 3.5: Histogram of the distances (in units of Mpc) for 118 spiral galaxies (left) and 65 early-type galaxies (right) from Fouqué et al. (2001).

M87 was well fitted with a β profile with $\beta = 0.45$ and $R_{\rm C} = 2'.3$ in the region $r < 120'$, where r is the distance from M87 (Böhringer et al., 1994). Matsumoto (1998) determined the temperature and abundance of the Virgo cluster up to $170'$ distance from M87. The temperature was $T =$ 2–2.5 keV for $40' < r < 170'$ and the abundance was $Z \sim 0.3\ Z_\odot$ in this region.

The location of the observed quasar LBQS 1228+1116 is $(12^{\rm h}30^{\rm m}54^{\rm s}.12, +11^\circ00'11''.2)$ in equatorial coordinates (J2000.0) or $(285^\circ.2742, 73^\circ.1668)$ in Galactic coordinates, which is 83.3' or $0.45 h_{70}^{-1}$ Mpc south of M87 (in J2000.0; see Figure 3.4). Its redshift is $z = 0.237$ (Hewett et al., 1995), so much behind the Virgo cluster that the structures in a spectrum due to the quasar itself can be easily separated from that of Virgo or Galactic origin from the difference of wavelength. Galactic neutral hydrogen column density in this direction is measured to be $N_{\rm H} = 9.3 \times 10^{19}$ cm^{-2} (Dickey & Lockman, 1990).

3.4 Abell 2218

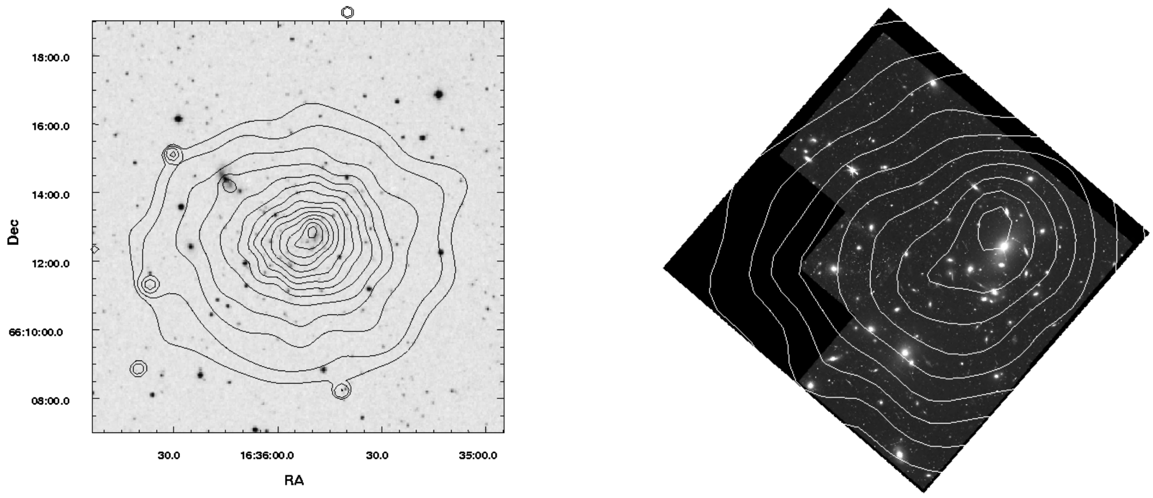

Figure 3.6: X-ray contours overlaid with an optical image by Pratt et al. (2005). The left panel shows a large-scale XMM/DSS overlay image, while the right panel is a close-up view of an XMM/HST overlay image with the same contours.

Table 3.1: Lensing to X-ray Mass Ratios

Lensing Reference	b ($''$)	b (kpc)	M_{lens} ($10^{14}M_\odot$)	M_{xc} ($10^{14}M_\odot$)	M_{xh} ($10^{14}M_\odot$)	M_{lens}/M_{xc}	M_{lens}/M_{xh}
Loeb & Mao 1994	20.8	79.8	0.64	0.19	0.29	3.4	2.2
Allen 1998	20.7	79.4	0.62	0.19	0.29	3.4	2.1
Kneib et al.1995	22.1	84.8	0.61	0.21	0.32	2.9	1.9
Allen 1998	22.1	84.8	0.57	0.21	0.32	2.7	1.8
AbdelSalam et al.1998	22.1	84.8	0.9	0.21	0.32	4.3	2.8
Kneib et al.1995	66.7	256	2.7	1.49	2.33	1.8	1.2
Squires et al.1996	99.8	383	2.4 ± 0.6	2.67	4.18	0.9	0.6
Smail et al.1997	99.8	383	2.1 ± 0.38	2.67	4.18	0.8	0.5
Squires et al.1996	210	806	7.8 ± 1.4	6.52	10.20	1.2	0.8

Note—- Taken from Machacek et al. (2002). The first five entries are strong lensing results, while the last three are lower bounds on the mass from weak lensing analyses. Mass with in the radius of b from the center is estimated. M_{xc} and M_{xh} are the x-ray masses for $kT = 6.9$ keV and the upper bound $kT = 10.8$ keV, respectively, assuming an $\Omega_m = 1$, $\Omega_\Lambda = 0$, $h = 0.5$ cosmology. The minimum mass model result is used from AbdelSalam et al.(1998).

A2218 is a cluster located at ($16^{\rm h}35^{\rm m}54^{\rm s}$, $+66^\circ 13'.0$) in equatorial coordinates (J2000.0), or ($97^\circ.7452$, $38^\circ.1237$) in Galactic coordinates. Its redshift is 0.1756 and the velocity dispersion of galaxies in the cluster is $\sigma_{\rm gal} = 5.37 \times 10^{-3}$ (Struble & Rood, 1999). This cluster is well known as a gravitational lensing object.

X-ray contours obtained with *XMM-Newton* overlaid with an optical image are shown in Figure 3.6. The cluster has slightly elliptical, symmetric shape at large scales (Figure 3.6-left). The surface brightness is represented by a β-model. The best-fit parameters of the β model obtained with *XMM-Newton* are $R_{\rm C} = 0'.95$ and $\beta = 0.63$ (Pratt et al., 2005). The entire spectrum is represented by a thermal plasma model of $kT = 6.6$ keV and $Z = 0.13\ Z_{\odot}$. *Chandra* provided similar parameters (Machacek et al., 2002): $R_{\rm C} = 1'.11$, $\beta = 0.71$, $kT = 6.9$ keV and $Z = 0.20\ Z_{\odot}$.

An irregularity at the center is also known. Near the core (Figure 3.6-right), the X-ray emission becomes elongated in the SE–NW direction. The irregularity was also found in its temperature profile. Neumann et al. (2003) reported that the temperature map shows a big peak in the central arcminuite region, where the temperature rises by a factor of two (from ~ 5 to ~ 10 keV). It leads to a discrepancy between the mass estimated from gravitational lensing and that determined from X-ray analysis. A summary by Machacek et al. (2002) is shown in Table 3.1. Estimates from gravitational lensing indicate ~ 3 times larger mass than an X-ray model for the central ($\sim 20''$) region.

These profiles suggests that A2218 is still in a dynamical state. X-ray analysis suggests that the cluster core is not in hydrostatic equilibrium due to an ongoing or recent merger (Pratt et al., 2005; Machacek et al., 2002) in the line-of-sight direction. The distribution of galaxy velocities in the optical study of Girardi et al. (1997) also strongly indicates substructure in the line of sight. Smith et al. (2005) studied the mass structure in detail and have also concluded that A2218 is unrelaxed. In summary, an extended structure along line-of-sight direction is highly probable.

Chapter 4

Instruments

4.1 A brief summary of XMM-Newton and Suzaku

We observed the Coma and Virgo clusters with *XMM-Newton* since it has a capability for both fine spectroscopy of a point source with grating spectrometers and imaging spectroscopy of diffuse emission with CCD cameras. On the other hand, we observed A2218 with *Suzaku* because it equips a CCD camera with better energy resolution below 1 keV, where the emission lines from the warm-gas reside. *Suzaku* is the only satellite that can clearly distinguish O VII emission line against the continuum. We investigated redshifted O lines with *Suzaku* to confirm the existence of soft emission in cluster outskirts. There is another in-orbit X-ray satellite, *Chandra*, sensitive to the energy range we are interested in. Although *Chandra* has great angular resolution of $0''.5$, its high internal background level for diffuse sources and small effective area is not appropriate for our study. Thus, we did not use the satellite.

Here I summarized key parameters of the detectors onboard *XMM-Newton* and *Suzaku*, the two satellites used in this thesis. See § 4.2 and § 4.3 for the details of each satellite, respectively. The data of *XMM-Newton* is based on *XMM-Newton Users' Handbook* on XMM-Newton Science Operations Centre Home Page[1], while we referred to *The Suzaku Technical Description*[2] for the information of *Suzaku*.

XMM-Newton has three kinds of detectors: the EPIC-MOS, the EPIC-pn and the RGS. The EPIC (European Photon Imaging Camera) detectors are X-ray CCD cameras. The MOS and the pn has different configuration (see § 4.2.2 for the difference). The RGS (Reflection Grating Spectrometer) is a dispersive spectrometer, which offers outstanding energy (wavelength) resolution for point sources. *Suzaku* has two available detectors: the XIS and the HXD. The XIS (X-ray Imaging Spectrometer) is X-ray CCD cameras, which consist of three FIs (Front Illuminated) cameras and one BI (Back Illuminated) camera. The HXD (Hard X-ray Detector) is a detector which covers the energy range from ~ 10 keV to ~ 300 keV.

Since we are interested in soft ($\lesssim 1$ keV) X-ray band, we did not use the HXD. The energy resolutions (ΔE), the field of view (FOV), the effective area (EA) and half energy width (HEW) of the EPIC-MOS, the EPIC-pn, the RGS, the XIS-FI and the XIS-BI are shown in Table 4.1. Note that the RGS is a dispersive detector; the energy resolution becomes significantly worse for extended ($\gtrsim 5'$) sources. Imaging analysis is impossible. Although

[1] `http://xmm.vilspa.esa.es/external/xmm_user_support/documentation/uhb/XMM_UHB.pdf`

[2] `http://www.astro.isas.ac.jp/suzaku/research/proposal/ao1/doc/suzaku_td.pdf`

Table 4.1: Instrument parameters

	EPIC-MOS	EPIC-pn	RGS[a]	XIS-FI	XIS-BI
ΔE (FWHM; 1 keV)	70 eV	80 eV	5 eV	50 eV	60 eV
ΔE (FWHM; 0.5 keV)	55 eV	70 eV	2 eV	40 eV	45 eV
FOV	30′ diameter	30′ diameter	—	$17.8' \times 17.8'$	$17.8' \times 17.8'$
EA[b] (1 keV)	640 cm^2	700 cm^2	60 cm^2	600 cm^2	300 cm^2
EA[b] (0.6 keV)	260 cm^2	300 cm^2	50 cm^2	60 cm^2	120 cm^2
EA[b] (0.5 keV)	400 cm^2	450 cm^2	90 cm^2	120 cm^2	140 cm^2
HEW	13.8″	15.2″	—	140″	115″

[a]: The properties for point sources.
[b]: The values of EPIC-MOS and XIS-FI are a sum of two and three cameras, respectively.

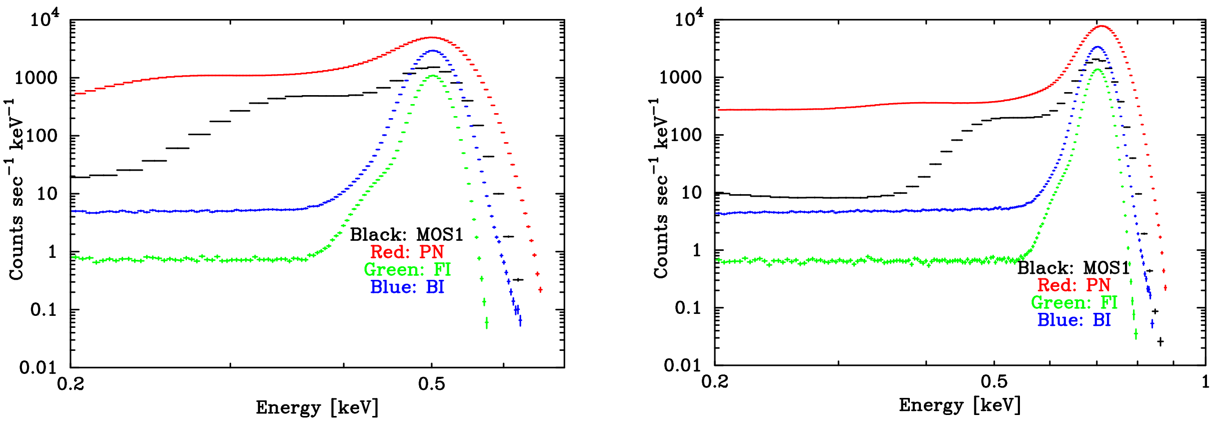

Figure 4.1: Comparison of line profile of single monotonic line of $E = 0.5$ keV (left) and $E = 0.7$ keV (right). Black, red, green and blue lines show the EPIC-MOS, the EPIC-pn, the XIS-FI and the XIS-BI, respectively.

the difference between energy resolution of the EPIC and the XIS is small, the XIS has a much better capability of line spectroscopy. Responses to a monotonic single line obtained with the EPIC and the XIS are compared in Figure 4.1. The profiles of the EPIC-MOS and the EPIC-pn has a big tail in low energy. These tails make difficult a detection of a weak line against continuum.

4.2 The XMM-Newton satellite

XMM-Newton (Jansen et al., 2001) was launched on the 10th December 1999 by an Ariane 5 launcher into a highly elliptical orbit, with an apogee of about 115,000 km and a perigee of about 6,000 km. The orbital inclination is 33°, the right ascension of the ascending node is 195° and the argument of perigee 89°. Such an orbit provides the best visibility in the southern celestial sky. Objects are continuously observable during the entire visibility period in an orbit, as *XMM-Newton* is operated with three ground stations which are located at Perth, Kourou and Santiago. Thus, the complete visibility period (145 ksec) is available for continuous observations.

There are three types of scientific instruments onboard *XMM-Newton*: three X-ray CCD cameras called the European Photon Imaging Camera (EPIC), two high-resolution X-ray spectroscopy instruments called the Reflection Grating Spectrometer (RGS), and the Optical Monitor (OM). The three EPICs and the two detectors of the RGS reside in the focal planes of the X-ray telescopes, while the OM has its own telescope.

4.2.1 X-ray Telescopes (XRTs)

4.2.1.1 Design Structure

The three XRTs of *XMM-Newton* are co-aligned with an accuracy of better than about 1 arcmin. Each of the three telescopes consists of 58 Wolter type-I mirrors, and the mirror grazing incidence angles range between 17 and 42 arcmin. The focal length is 7.5 m and the diameter of the largest mirrors is 70 cm. One telescope with the pn camera at the focal point has a light path as shown in Figure 4.2–left. The two others have grating assemblies in their light paths, diffracting part of the incoming radiation onto their secondary focus as shown in Figure 4.2–right. About 44 % of the incoming light focused by the XRT is directed onto the MOS camera at the prime focus, while 40 % of the radiation is dispersed by a grating array onto a linear strip of CCDs. The remaining light is absorbed by the support structures of the RGAs.

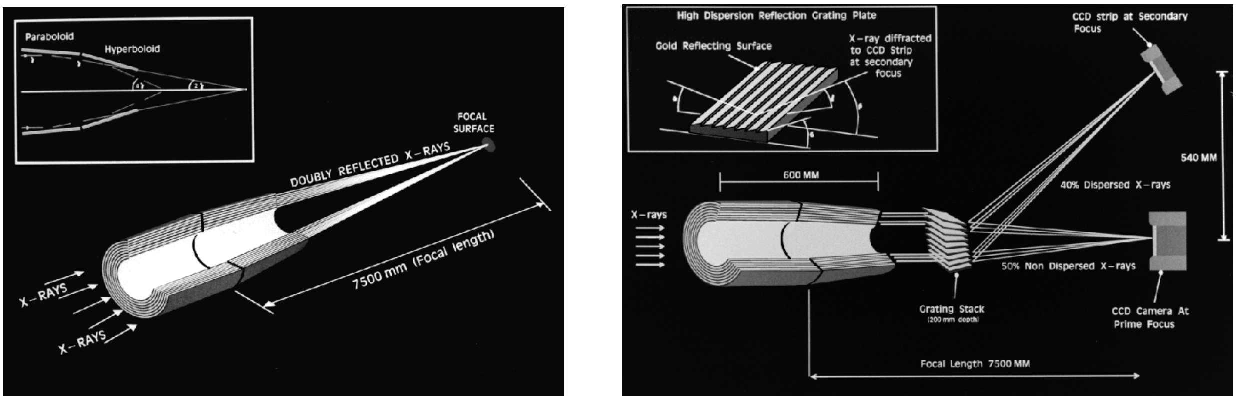

Figure 4.2: The light path in XRT of *XMM-Newton*. Left: with the pn camera in focus; right: with MOS camera and RGA

4.2.1.2 Point-spread function (PSF) of XRTs

A point-spread function (PSF) determines the imaging quality of an XRT. Figure 4.3 shows the in orbit on-axis images obtained by each detector. The radial substructures are caused by the spiders holding the mirror shells. Figure 4.4 displays the azimuthally averaged profile of the PSF of one XRT together with the best-fit King profile, which has the form $A(1/[\{1+(r/r_c)^2\}^\alpha])$, where r is the radial distance from the center of the PSF, r_c is the core radius and α is the slope of the King model. Figure 4.5 shows the encircled energy function (hereafter EEF) as a function of radius from the center of the PSF for several different energies. For on-axis source, high energy photons are reflected and focused predominantly by the inner shells of the XRTs. The inner shells apparently give better focus than the average of all shells, hence the EEF increase with increasing photon energy. A half energy width (hereafter HEW), which means the width including half of all the reflected photons, of the PSF can be derived from EEF. Table 4.2 lists the on-axis HEW of the different XRTs measured in orbit and on ground.

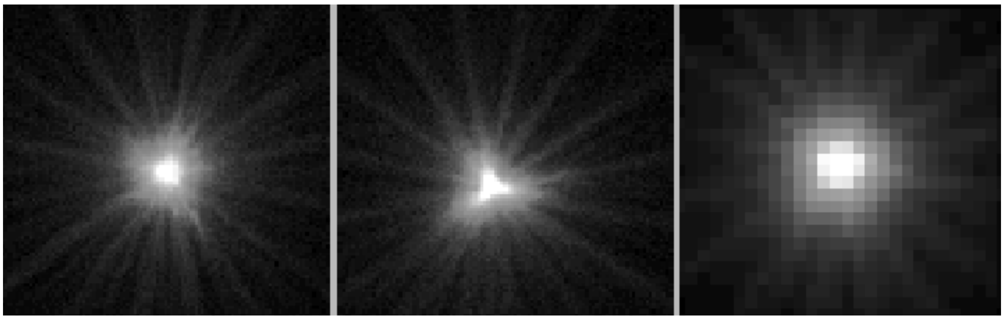

Figure 4.3: On-axis images of the MOS1, MOS2 and pn XRTs (left to right). The images are 110 arcsevc wide and a logarithmic scale has been used to visualize the wings of the point spread function.

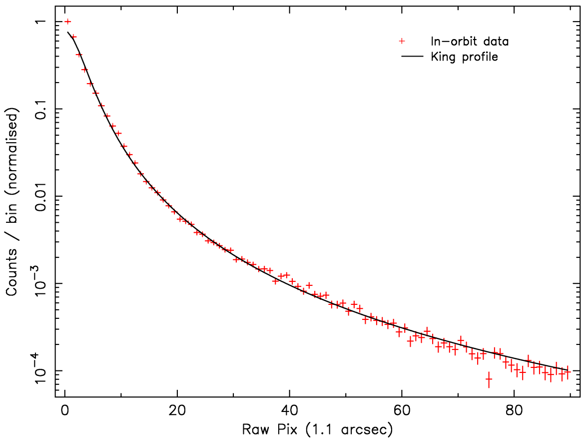

Figure 4.4: Radial counts distribution for the on-axis PSF of the MOS1 XRT in the 0.75–2.25 keV energy range. The solid line indicates the best-fit King profile.

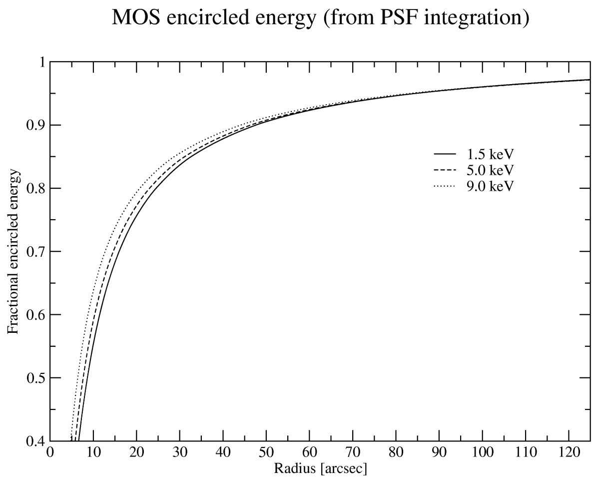

Figure 4.5: The encircled energy function as a function of angular radius (on-axis) at different energies. The curves are calculated assuming a fractional encircled energy of 100 % at a radial distance of 5 arcmin.

4.2.1.3 Effective Area (EA) of XRTs

An effective area is an indicator of ability of collecting photons. *XMM-Newton* carries the XRT with the largest effective area of focusing telescope ever. The total mirror geometric effective area (EA) at 1.5 keV energy is about 1,550 cm^2 for each telescope, i.e., 4,650 cm^2

Table 4.2: The on-axis in orbit and on ground 1.5 keV HEW of the different XRT.

Instr.	pn	MOS1	MOS2
	orbit/ground	orbit/ground	orbit/ground
HEW [arcsec]	15.2/15.1	13.8/13.6	13.0/12.8

in total. Figure 4.6 shows the on-axis effective area of all *XMM-Newton* XRTs. The EAs of the two MOS cameras are lower than that of the pn, because only part of the incoming radiation falls onto these detectors, which are partially obscured by the RGAs. Not only the shape of the X-ray PSF, but also the effective area of the XRT is a function of off-axis angle within the field of view. Decreasing of photons reflected effectively in the XRT arises from an increasing off-axis angle. This effect is called vignetting. Figure 4.7 displays the vignetting function as a function of off-axis angle for several different energies. The vertical axis is normalized by the on-axis effective area.

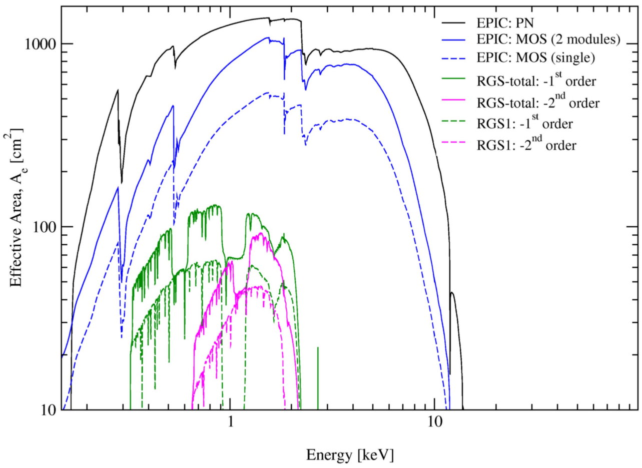

Figure 4.6: The net effective area of all *XMM-Newton* XRT, combined with the response characteristics of the focal detectors.

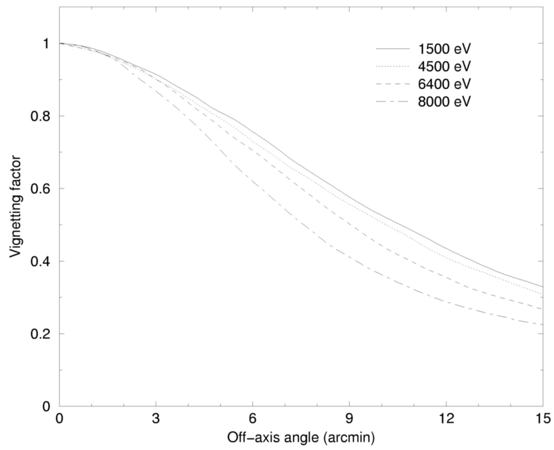

Figure 4.7: Vignetting function as a function of off-axis angle at several different energies (based on simulations).

4.2.2 European Photon Imaging Camera (EPIC)

Two of *XMM-Newton*'s X-ray telescopes are equipped with EPIC MOS (Metal Oxide Semiconductor, Turner et al., 2001) CCD arrays, while the third one carries a different CCD camera called EPIC pn (Strüder et al., 2001). The EPIC cameras offer the possibility to perform extremely sensitive imaging observations over a field of view of 30 arcmin and the energy range from 0.15 to 15 keV, with moderate spectral ($E/\Delta E \sim$ 20–50) and angular resolution (15 arcsec HEW). The detector layout and the baffled X-ray telescope FOV of both types of EPIC cameras are shown in Figure 4.8. The pn chip array is slightly offset with respect to the optical axis of its X-ray telescope so that the nominal, on-axis observing position does not fall on the central chip boundary. This ensures that more than 90 % of the energy of an on-axis point source are collected on one pn CCD chip. Two EPIC MOS cameras are rotated by 90° with respect to each other. The dead spaces between the MOS chips are not gaps, but unusable areas due to detector edges (the MOS chip physically overlap each other, the central one being located slightly behind the ones in the outer ring). All EPIC cameras are operated in photon counting mode with a fixed, mode dependent frame read-out frequency.

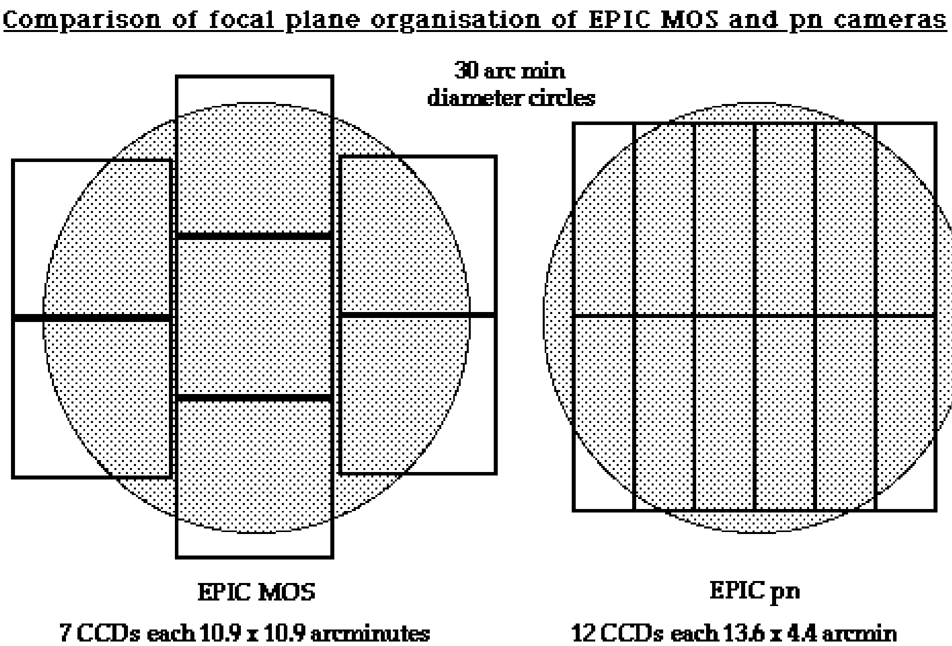

Figure 4.8: A rough sketch of the field of view of the two types of EPIC cameras (MOS, left; pn, right). The shaded circle depicts a 30 arcmin diameter area which is equivalent with the XRT field of view.

4.2.2.1 Two Types of EPIC Cameras: MOS and pn

The two types of EPIC cameras are fundamentally different. This does not only hold for the geometry of the MOS chip array and the pn chip array, but other properties as well, for example, their readout times. The readout of the pn chips is much faster than that of the MOS cameras, because each pixel column has its own readout node. Another important difference is that the MOS chips are front-illuminated, while the pn CCDs are back-illuminated, which affects the detector quantum efficiencies decisively.

The MOS chip arrays consist of 7 individual identical, front-illuminated chips. The individual CCDs are not co-planar, but offset with respect to each other, following closely the slight curvature of the focal surface of the Wolter telescopes. Technically, this leaves space for the connections to the central CCD. The heart of the pn camera is a single Silicon wafer with 12 CCD chips integrated.

4.2.2.2 Science Modes of the EPIC Cameras

The EPIC cameras allow several modes of data acquisition, which are called *Full frame mode*, *Large window mode*, *Small window mode* and *Timing mode* in order to allow the optimized observations for different count rates. All observations in the analysis in this thesis are performed with Full Frame mode.

4.2.2.3 Angular resolution

The EPIC MOS and pn cameras have pixels with sizes of 40 and 150 μm, respectively. For the focal length of the X-ray telescopes (7.5 m), these pixel size corresponds to 1.1 arcsec and 4.1 arcsec on the sky. Since they are smaller than the HEW of XRT (15 arcsec), EPIC's angular resolution is basically determined by the PSF of the mirror modules.

4.2.2.4 Energy resolution

The resolving power of EPIC cameras is determined by the intrinsic energy resolution of the individual pixels. Figure 4.9 show the energy resolution (FWHM) of MOS and pn. The measured in-flight FWHM of the Al Kα (1.5 keV) and Mn Kα (5.9 keV), which are the on-board calibration lines, are also plotted in Figure 4.9. It is well known that the energy resolution of MOS cameras has been gradually decrease due to the CTI (charge transfer inefficiency) effect, which means the imperfect transfer of charge as it is transported through the CCD to the output amplifiers. The latest calibration status is found at *XMM-Newton* Science Operation Centre.[3] The accuracy of the energy determination is about 10 eV over the full energy range and for all modes except for MOS timing mode.

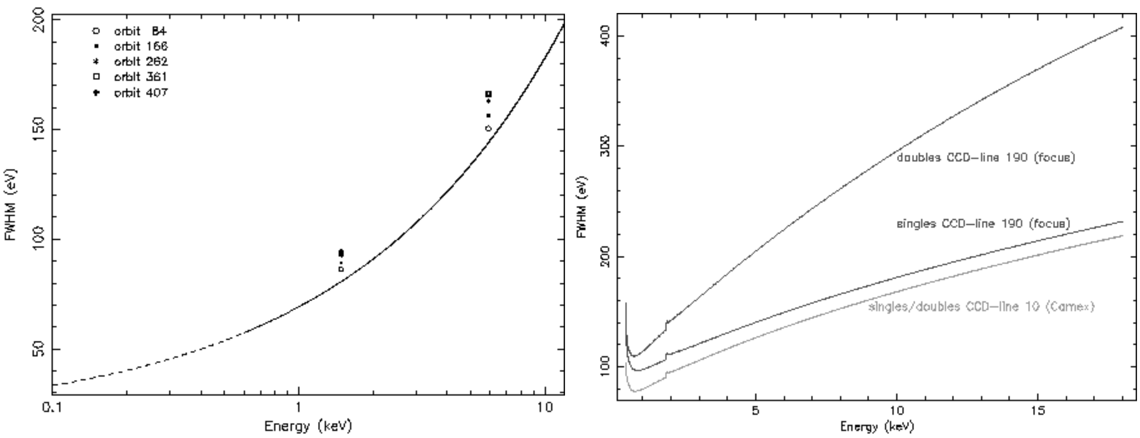

Figure 4.9: The EPIC energy resolution (FWHM) as a function of energy. Left: MOS. The solid curve is a best-fit $E^{0.5}$ function to ground calibration data between 0.1–12.0 keV. Below around 0.6 keV (shown by the dotted region), surface charge loss effects distort the main photo-peak significantly from a Gaussian form and, hence the effective energy resolution. The measured in-flight FWHM of the Al Kα (1.487 keV) and Mn Kα (5.893 keV) lines are also plotted. Right: pn. Curves are given for single and double events (full frame mode) at the focus position as well as at a position 10 pixels away from the readout node.

[3] *http://xmm.vilspa.esa.es/external/xmm_sw_cal/calib/documentation.shtml#EPIC*

4.2.2.5 Quantum efficiencies

The quantum efficiency of both types of EPIC CCD chips as a function of photon energy is displayed in Figures 4.10 and 4.11. These chips were calibrated using laboratory X-ray beams, synchrotron generated monochromatic X-ray beams, before launch, and celestial X-ray source measurements. We can see the typical X-ray absorption fine structure (XAFS) behavior around the silicon K edge at 1.838 keV. Ground calibration measurements have shown that the quantum efficiency of MOS CCDs is uniform above 400 eV. Below this energy, spatial variations are seen as patches in the outer parts of the CCDs where the response is degraded. This inhomogeneity is currently not taken into account by the *XMM-Newton* science analysis system (SAS).

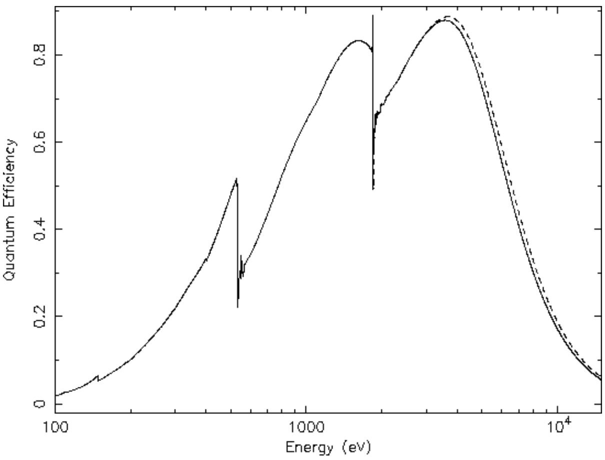

Figure 4.10: Quantum efficiency of the EPIC MOS camera as a function of photon energy.

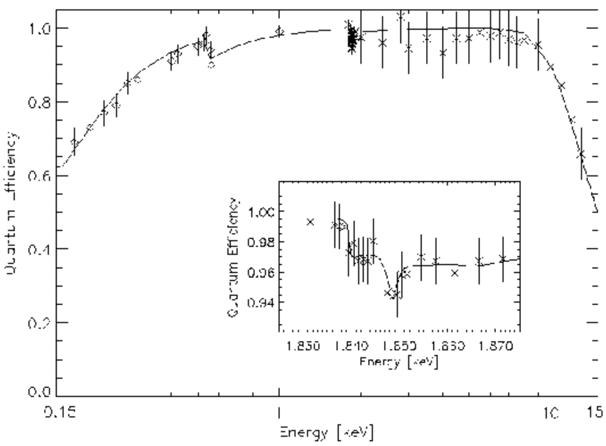

Figure 4.11: Quantum efficiency of the EPIC pn camera as a function of photon energy.

4.2.2.6 EPIC filters

The EPIC CCDs are not only sensitive to X-ray photons, but also to Infra Red, visible and UV light. Therefore, if an astronomical target has a high optical to X-ray flux ratio, there is a possibility that the X-ray signal becomes contaminated by those photons. To prevent such a contribution, each EPIC camera is equipped with a set of 3 separate aluminised optical blocking filters, named *thick*, *medium* and *thin*. The thick filter should be used for all point source targets up to absolute magnitude : $m_{\rm V}$ of 1–4 (MOS) or 0–3 (pn). The medium filter is about 10^3 less efficient than the thick filter, therefore, it is useful for preventing optical contamination from point sources as bright as $m_{\rm V}$ = 8–10. The thin filter is about 10^5 less efficient than the thick filter, so the use of this filter will be limited to point sources with optical magnitudes about 14 magnitudes fainter than the corresponding thick filter limitations.

4.2.2.7 EPIC Background

The EPIC background can be divided into 3 different types of background. First one is a cosmic X-ray background (CXB) dominated by thermal emission at lower energies ($E <$

1 keV) and a power law at higher energies (primarily from unresolved cosmological sources). Second one is EPIC external flaring background due to soft protons ($E \sim$ a few 100 keV) which are most likely organized in clouds populating the Earth's magnetosphere. Figure 4.12 shows the lightcurve badly affected by soft proton flares. The spectra of soft proton flares are variable and no clear correlation is found between intensity and spectral shape. The third one is the EPIC internal quiescent background which is associated with high energy ($E >$ 100 MeV) particles interacting with the structure surrounding the detectors and the detectors themselves. Figures 4.13 and 4.14 display this type of background spectra. The component shows only small intensity variations in time, however shows the spatially inhomogeneous intensity variations.

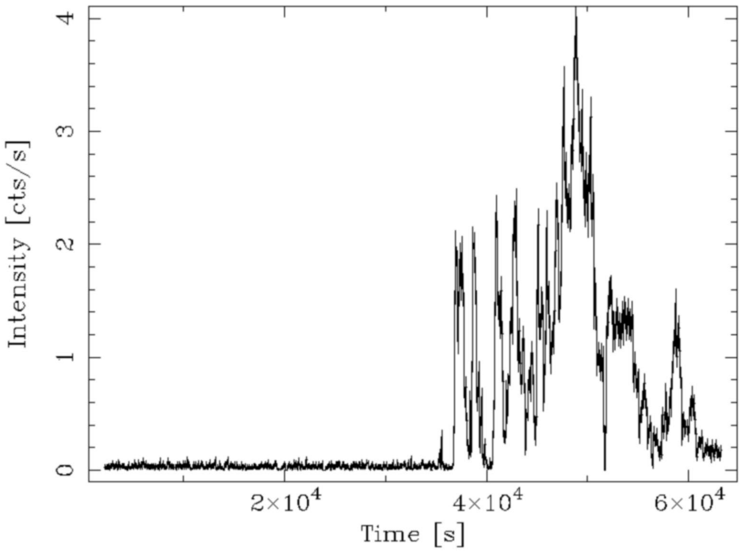

Figure 4.12: Light curve badly affected by soft proton flares.

4.2.3 Reflection Grating Spectrometer (RGS)

Two of the three *XMM-Newton*'s XRTs are equipped with RGS units (den Herder et al., 2001). These consist of Reflection Grating Assemblies (RGAs) and RGS Focal Cameras (RFCs). The RGS optical design is illustrated in Figure 4.15. Figure 4.16 displays the photograph of the RGS units onboard *XMM-Newton*. Each incorporates an array of reflection gratings placed in the converging beam of the XRT. The grating stack consists of 182 precisely aligned reflection gratings and intercepts about 58 % of the light emanating from the telescope. The gratings are actually located on a toroidal Rowland surface, formed by rotating the Rowland circle about an axis passing through the telescope and spectroscopic foci. The gratings are slightly trapezoidal, since their edges lie along rays converging on the telescope focus. The field of view in the cross-dispersion direction is determined by the width of the CCDs ($\pm$ 2.2 arcmin), and the spatial resolution in this direction is largely determined by the imaging properties of the mirror. In the dispersion direction the aperture of RGS covers the entire FOV of the mirrors, only the effective area reduces significantly for off-axis sources.

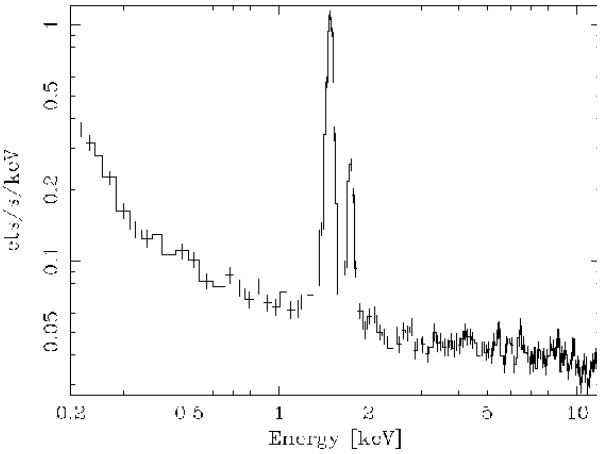

Figure 4.13: Background spectrum for the MOS1 camera during an observation with the filter wheel in the closed position. The prominent features around 1.5 and 1.7 keV are Al K and Si K fluorescence lines, respectively.

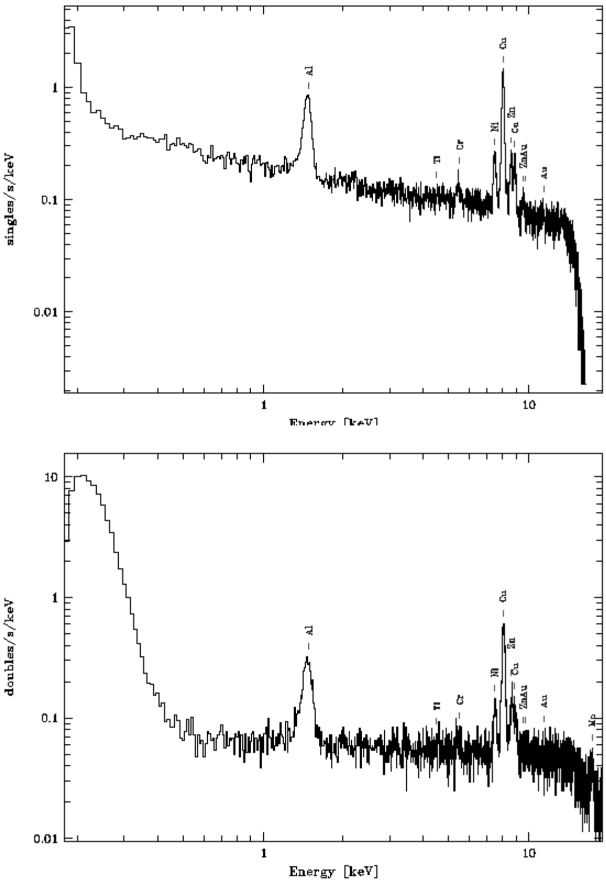

Figure 4.14: Background spectrum for the pn camera during an observation with the filter wheel in the closed position. The prominent features are identified as Al-K (1.5 keV), Cr-K (5.5 keV), Ni-K, Cu-K, Zn-K (8.0 keV) and Mo-K (17.5 keV), respectively.

Nine back-illuminated CCDs are located on the Rowland circle to detect the dispersed spectra in single photon counting mode. However there are problems with failing drive electronics of two CCDs (CCD 4 in RGS-2, covering the wavelength range from 20.1 to 23.9 Åand CCD 7 in RGS-1, 10.5 to 14.0 Å). The position of the X-ray on the detector gives the wavelength through the dispersion equation

$$m\lambda = d(\cos\beta - \cos\alpha), \tag{4.1}$$

where m is the spectral order (-1, -2, ...), d is the groove spacing and α and β are the angles of the incident and dispersed rays measured from the grating plane, respectively (see Figure 4.17). Key parameters are summarized in Table 4.3 and Figure 4.18 indicates the effective areas of both RGS units.

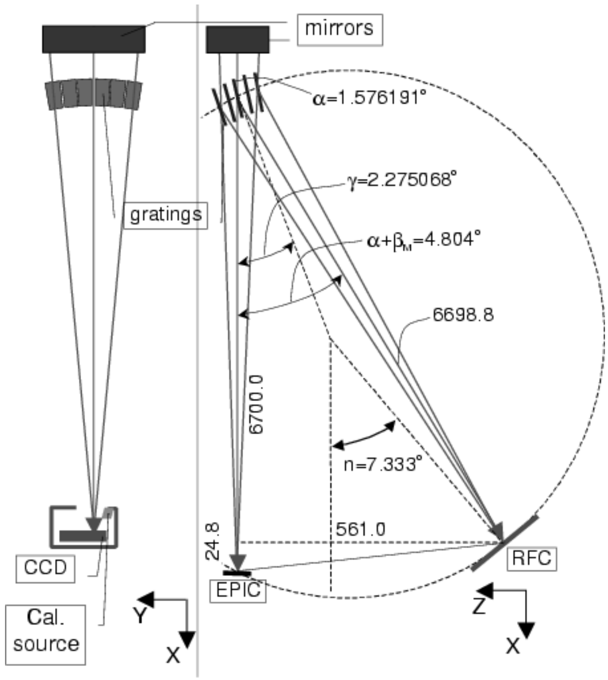

Figure 4.15: Optical design of the RGS (not to scale). X-rays enter from the top. Numerical values for a few key dimensions and angles are indicated (linear dimensions in mm, angles in degrees).

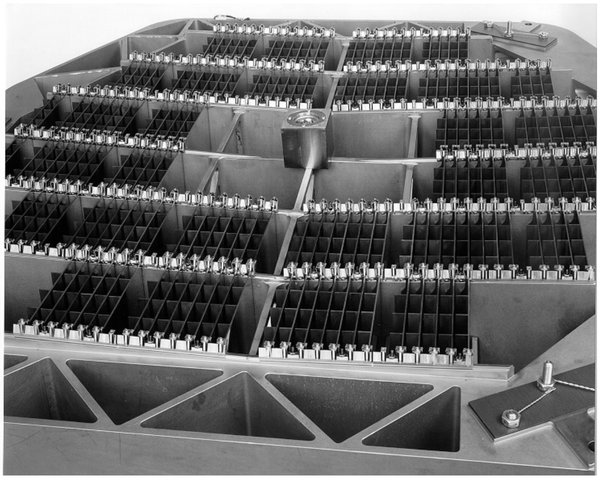

Figure 4.16: Photograph of the RGS unit onboard *XMM-Newton*.

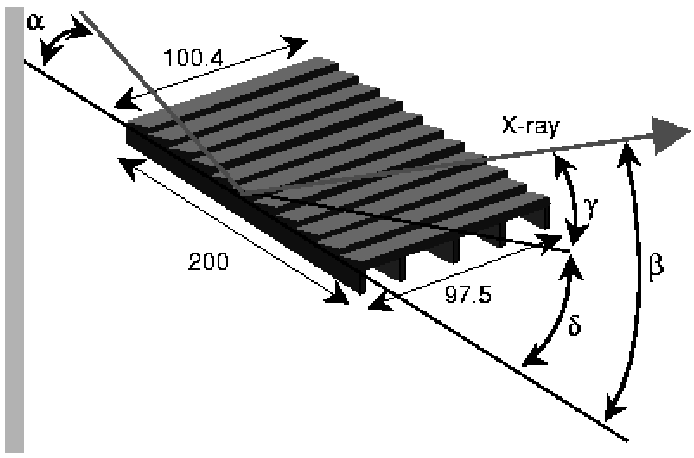

Figure 4.17: Schematic drawing of a grating, including some of the key dimensions and angles.

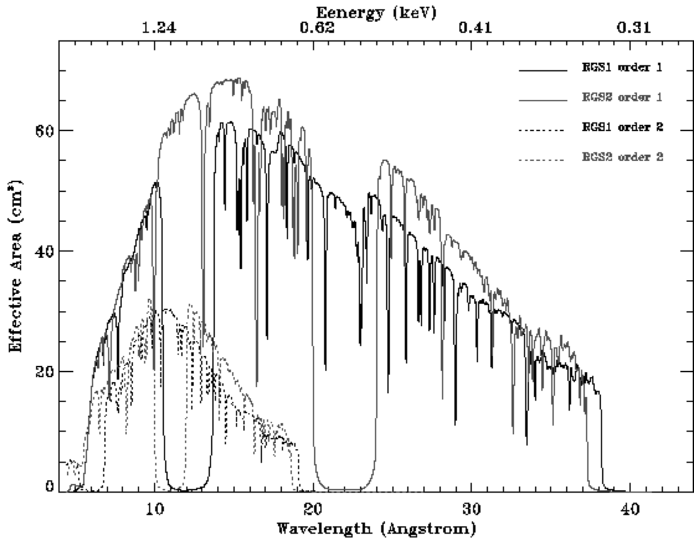

Figure 4.18: Effective area for the two RGSs. The large drops appeared in 10–14 and in 21–24 Åare due to the failing read-out of CCD 4 in RGS-2 and CCD 7 in RGS-1, respectively. Narrow deep drops implies the gaps between the CCDs and narrow small dips are due to corrections for cosmetic blemishes.

Table 4.3: Key performance parameters of the RGSs.

Parameter	Value	Comments
$A_{\rm eff}$	140 cm^2	peak effective area (at 15 Å)
λ	5–38 Å	1st order wavelength range
E	0.35–2.5 keV	1st order energy range
$\lambda/\Delta\lambda$ (FWHM)	100–500	resolving power (line separation)
$\lambda/\Delta\lambda$ (HEW)	100–800	resolving power (weak line detection)
$1/d$	645.6 lines/mm	central groove density
σ_λ	7 mÅ	1σ wavelength accuracy
bin size (3×3 on chip binned)	2.5 arcsec	cross dispersion
	7–14 mÅ	dispersion, 1st order

4.3 The Suzaku satellite

Note that most of this section is written in 2005. Some informations may be obsolete.

4.3.1 Mission Description

Suzaku is placed in a near-circular orbit with an apogee of 568 km, an inclination of 31.9 degrees, and an orbital period of about 96 minutes. The maximum slew rate of the spacecraft is 6 degrees/min, and settling to the final attitude takes ~ 10 minutes, using the star trackers.

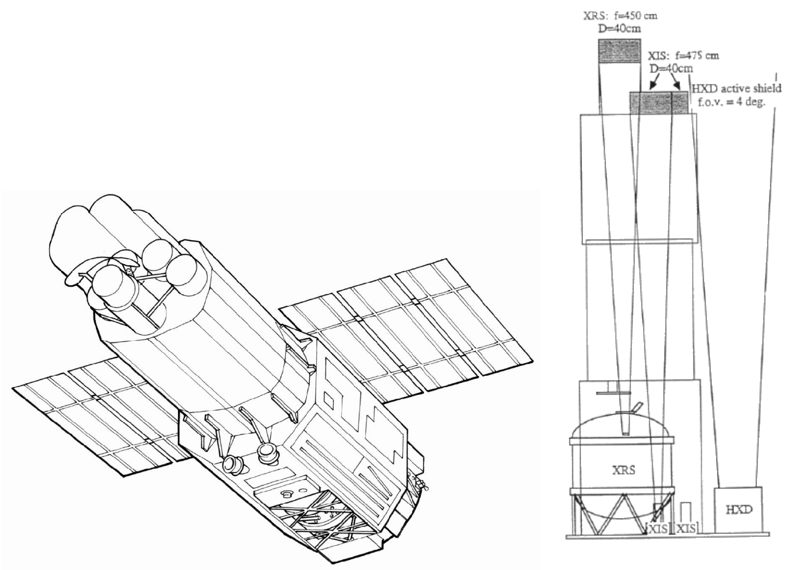

Figure 4.19: [Left] Schematic picture of the bottom of the *Suzaku* satellite. [Right] A side view of the instrument and telescopes on *Suzaku* .

The scientific payload of *Suzaku* (Fig. 4.19) initially consisted of three distinct co-aligned scientific instruments. There are four X–ray sensitive imaging CCD cameras (X–ray Imaging Spectrometers, or XISs), three front-illuminated (FI; energy range 0.4-12 keV) and one back-illuminated (BI; energy range 0.2-12 keV), capable of moderate energy resolution. Each XIS is located in the focal plane of a dedicated X–ray telescope. The second instrument is the non-imaging, collimated Hard X–ray Detector (HXD), which extends the bandpass of the observatory to much higher energies with its 10–600 keV pointed bandpass. The X–Ray Spectrometer (XRS) is no longer operational. XRT–XIS modules and HXD operate simultaneously. In the study of this thesis, only XRT/XIS were used. The detailed description of the HXD is hence omitted.

Table 4.5 summarizes the calibration items of all scientific instruments, the current status, and their expected accuracy. These values are the 90% limits, equivalent to 1.6σ. Note that the values listed are those required from the scientific purpose and ultimate goals which are possible to be realized on the basis of the instrument design, and are not measurement results.

Table 4.4: Overview of *Suzaku* capabilities

S/C	Orbit Apogee	568 km
	Orbital Period	96 minutes
	Observing Efficiency	$\sim 45\%$
XRT	Focal length	4.75 m
	Field of View	$17'$ at 1.5 keV
		$13'$ at 8 keV
	Plate scale	0.724 arcmin/mm
	Effective Area	440 cm^2 at 1.5 keV
		250 cm^2 at 8 keV
	Angular Resolution	$2'$ (HPD)
XIS	Field of View	$17.8' \times 17.8'$
	Bandpass	0.2–12 keV
	Pixel grid	1024×1024
	Pixel size	24 μm× 24 μm
	Energy Resolution	~ 130 eV at 6 keV
	Effective Area	340 cm^2 (FI), 390 cm^2 (BI) at 1.5 keV
	(incl XRT-I)	150 cm^2 (FI), 100 cm^2 (BI) at 8 keV
	Time Resolution	8 s (Normal mode), 7.8 ms (P-Sum mode)
HXD	Field of View	$4.5° \times 4.5°$ ($\gtrsim 100$ keV)
	Field of View	$34' \times 34'$ ($\lesssim 100$ keV)
	Bandpass	10 – 600 keV
	– PIN	10 – 60 keV
	– GSO	30 – 600 keV
	Energy Resolution (PIN)	~ 3.0 keV (FWHM)
	Energy Resolution (GSO)	$7.6/\sqrt{E_{MeV}}$ % (FWHM)
	Effective area	~ 160 cm^2 at 20 keV, ~ 260 cm^2 at 100 keV
	Time Resolution	61 μs
HXD-WAM	Field of View	2π (non-pointing)
	Bandpass	50 keV – 5 MeV
	Effective Area	800 cm^2 at 100 keV / 400 cm^2 at 1 MeV
	Time Resolution	31.25 ms for GRB, 1 s for All-Sky-Monitor

4.3.2 X–Ray Telescopes (XRTs)

Suzaku has five light-weight thin-foil X–Ray Telescopes (XRTs). The These are grazing-incidence reflective optics consisting of compactly nested, thin conical elements. Because of the reflectors' small thickness, they permit high density nesting and thus provide large collecting efficiency with a moderate imaging capability in the energy range of 0.2-12 keV, all accomplished in telescope units under 20 kg each.

Four XRTs onboard *Suzaku* (XRT-I) are used on the XIS, and the other XRT (XRT-S) is for the XRS. XRT-S is no more functional. The XRTs are arranged on the Extensible Optical Bench (EOB) on the spacecraft in the manner shown in Figure 4.20. The external dimensions of the 4 XRT-Is, however, are the same (See Table 4.6, which also includes a comparison with the ASCA telescopes).

The angular resolutions of the XRTs range from $1.8'$ to $2.3'$, expressed in terms of half-power diameter, which is the diameter within which half of the focused X–ray is enclosed.

Table 4.5: Error Budgets of Scientific Instrument Calibrations

	Calibration Item	October 2005	Requirement	Goal
XRT−I/XIS	On-axis effective area [a]	$\sim$10%	5%	5%
	Vignetting	$\sim$50%	5%	2%
	On-axis EEF [b]	$\sim$20%	5%	1%
	Off-axis EEF [c]	$\sim$30%	20%	2%
	Optical axis position in XIS	$\sim 0.5'$	$< 0.2'$	$<0.2'$
	Energy scale	0.3%	0.1%	0.1%
	Energy resolution (FWHM) at 5.9 keV	5%	1%	1%
HXD	Absolute effective area	20%	20%	5%
	Relative effective area	10%	10%	5%
	Vignetting	5%	10%	5%
	Background modeling (PIN)	5%	10%	1%
	Background modeling (GSO)	10%	10%	3%
	Absolute timing	N/A	300 μs	100 μs
	Relative timing	N/A	10^{-8}	10^{-10}
	GRB absolute timing	N/A	100 ms	15 ms

Note ··· All the values quoted are preliminary.

a: Valid in the 1–8 keV band. Calibration uncertainty may become larger outside this energy range, especially below 0.3 keV (BI chip) and above 10 keV.

b: For all integration radii from $1'$-$6'$. No error on attitude control is included.

c: As on-axis but for all XIS f.o.v. No calibration is currently scheduled.

The angular resolution does not significantly depend on the energy of the incident X–ray in the energy range of *Suzaku* , 0.2-12 keV. The effective areas are typically 440 cm^2 at 1.5 keV and 250 cm^2 at 8 keV. The focal lengths are 4.75 m for the XRT-I. Individual XRT quadrants have their component focal lengths deviated from the design values by a few cm. The optical axes of the quadrants of each XRT are aligned within $2'$ from the mechanical axis. The field of view for XRT-Is is about $17'$ at 1.5 keV and $13'$ at 8 keV. (see also Table 4.4)

4.3.2.1 Basic Components of XRT

The *Suzaku* X–Ray Telescopes (XRTs) consist of closely nested thin-foil reflectors, reflecting X–ray at small grazing angles. An XRT is a cylindrical structure, having the following layered components: a thermal shield at the entrance aperture to help maintain a uniform temperature; a pre-collimator mounted on metal rings for stray light elimination; a primary stage for the first X–ray reflection; a secondary stage for the second X–ray reflection; a base ring for structural integrity and interface with the EOB of the spacecraft. All these components, except the base rings, are constructed in 90° segments. Four of these quadrants are coupled together by interconnect-couplers and also by the top and base rings (Figure 4.21). The telescope housings are made of aluminum for an optimal strength to mass ratio. Each reflector consists of a substrate also made of aluminum and an epoxy layer that couples the reflecting gold surface to the substrate.

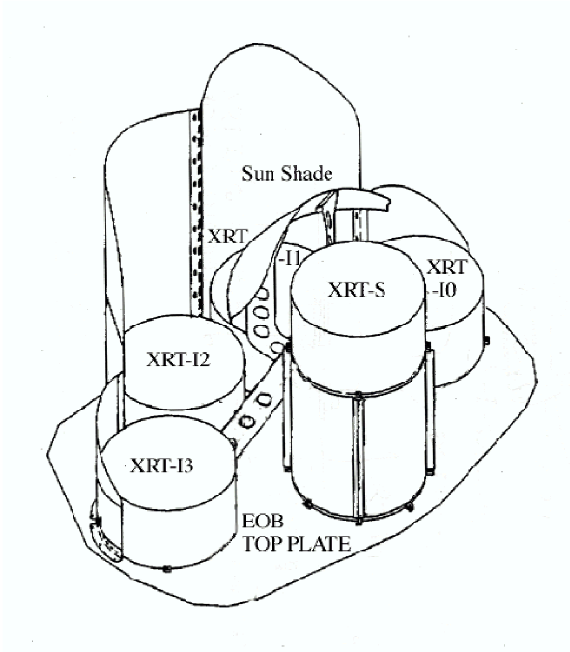

Figure 4.20: Layout of the XRTs on the *Suzaku* spacecraft.

Figure 4.21: A Suzaku X–Ray Telescope

Table 4.6: Telescope Dimensions and Parameters of XRT-I

	Suzaku XRT-I	ASCA
Number of telescopes	4	4
Focal length	4.75 m	3.5 m
Inner Diameter	118 mm	120 mm
Outer Diameter	399 mm	345 mm
Height	279 mm	220 mm
Mass/Telescope	19.5 kg	9.8 kg
Number of nested shells	175	120
Reflectors/Telescope	1400	960
Geometric area/Telescope	873 cm^2	558 cm^2
Reflecting surface	Gold	Gold
Substrate material	Aluminum	Aluminum
Substrate thickness	155 μm	127 μm
Reflector slant height	101.6 mm	101.6 mm

4.3.2.2 Reflectors

In shape, each reflector is a 90° segment of a section of a cone. The cone angle is designed to be the angle of on-axis incidence for the primary stage and 3 times that for the secondary stage. They are 101.6 mm in slant length and with radii extending approximately from 60 mm at the inner part to 200 mm at the outer part. The reflectors are nominally 178 μm in thickness. All reflectors are positioned with grooved alignment bars, which hold the foils at their circular edges. There are 13 alignment bars at each face of each quadrant, separated at approximately 6.4° apart.

To properly reflect and focus X–ray at grazing incidence, the precision of the reflector figure and the smoothness of the reflector surface are important aspects. Since polishing of thin reflectors is both impractical and expensive, reflectors in *Suzaku* XRTs acquire their surface smoothness by a replication technique and their shape by thermo-forming of aluminum. In the replication method, metallic gold is deposited on extrusion glass mandrel ("replication mandrel"), of which the surface has sub-nanometer smoothness over a wide spatial frequency, and the substrate is subsequently bonded with the metallic film with a layer of epoxy. After the epoxy is hardened, the substrate-epoxy-gold film composite can be removed from the glass mandrel and the replica acquires the smoothness of the glass. The replica typically has ∼0.5 nm rms roughness in the mm or smaller spatial scale, which is sufficient for excellent reflectivity at incident angle less than the critical angle. The *Suzaku* XRTs are designed with on-axis reflection at less than critical angle, which is approximately inversely proportional to X–ray energy.

In the thermo-forming of the substrate, pre-cut, mechanically rolled aluminum foils are pressed onto a precisely shaped "forming mandrel", which is not the same as the replication mandrel. The combination is then heated until the aluminum softened. The aluminum foils acquire the figure of the properly shaped mandrel after cooling and release of pressure. In the *Suzaku* XRTs, the conical approximation of the Wolter-I type geometry is used. This approximation fundamentally limits the angle resolution achievable. More significantly, the combination of the figure error in the replication mandrels and the imperfection in the thermo-forming process (to about 4 micrometers in the low frequency components of the figure error in the axial direction) limits the angular resolution to about 1 minute of arc.

4.3.2.3 Pre-collimator

The pre-collimator, which blocks off stray light that otherwise would enter the detector at a larger angle than intended, consists of concentrically nested aluminum foils similar to that of the reflector substrates. They are shorter, 22 mm in length, and thinner, 120 micrometers in thickness. They are positioned in a fashion similar to that of the reflectors, by 13 grooved aluminum plates at each circular edge of the pieces. They are installed on top of their respective primary reflectors along the axial direction. Due to their smaller thickness, they do not significantly reduce the entrance aperture in that direction more than the reflectors already do. Pre-collimator foils do not have reflective surfaces (neither front nor back). The relevant dimensions are listed in Table 4.7.

Table 4.7: Design Parameters for Pre-collimator

	XRT-I
Number of Collimators	4
Height	32 mm
Blade Substrate	Aluminum
Blade Thickness	120 μm
Blade Height	22 mm
Height from Blade Top to Reflector Top	30 mm
Number of nested shells	175
Blade/Telescope	700
Mass/Collimator	2.7 kg

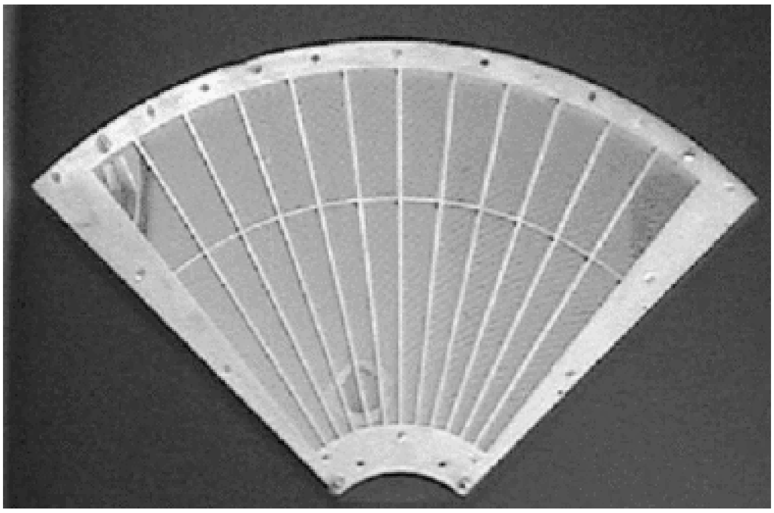

Figure 4.22: A thermal shield.

4.3.2.4 Thermal Shields

The *Suzaku* XRTs are designed to function in a thermal environment of 20±7.5°C. The reflectors, due to its composite nature and thus its mismatch in coefficients of thermal expansion, suffer from thermal distortion that degrades the angular resolution of the telescopes in temperature outside this range. Thermal gradient also distorts the telescope in a larger scale. Even though sun shields and other heating elements on the spacecraft help in maintaining a reasonable thermal environment, thermal shields are integrated on top of the pre-collimator stage to provide the needed thermal control.

4.3.2.5 XRT-I Performance in Orbit

The four XISs (cf. Fig. 4.30) are true imagers, with a large field of view ($\sim 18' \times 18'$), and moderate spectral resolution. Each of the co-aligned XRTs features an X–ray mirror with an angular resolution (expressed as Half-Power Diameter, or HPD) of $\sim 2'$. Figure 4.23 shows the total effective area of the XIS+XRT, which includes features due to the elemental composition of the XIS and XRT. K-shell absorption edges from the oxygen (0.54 keV) and aluminum (1.56 keV) in the blocking filters are present, as well as a number of weak M-shell

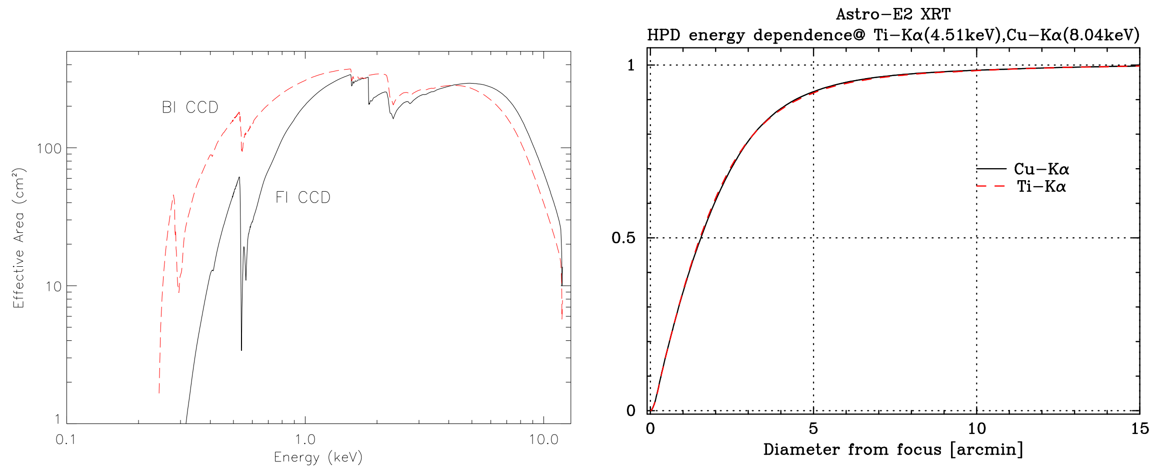

Figure 4.23: Left: XIS Effective area of one XRT + XIS system, for both the FI and BI chips. Right: The Encircled Energy Function (EEF) showing the fractional energy within a given radius for one quadrant of the XRT-I telescopes on *Suzaku* at 4.5 and 8.0 keV.

features between 2–3 keV arising from the gold in the XRT.

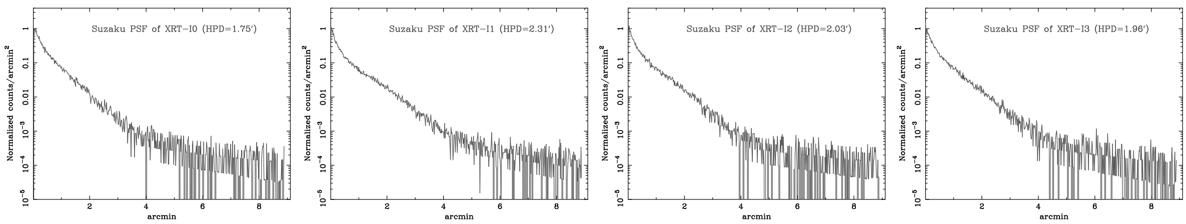

Figure 4.24: Point spread functions of the XRT–XIS modules for the XRT-I0 through XRT-I3 from left to right. Each PSF is normalized by the number of total photons collected over the entire XIS aperture.

Fig. 4.24 shows the point spread functions (PSFs) of all the XRT-I+XIS modules, measured using a observation of a point-like source MCG−6−30-15. The preliminary HPD, with a typical statistical error of $\sim 0'.1$, ranges from $1'.8 \sim 2'.3$. Figure 4.25 shows the focal position of the XRT-Is, that the source is focused when the satellite points at the XIS aimpoint. The focal positions locate roughly within $0'.5$ from the detector center with an deviation of $\sim 0'.3$. This implies that the fields of view of the XIS coinsides each other within $\sim 0'.3$.

A series of offset observations of the Crab observations were carried out in August and Septemper at various off-axis angles of $0'$, $3'.5$, $7'$. The intensity of the Crab nebula is evaluated for each pointing and for each XIS module separately. By finding the maximum throughput angle, we also have obtained a direction of the optical axis of each telescope. The result is shown in Fig. 4.26. The optical axes locate roughly within $1'$ from the XIS aim point. This implies that the efficiency of all the XRT-Is is more than 97 % even at 10 keV when we observe a point source on the XIS aimpoint. By assuming the detector efficiency is constant over the field of view, we determined the vignetting function as shown in Figure 4.27. The vignetting function is narrower in higher energy. The averaged effective area over the detector size of XIS ($17.8'$x$17.8'$) is 60%, 60% and 50% of the E.A on axis at 1.5, 4.5 and 8.0 keV, respectively.

In-flight stray-light observations were carried out with Crab at off-axis angles of $20'$ (4

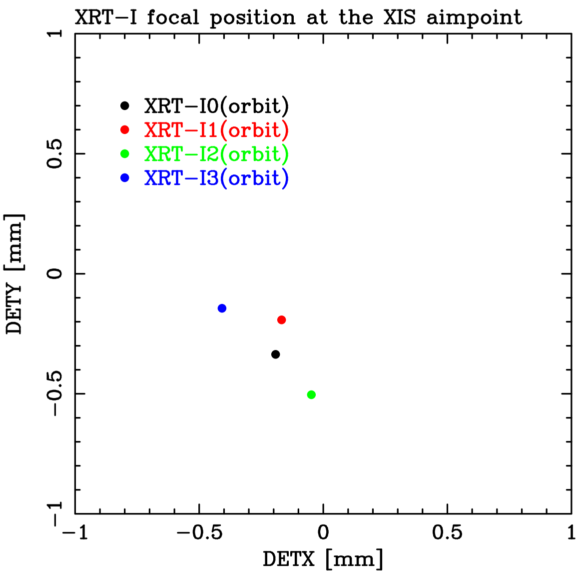

Figure 4.25: Focal positions at the XISs when the satellite points MCG−6−30-15 at the XIS aimpoint.

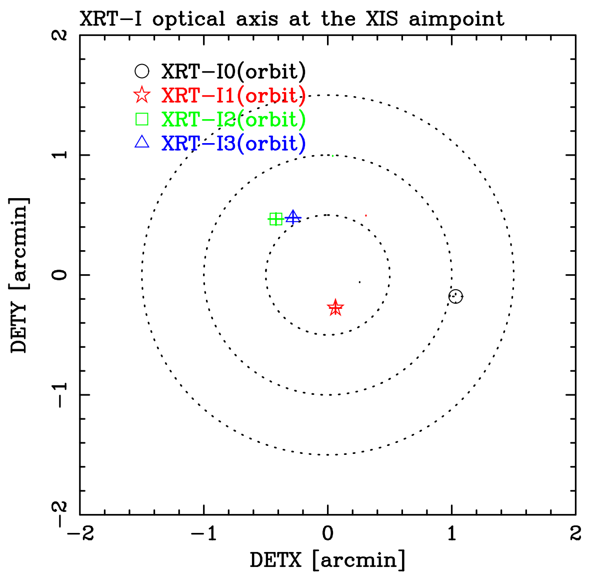

Figure 4.26: Optical axis directions of the XIS-S0 through S3. The optical axis of the XRT-I0 (XIS-S0), for example, locates at $(1\overset{\prime}{.}0,\ -0\overset{\prime}{.}2)$, which implies that the maximum throughput is achieved for XRT-I0 when the satellite points at the XIS aimpoint.

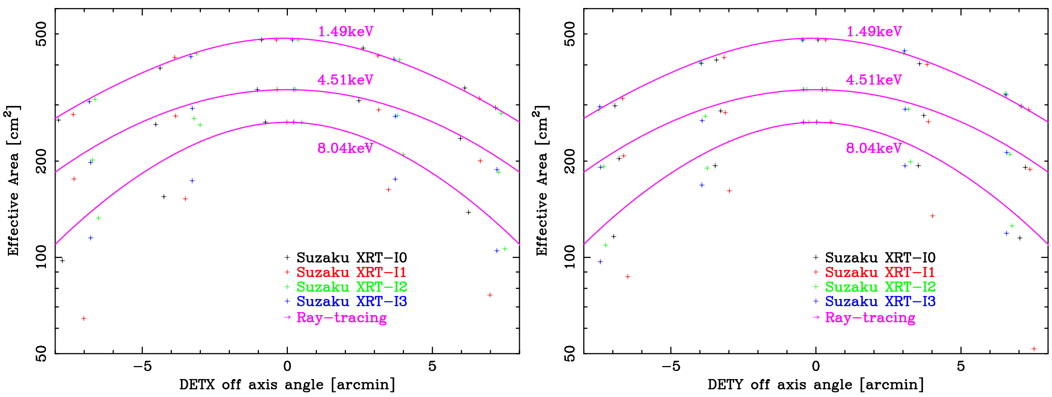

Figure 4.27: Vignetting curves of XRT-I at three different energies of 1.5, 4.5 and 8.0 keV. The three solid lines in the plots correspond to a parameter of ray-tracing program while the crosses are the preliminary XRT-I effective area "inferred" from the Crab pointings with some assumptions. The XRT-I effective area shown here does not includes either the quantum efficiency of the detector or transmissivity of the thermal shield and the optical blocking filter.

pointings), 50′ (4 pointing) and 120′ (4 pointing) in August and September. It was found that the pre-collimator works for reducing the stray light in orbit. Figure 4.28 shows angular responses of the XRT-I at 1.5 and 4.5 keV up to 2 degrees. The effective area is normalized at on-axis. The integration area is corresponding to the detector size of XIS $(17'.8 \times 17'.8)$.

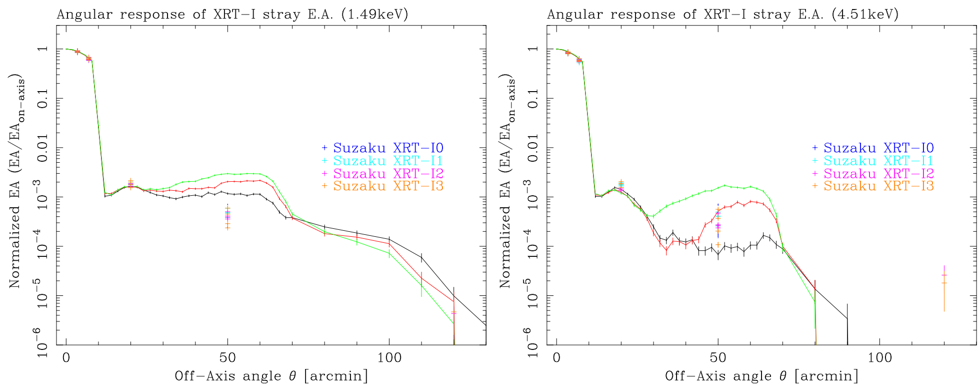

Figure 4.28: Angular responses of the XRT-I at 1.5 (left) and 4.5 keV (right) up to 2 degrees. The effective area is normalized at on-axis. The integration area is corresponding to the detector size of XIS ($17'.8 \times 17'.8$). The three solid lines in the plots correspond to different parameters of ray-tracing program while the crosses are the normalized effective area using the Crab pointings.

The plots are necessary to plan observations of diffuse sources or faint emissions near bright sources, such as outskirts of cluster of galaxies, diffuse objects in the Galactic plane, SN 1987A, etc.

The three solid lines in the plots correspond to different parameters of ray-tracing program while the crosses are the normalized effective area using the Crab pointings. For example, the effective area of the stray lights at 1.5 keV is $\sim 10^{-3}$ at angles smaller than 70 arcmin off axis and $< 10^{-3}$ at angles larger than 70 arcmin off. The measured flux of stray lights are in good agreement with that of raytracing within an order.

4.3.3 X–ray Imaging Spectrometer (XIS)

4.3.3.1 Overview of the XIS

Suzaku has four X–ray Imaging Spectrometers (XISs), which are shown in Figure 4.29. These employ X–ray sensitive silicon charge-coupled devices (CCDs), which are operated in a photon-counting mode, similar to that used in the ASCA SIS, *Chandra* ACIS, and *XMM-Newton* EPIC. The four *Suzaku* XISs are named XIS-S0, S1, S2 and S3, each located in the focal plane of an X–ray Telescope; those telescopes are known respectively as XRT-I0, XRT-I1, XRT-I2, and XRT-I3. Each CCD camera has a single CCD chip with an array of 1024×1024 picture elements ("pixels"), and covers an $18' \times 18'$ region on the sky. Each pixel is 24 μm square, and the size of the CCD is 25 mm $\times$ 25 mm. One of the XISs, XIS-S1, uses a back-side illuminated CCDs, while the other three use front-side illuminated CCDs.

A CCD has a gate structure on one surface to transfer the charge packets to the readout gate. The surface of the chip with the gate structure is called the "front side". A front-side illuminated CCD (FI CCD) detects X-ray photons that pass through its gate structures, i.e. from the front side. Because of the additional photo-electric absorption at the gate structure, the low-energy quantum detection efficiency (QDE) of the FI CCD is rather limited. Conversely, a back-side illuminated CCD (BI CCD) receives photons from "back," or the side without the gate structures. For this purpose, the undepleted layer of the CCD is com-

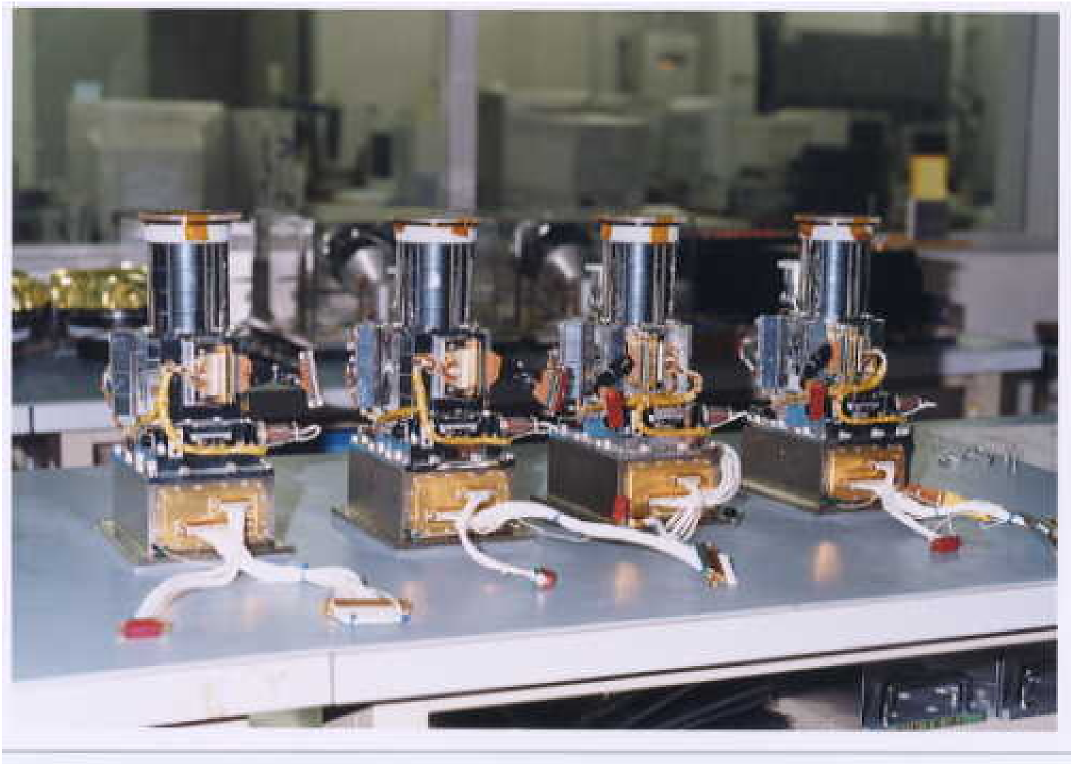

Figure 4.29: The four XIS detectors before installation onto *Suzaku* .

pletely removed in the BI CCD, and a thin layer to enhance the electron collection efficiency is added in the back surface. A BI CCD retains a high QDE even in sub-keV energy band because of the absence of gate structure on the photon-detection side. However, a BI CCD tends to have a slightly thinner depletion layer, and the QDE is therefore slightly lower in the high energy band. The decision to use only one BI CCD and three FI CCDs was made because of both the slight additional risk involved in the new technology BI CCDs and the need to balance the overall efficiency for both low and high energy photons. To minimize the thermal noise, the sensors need to be kept at ~ -90°C during observations.

To reduce contamination of the X–ray signal by optical and UV light, each XIS has an Optical Blocking Filter (OBF) located in front of it. The OBF is made of polyimide with a thickness of 1000 Å, coated with a total of 1200 Å of aluminum (400 Å on one side and 800 Å on the other side). To facilitate the in-flight calibration of the XISs, each CCD sensor has two ^{55}Fe calibration sources. One is installed on the door to illuminate the whole chip, while the other is located on the side wall of the housing and is collimated in order to illuminate two corners of the CCD. The door-mounted source will be used for initial calibration only; once the door is opened, it will not illuminate the CCD. The collimated source can easily be seen in two corners of each CCD. A small number of these X–rays scatter onto the entire CCD. In addition to the emission lines created by these sources, we can utilize a new feature of the XIS CCDs, "charge injection capability," to assist with calibration. This allows an arbitrary amount of charge to be input to the pixels at the top row of the imaging region (exposure area), i.e. the far side from the frame-store region. The charge injection capability may be used to measure the CTI (charge transfer inefficiency) of each column, or even to reduce the CTI. The latter usage, so-called spaced-row CI, is successfully demonstrated in

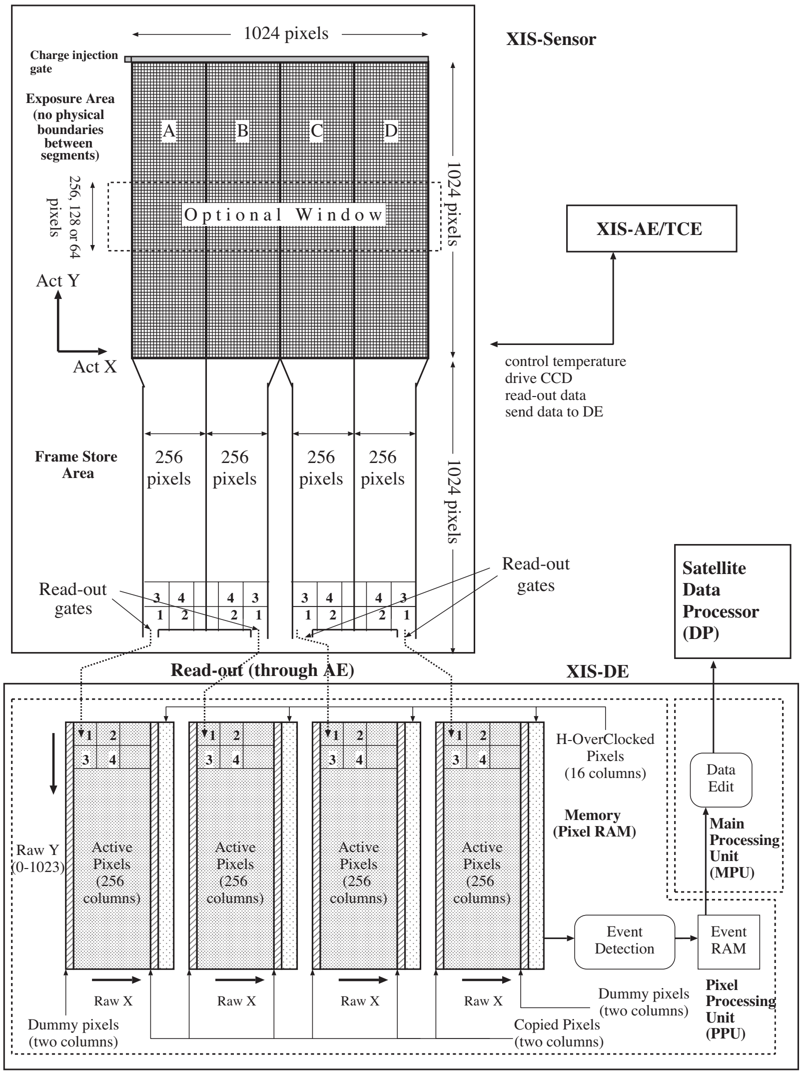

Figure 4.30: One XIS instrument. Each XIS consists of a single CCD chip with 1024×1024 X–ray sensitive cells, each 24 μm square. *Suzaku* contains four CCD sensors (XIS-S0 to S3), two AE/TCUs (AE/TCE01 and AE/TCE23), two PPUs (PPU01 and PPU23), and one MPU. AE/TCU01 and PPU01 service XIS-S0 and XIS-S1, while AE/TCE23 and PPU23 service XIS-S2 and XIS-S3. Three of the XIS CCDs are front-illuminated (FI) and one (XIS-S1) is back-illuminated (BI).

2006.

Fig. 4.30 provides a schematic view of the XIS system. Charge clouds produced in the CCD by the X–rays focused by the XRT are accumulated on the exposure area for a certain exposure period (typically 8 s in the "normal" mode), and the data are transferred to the Frame Store Area (FSA) after each exposure. Data stored in the Frame Store Area are read-out sequentially by the AE, and sent to the PPU after the conversion to the digital data. The data are put into the memory in PPU named Pixel RAM. Subsequent data processing is done by accessing the Pixel RAM.

4.3.3.2 Pulse Height Determination, and Hot Pixels

When a CCD pixel absorbs an X–ray photon, the X–ray is converted to an electric charge, which in turn produces a voltage at the analog output of the CCD. This voltage ("pulse-height") is proportional to the energy of the incident X–ray. In order to determine the true pulse-height corresponding to the input X–ray energy, it is necessary to subtract *Dark Levels* and correct possible *optical Light Leaks*. XIS has capability to measure them on-board.

Hot pixels are pixels which always output over threshold pulse-heights even without input signals. Hot pixels are not usable for observation, and their output has to be disregarded during scientific analysis. In the case of XIS, hot pixels are detected on-board and their positions and pulse-heights are stored in the Hot-pixel RAM and sent to the telemetry. Thus, hot pixels can be recognized on-board, and they are excluded from the event detection processes. It is also possible to specify the hot pixels manually. There are, however, some pixels which output over threshold pulse-heights intermittently. Such pixels are called flickering pixels. It is difficult to identify and remove the flickering pixels on board; they are inevitably output to the telemetry and need to be removed during the ground processing. Flickering pixels sometimes cluster around specific columns, which makes it relatively easy to identify.

4.3.3.3 Photon pile-up

The XIS is essentially a position-sensitive integrating instrument, with the nominal interval between readouts of 8 s. If during the integration time one or more photons strike the same CCD pixel, or one of its immediate neighbors, these cannot be correctly detected as independent photons: this is the phenomenon of photon pile-up. Here, the modest angular resolution of the *Suzaku* XRT is an advantage: the central 3×3 pixel area receives 2% of the total counts of a point source, and $\sim$10% of the counts fall within $\sim$0.15 arcmin of the image center. The pile-up effect is negligible for the object studied in this thesis.

4.3.3.4 XIS background rate

All four XISs have low backgrounds, due to a combination of the *Suzaku* orbit and the instrumental design. Below 1 keV, the high sensitivity and energy resolution of the XIS-S1 combined with this low background means that *Suzaku* is the superior instrument for observing soft sources with low surface brightness. At the same time, the large effective area at Fe K (comparable to the XMM pn) combined with this low background make *Suzaku* a powerful tool for investigating hot and/or high energy sources as well.

In the XIS, the background originates from the cosmic X–ray background (CXB) combined with charged particles (the non-X–ray background, or NXB). When observing the dark earth (*i.e.* the NXB), the background rate between 1-12 keV in is 0.11 cts/s in the FI CCDs and 0.40 cts/s in the BI CCD; see Figure 4.31. Note that these are the fluxes after the grade selection is applied with only grade 0, 2, 3, 4 and 6 selected. There are also fluorescence features arising from the calibration source as well as material in the XIS and XRTs. The Mn lines are due to the scattered X-rays from the calibration sources. As shown in Table 4.8 the Mn lines are almost negligible except for XIS-S0. The O lines are mostly contamination from the day earth (4.3.3.4.2). The other lines are fluorescent lines from the material used for the sensor. Table 4.8 shows the current best estimates for the strength of these emission

Table 4.8: Major XIS Background Emission Lines

Line	Energy keV	XIS-S0 10^{-9} ct/s/pix	XIS-S1 10^{-9} ct/s/pix	XIS-S2 10^{-9} ct/s/pix	XIS-S3 10^{-9} ct/s/pix
O K	0.5249	18.5 ± 0.5	$69.3^{+2.7}_{-2.6}$	$14.3^{+1.5}_{-1.3}$	$14.1^{+1.1}_{-1.2}$
Al K	1.846	1.98 ± 0.23	3.01 ± 0.51	$1.50^{+0.31}_{-0.28}$	$1.57^{+0.25}_{-0.23}$
Si K	2.307	$0.299^{+0.2080}_{-0.2074}$	2.21 ± 0.45	$0.0644(< 0.282)$	$0.543^{+0.212}_{-0.213}$
Au M	2.1229	0.581 ± 0.234	$1.13^{+0.280}_{-0.291}$	$0.359^{+0.211}_{-0.212}$	$6.69^{+2.91}_{-2.90}$
Mn Kα	5.898	$8.35^{+0.36}_{-0.34}$	0.648 ± 0.289	$0.299^{+0.209}_{-0.2086}$	$0.394^{+0.181}_{-0.18}$
Mn Kβ	6.490	$1.03^{+0.22}_{-0.216}$	$0.294(< 0.649)$	$0.00(< 0.111)$	$0.428^{+0.225}_{-0.226}$
Ni Kα	7.470	7.20 ± 0.31	6.24 ± 0.53	$3.78^{+0.26}_{-0.25}$	$7.13^{+0.36}_{-0.37}$
Ni Kβ	8.265	0.583 ± 0.183	$1.15^{+0.5}_{-0.489}$	0.622 ± 0.206	$0.983^{+0.247}_{-0.249}$
Au Lα	9.671	$3.52^{+0.27}_{-0.28}$	$3.28^{+1.16}_{-0.99}$	$1.88^{+0.31}_{-0.28}$	$3.54^{+0.36}_{-0.35}$
Au Lβ	11.514	$2.25^{+0.73}_{-0.59}$	2.91 ± 1.29	$0.752^{+0.428}_{-0.304}$	$2.67^{+0.61}_{-0.53}$

Note: Typical accumulation time are 110-160 ks

features, along with their 90% upper and lower limits.

4.3.3.4.1 Out-of-time events X-ray photons detected during the frame-store transfer do not correspond to the true image, but instead appear as a streak or blur in the readout direction. These events are called out-of-time events., and they are an intrinsic feature of CCD detectors. Similar streaks are seen from bright sources observed with *Chandra* and *XMM-Newton* . Out-of-time events produce a tail in the image, which can be an obstacle to detecting a low surface brightness feature in an image around a bright source. Thus the out-of-time events reduce the dynamic range of the detector. Since XIS spends 25 ms in the frame-store transfer, about 0.3% ($= 0.025/8 \times 100$) of all events will be out-of-time events. However, because the orientation of the CCD chip is different among the sensors, one can in principle distinguish a true feature of low surface brightness and the artifact due to the out-of-time events by comparing the images from two or more XISs.

4.3.3.4.2 Day Earth Contamination When the XIS field of view is close to the day earth (i.e. Sun lit Earth), fluorescent lines from the atmosphere contaminate low-energy part of the XIS data, especially in the BI chip. Most prominent is the oxygen line, but the nitrogen line may be also noticed (see Fig. 4.31–right). These lines are mostly removed when we apply the standard data screening criteria (XIS FOV is at least 20 degree away from the day earth) during the ground processing. However, small amount of contamination can remain. This contamination may be further reduced if we subtract appropriate background. This subtraction, however, may be imperfect.

4.3.3.5 Radiation Damage and On-board Calibration of the XIS

The performance of X-ray CCDs gradually degrades in the space environment due to the radiation damage. This generally causes an increase in the dark current and a decrease of the charge transfer efficiency (CTE). In the case of XIS, the increase of the dark current is

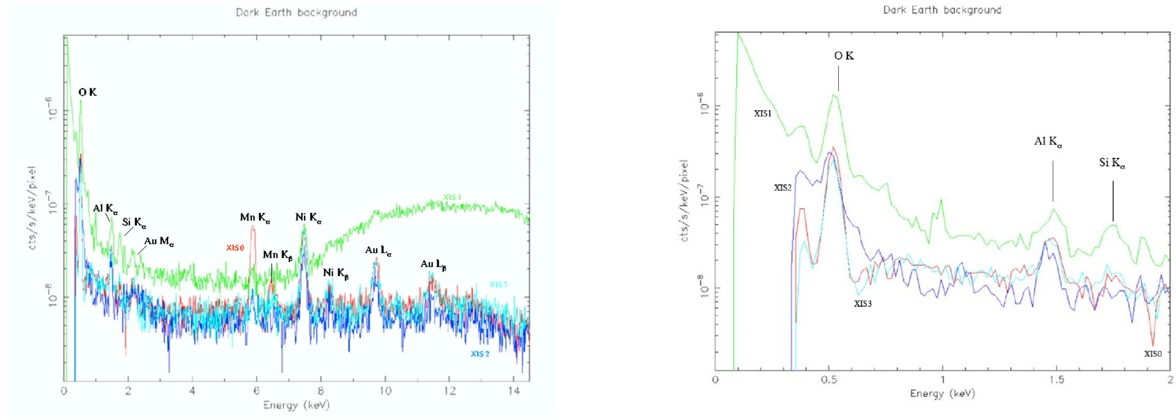

Figure 4.31: The XIS background rate for each of the four XIS detectors. Left: a figure to show the whole energy range with prominent fluorescent lines marked. These spectra are based on $\sim 110 - 160$ ksec of observations towards the dark Earth. Right: showing only energies between 0.1-2.0 keV. Below 0.3 keV the background rate for the FI chips cannot be determined due to their low effective area.

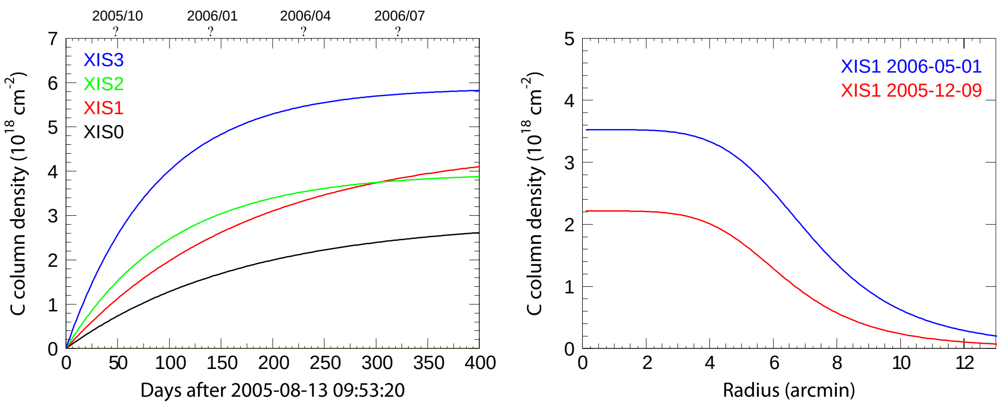

Figure 4.32: Contamination profiles. Left: thickness vs. time; right: position dependence. C/O=6 is assumed.

expected to be small due to the low (–90°C) operating temperature of the CCD. However, a decrease in CTE is unavoidable. Thus, continuous calibration of CCD on orbit is essential to the good performance of the XIS. This is calibrated using a radio isotope source and charge injection as explained below:
(i) Each XIS carries ^{55}Fe calibration sources near the two corners of the chip, which will be used to monitor the instrument gain.
(ii) Each XIS CCD is equipped with charge injection capability, which may be useful to measure and even suppress CTI.

4.3.3.6 Contamination on the OBFs

After the launch of *Suzaku*, a time and position dependent contamination of the XIS optical blocking filter (OBF) was found. The source is probably outgassing from the satellite. The level of contamination increases with time and is different from sensor to sensor. The Suzaku team investigated possible materials that caused the contamination and found DEHP (a kind of rubber), which evaporates in high temperature is a candidate. The composition of DEHP is $C_{24}H_{38}O_4$, i.e., C/O=6. The time and position dependence of the contamination thickness has been empirically modeled by the XIS team as shown in Figure 4.32, assuming C/O=6. The uncertainties in composition, thickness and position dependence produce the largest systematic uncertainty on the effective area and response functions, in particular for diffuse emissions, at the time of this study.

4.3.3.7 On-ground event selection

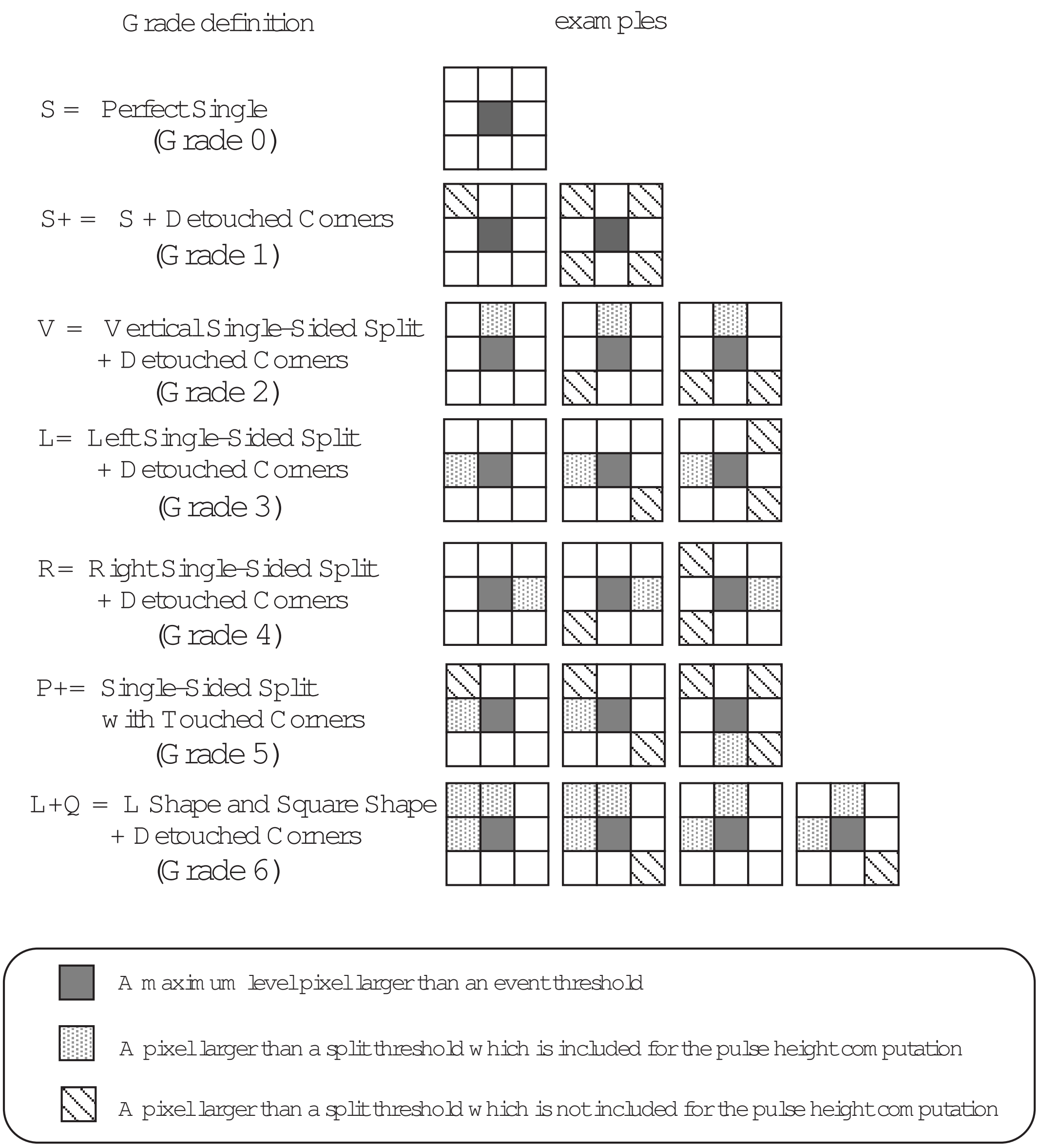

Figure 4.33: Definition of GRADE of CCD events.

Internal (non X-ray) background events can be effectively removed using the pattern on CCD pixels (GRADE), the position (STATUS) and time of an event. The definition of

GRADE is shown in Figure 4.33. Most of X-ray events take GRADE = 0, 2, 3, 4, or 6. On the other hand, most of the events of other GRADEs are dominated by non X-ray events, and should be excluded. STATUS parameter stores the information of pixel quality of an event. Known hot pixels, bad CTE columns, flickering pixels, and pixels on the segment boundaries can be removed by selecting the events with STATUS< 131072. The parameters used in good time interval (GTI) selection are shown in Table 4.9. The signal to noise ratio can be improved with an appropreate GTI criteria, indicated in Table 4.9.

Table 4.9: Parameters used in GTI selection of *Suzaku*

Parameter	Definition	Recommended value to use
SAA	Whether the satellite was in the SAA[a] or not	eq.0
T_SAA	Time after the last SAA duration (s)	> 255
ELV	Elevetion angle from the Earth limb (degree)	> 5
DYE_ELV	Elevation angle from the day Earth limb (degree)	> 20
COR	Cut off rigidity of the cosmic ray (GeV/c/particle)	> 8

[a]: South Atlantic anomaly

Chapter 5

The Coma cluster vicinity

5.1 Observation Summary

The Coma cluster systemic redshift is $z_{\rm com} = 0.0231$ (Struble & Rood, 1999), which yields a scale of 1.68 h_{70}^{-1} Mpc per degree for our assumed cosmology. The redshift dispersion of the cluster galaxies is $\sigma_{\rm gal} = 3.44 \times 10^{-3}$.

We made five observations of X Comae with *XMM-Newton* in 2004 and 2005 for a total of 451.8 ks. As shown in Figure 3.1, it is $26'.5$ or $0.74 h_{70}^{-1}$ Mpc or 0.31 r_{200} north of the cluster center, defined to be at NGC 4874. Its redshift is 0.091±0.001 (Branduardi-Raymont et al., 1985). The instrument mode and the filter used are shown in Table 5.1, and the gross and net exposure time and flux of X Comae are summarized in Table 5.2. Unfortunately, X Comae had a flux at or below its hitherto historical low during our observations.

Table 5.1: Instrument mode

Instrument	Mode	Filter
RGS	Spectro+Q	—
EPIC pn	Full frame	Medium
EPIC MOS	Full frame	Thin

Table 5.2: Exposure times and fluxes of X Comae

Date	Duration ks	Net exposure[a] ks	Flux[a] (0.3–2.0 keV) ergs cm^{-2} s^{-1}
2004 June 6	102.6	71.5	1.92×10^{-12}
2004 June 18	108.3	54.7	1.48×10^{-12}
2004 July 12	104.2	45.6	1.36×10^{-12}
2005 June 27	55.9	23.9	1.02×10^{-12}
2005 June 28	80.8	62.5	1.46×10^{-12}
Total	451.8	259.7	1.66×10^{-12}

[a] For RGS spectra

Table 5.3: Results of fitting the RGS spectra with broken power law models

Component	Value
$N_{\rm H}$	9.3×10^{19} cm^{-2} (fixed)
Source Γ ($E < 0.75$ keV)	$1.74^{+0.15}_{-0.29}$
Source Γ ($E > 0.75$ keV)	2.41 ± 0.25
Source Normalization^a	$(6.88^{+0.72}_{-0.66}) \times 10^{-4}$
Background Γ ($E < 0.75$ keV)	$3.73^{+0.18}_{-0.12}$
Background Γ ($E > 0.75$ keV)	1.96 ± 0.23
Background Normalization^a	$(0.79 \pm 0.08) \times 10^{-4}$
C-statistic	708.63
free parameters	6
d.o.f.	628

^{a}: in units of photons keV^{-1} cm^{-2} s^{-1} at 1 keV

5.2 Absorption lines in the RGS spectra

5.2.1 Data reduction

We reduced the RGS data using the XMM-Newton Science Analysis System (SAS) version 6.1.0, with standard parameters. We checked the data from a source-free region of CCD 9 for background flares. The regions were CHIPX = 2 to 341, CHIPY = 2 to 38 and 87 to 127 for RGS1 and CHIPX = 2 to 284, CHIPY = 2 to 37 and 87 to 127 for RGS2. We accumulated signal photons only when the count rates in these regions were less than 0.1 s^{-1} (in PI range 80–3000) for both RGS1 and 2. This rather severe threshold was determined empirically to yield the highest signal to noise background subtracted source spectrum. The net exposure time was about 60 % of the total exposure and is summarized in Table 5.2.

The spectra were extracted after merging the five data sets and then binned by a factor of four, resulting in a final bin width of 0.035 Å at 11.5 Å and 0.046 Å at 23 Å. These bin width are about half of the average FWHM wavelength resolution of the RGS (0.067 Å). The redshift widths corresponding to the resolution are 0.0058 and 0.0029 at 11.5 Å and 23 Å respectively. The dispersion angle vs. cross dispersion angle images and dispersion angle vs. PI plots (so called banana plots) are shown in Figure 5.1. The source spectra contain the events only in the region between the blue lines in the dispersion vs. cross dispersion image *and* in the lower curved region between blue lines in the banana plot. The background spectra were extracted from the region *outside* the blue line regions of the dispersion vs. cross dispersion plot. Only the events in the same region in the banana plot as the source spectra were extracted. The background spectra were then scaled to account for the different areas used in accumulating the source and background photons. Since the number of photons is small, we used the C-statistic (maximum-likelihood) method for model fitting of RGS spectra. The systematic uncertainty in the absolute energy scale of RGS is 8 mÅ(rms) at 19 Å.

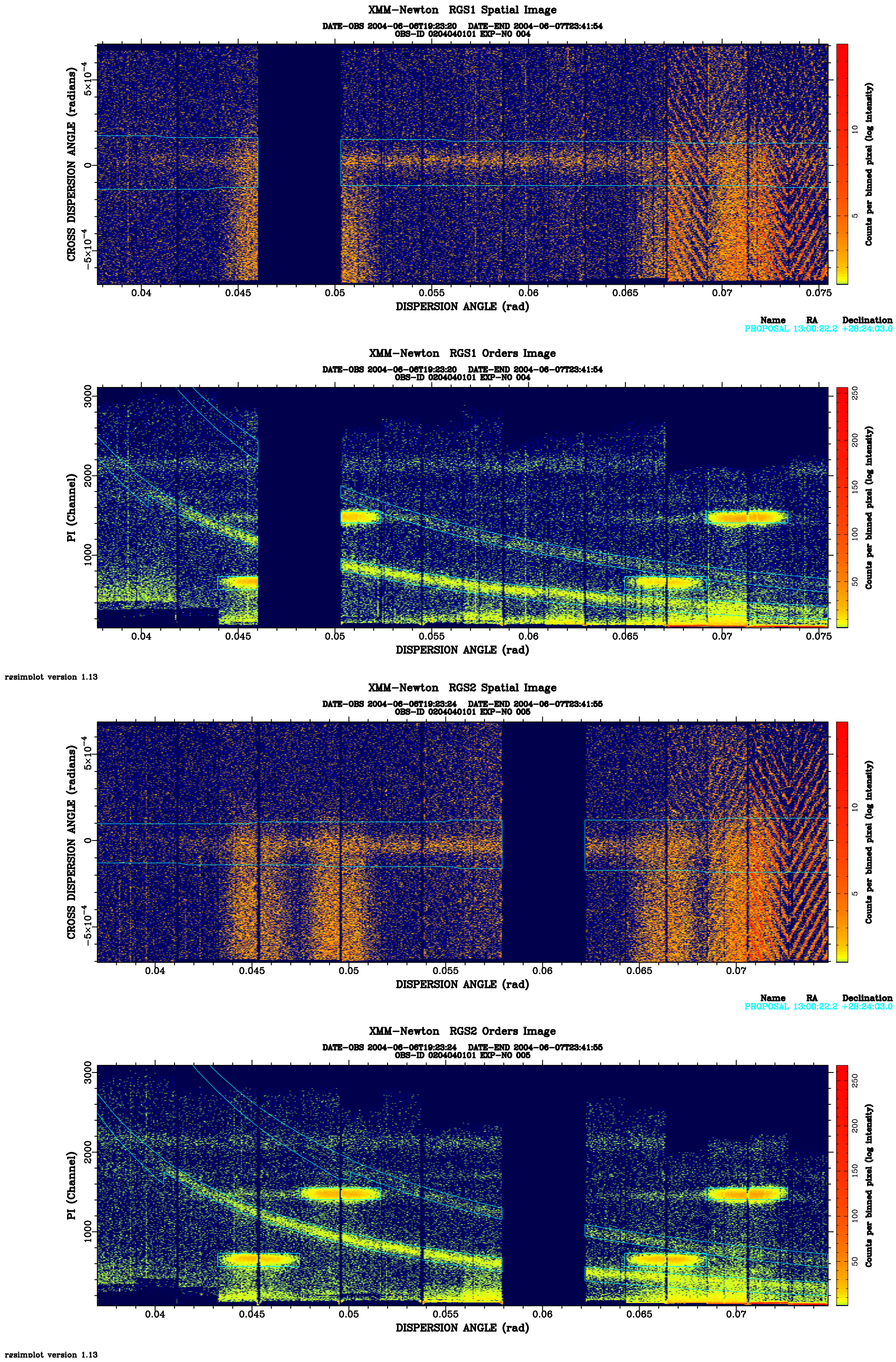

Figure 5.1: Dispersion angle vs. cross dispersion angle (the first image for RGS1 and the third for RGS2) and PI ('banana plot'; the second for RGS1 and the fourth for RGS2). The events in both the blue line in the dispersion vs. cross dispersion angle and the lower curved blue-line region in the banana plot were extracted into the spectra. CCD 9, used to check the background flares is the leftmost one.

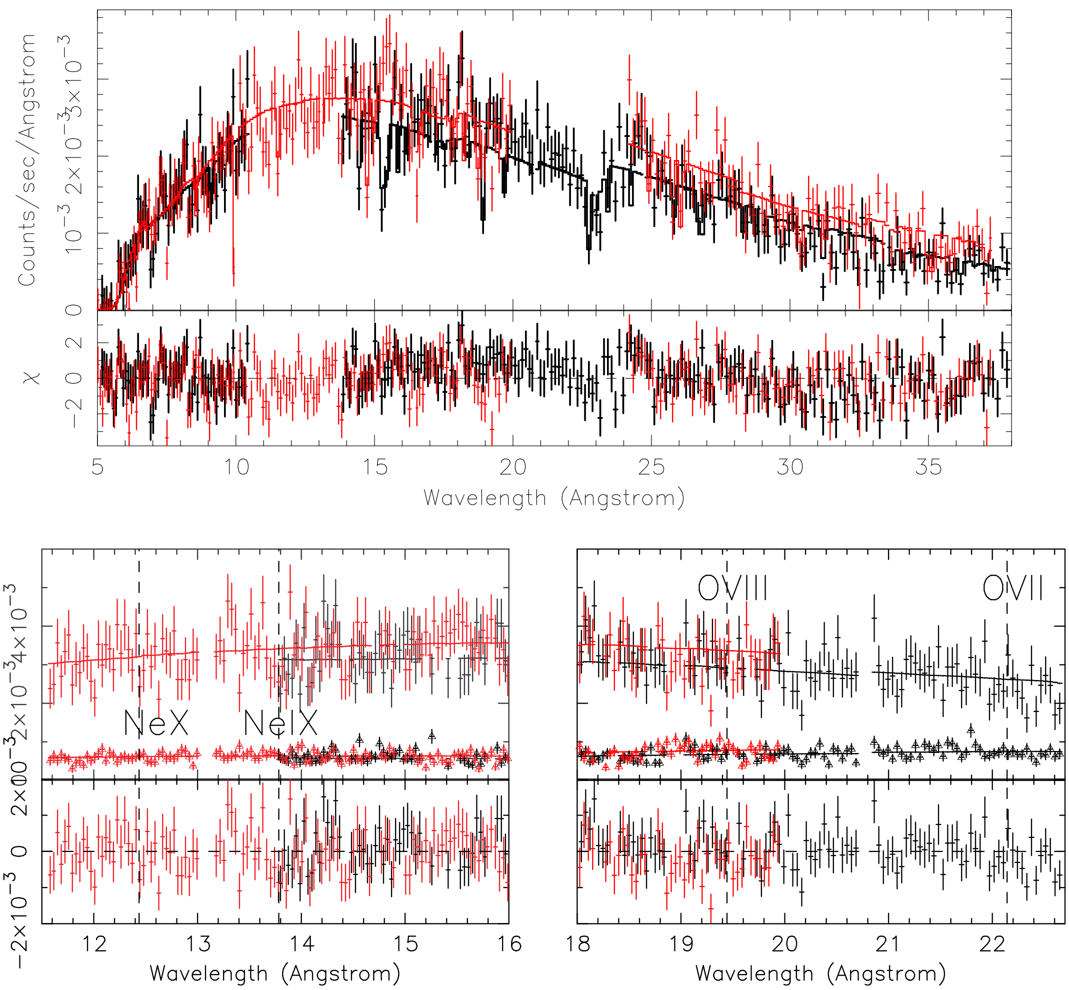

Figure 5.2: X Comae spectra obtained with RGS. Top: spectrum of whole wavelength range after subtraction of background data. The bin widths are three times larger than the spectra of bottom panels. Note that this data was not used for model fitting. Bottom left: spectra around Ne Kα lines. Bottom right: spectra around O Kα lines. Black and red represent RGS1 and RGS2, while crosses (+) and triangles ($\triangle$) show source and background, respectively. The solid lines show the best fit model. The wavelengths corresponding to redshifted Ne, O and Fe lines ($z = 0.0231$) are indicated with vertical dashed lines in the bottom figures. The residuals against the best fit model are also shown in the lower panel of each figure.

5.2.2 Detection of absorption features and their equivalent widths

Figure 5.2 shows the RGS spectra of X Comae. Top panel shows the whole spectrum, while bottom panels show the spectra in the Ne region (11.5–14.5 Å) and the O region (18.0–23.0 Å). The whole spectra were well fitted with a power-law whose index is ~ 2.0 convolved with Galactic absorption of $N_{\rm H} = 9.3 \times 10^{19}$ cm^{-2}. We calculated the ratio of the data to a continuum-only model in order to estimate the statistical significance of possible absorption features at the wavelengths of Ne IX, Ne X, O VII and O VIII Kα resonance lines of the

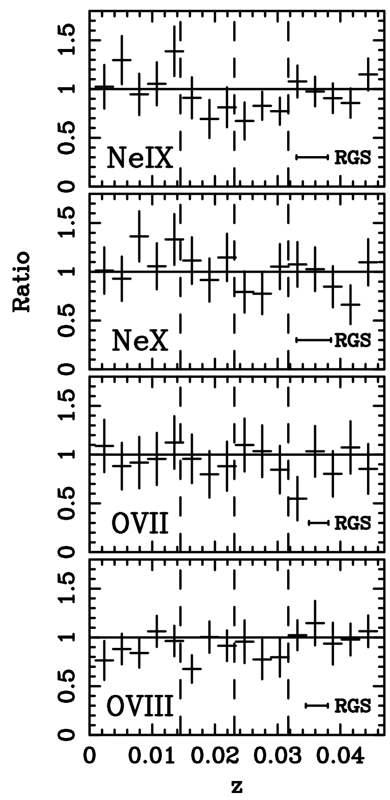

Figure 5.3: Ratios of the data to the the continuum model vs. z for Ne IX, Ne X, O VII, O VIII and Fe XVII (top to bottom). Vertical dashed lines indicate $z_{\rm com}$ and $\pm 2.5 \times \sigma_{\rm gal}$. The average RGS1 and RGS2 instrumental resolution of 0.067 Å (FWHM) corresponds to a redshift resolution of 0.0050, 0.0055, 0.0031 and 0.0035 (top to bottom), which is indicated as a horizontal line at the lower right of each panel.

Coma redshift ($z = 0.0231$) in a model independent way. That is, we calculated

$$\text{Ratio} \equiv \frac{(\text{source} + \text{background data}) - (\text{background data})}{(\text{source} + \text{background model}) - (\text{background model})}. \tag{5.1}$$

This procedure is called the ratio method in what follows.

The source model is a broken power law multiplied by the Galactic absorption of $N_{\rm H} = 9.3 \times 10^{19}$ cm^{-2} (Dickey & Lockman, 1990). The background model is a different broken power law without Galactic absorption. We fitted the source plus background and background spectra of RGS1 and 2 simultaneously using XSPEC version 11.3 in the wavelength region 11.5 Å–22.7 Å. Regions around the Ne IX, Ne X, O VII and O VIII Kα lines, which are defined as $z_{\rm com} - 3\sigma_{\rm gal} < z < z_{\rm com} + 3\sigma_{\rm gal}$, were excluded from the fit.

The best fit model and parameters are shown in Figure 5.2 and in Table 5.3. The ratios around Ne IX, Ne X, O VII and O VIII lines vs. z are shown in Figure 5.3. The FWHM wavelength resolution of RGS is also shown as a horizontal line. We summed the RGS1 and 2 data where both were available. Since the mapping from wavelength to redshift is a function of wavelength, we interpolated the counts to a common redshift bin size for all four lines.

The three vertical dashed lines in Figure 5.3 indicate $z_{\rm com}$ and $z_{\rm com} \pm 2.5 \times \sigma_{\rm gal}$. We

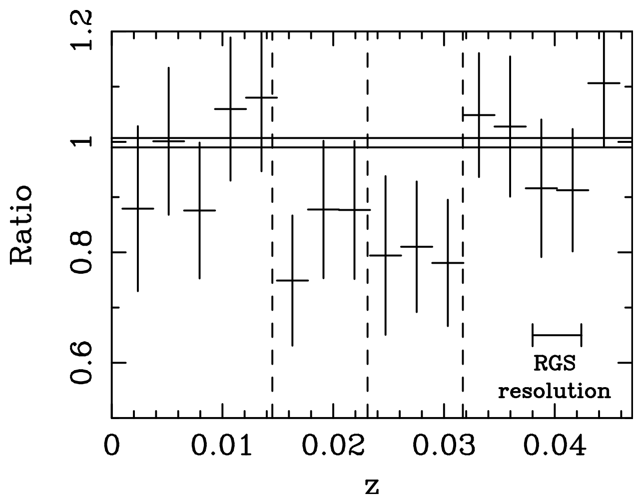

Figure 5.4: Error-weighted average ratio of the data to the the continuum model (as defined in Eq. (5.1)) vs. z for the Ne IX, Ne X, O VII and O VIII lines. Vertical dashed lines indicate $z_{\rm com}$ and $z_{\rm com} \pm 2.5 \times \sigma_{\rm gal}$. The two horizontal lines show the ± 1 σ error of the model normalization. The average of the ratio in the seven bins between the left and right vertical lines is 0.813 ± 0.050. The significance of this absorption is 99.7% according to Monte Carlo simulations. The average of the remaining ten continuum bins is 0.993 ± 0.039, which is consistent with unity. The FWHM averaged wavelength resolution of RGS is also shown as a horizontal line at lower right.

defined redshifts within $z_{\rm com} \pm 2.5 \times \sigma_{\rm gal}$ as absorption and the remainder in Figure 5.3 as continuum, and then calculated the error-weighted average of the absorption and continuum ratios. The results are shown in Table 5.4. When the absorption redshift region was defined, we fixed its center to the *apriori* known $z_{\rm com}$ and chose its width to maximize the Ne IX plus O VIII signal from among 2, 4, 6 or 8 binned-by-four pixels; i.e., the region was determined after a four-trial optimization.

Ne IX is the ion with the deepest absorption, and O VIII is the second deepest. The absorption ratio is below 1 for the Ne X and O VII lines as well, though they are not very significant. The continuum is always consistent with 1. This situation of strong Ne IX absorption and weak absorption by the other three lines is often observed at much higher

Table 5.4: Ratio for continuum and absorption spectral regions[a]

	Continuum region	Absorption region	EW
Ne IX	1.027 ± 0.058	0.782 ± 0.071 (98.0%)	3.3 ± 1.8 eV
Ne X	1.011 ± 0.073	0.950 ± 0.092 (42.7%)	0.8 (< 3.9) eV
O VII	0.908 ± 0.080	0.927 ± 0.103 (50.0%)	0.7 (< 2.6) eV
O VIII	0.963 ± 0.054	0.845 ± 0.071 (94.1%)	1.7 ± 1.3 eV
Avg. of Ne IX and O VIII	0.993 ± 0.039	0.813 ± 0.050 (99.7%)	—

[a]: 68% confidence errors

signal to noise in interstellar medium features in the spectra of galactic X-ray sources (e.g. Yao & Wang, 2005).

To improve the signal-to-noise, we made a grand error-weighted average of the ratios for Ne IX and O XVIII lines and calculated the combined significance. The result is shown in Figure 5.4 where the band around unity is +0.7%, −1.0%, the 1σ error of the model normalization with power law indices fixed at their best fit values. The average of the grand-averaged ratio are also given in Table 5.4.

Since the number of counts in each bin is not very high (20–30 counts/bin), we investigated the significance of the absorption using Monte Carlo simulations. We made 1000 simulated spectra with *no* absorption which have the same statistics and the same response function as the actual data, and then calculated the ratios with the same procedure as above. That is, we calculted the ratio for Ne IX, Ne X, O VII and O VIII lines and grand error-weighted average of the ratios of Ne IX and O VIII. This calculation was done for 2, 4, 6 and 8 binned-by-four pixels around $z_{\rm com}$, and then we chose the most significant grand average among the four trials. The significance of the absorption in our observed RGS data can be estimated as the probability that the simultated spectra without absorption yield a smaller discrepancy from unity. The significance for the grand error-weighted average was 99.7%. We conclude that we have detected absorption by material associated with the Coma cluster with a significance of 99.7%. This significance is equivalent to 3.0σ of a Gaussian distribution. The significance of Ne IX and O VIII was 98.0% (2.3σ) and 94.1% (1.9σ), respectively.

The equivalent width EW of the absorption lines can be calculated from the ratios as $(1 - \text{Ratio}) \times \Delta E$, where ΔE is the energy corresponding to the width of 6 bins we used to calculate the ratios. The EWs for the four lines are also shown in Table 5.4. Assuming that the absorption lines are not saturated, the column density $N_{\rm ion}$ is calculated from EW as

$$N_{\rm ion} = \frac{m_{\rm e} c(1+z)}{\pi h e^2} \frac{EW}{f_{\rm os}}, \tag{5.2}$$

or

$$N_{\rm ion} = 9.11 \times 10^{15}\ {\rm cm}^{-2} \frac{(1+z)}{f_{\rm os}} \frac{EW}{1\ {\rm eV}}, \tag{5.3}$$

(Sarazin, 1989) where $f_{\rm os}$ is the oscillator strength of the transition and the other symbols have their usual meanings. We used $f_{\rm os} = 0.724$ for the Ne IX, $f_{\rm os} = 0.696$ for O VII, and $f_{\rm os} = 0.416$ for Ne X and O VIII (Verner et al., 1996). The column densities of the four lines are then $N_{\rm NeIX} = 4.3 \pm 2.3 \times 10^{16}\ {\rm cm}^{-2}$, $N_{\rm NeX} = 1.9\ (< 8.8) \times 10^{16}\ {\rm cm}^{-2}$, $N_{\rm OVII} = 0.9\ (< 3.5) \times 10^{16}\ {\rm cm}^{-2}$ and $N_{\rm OVIII} = 3.7 \pm 2.8 \times 10^{16}\ {\rm cm}^{-2}$.

5.2.3 Fitting the absorption features and their equivalent widths

Next we derived the equivalent widths of the four lines by another way: using model-fitting of the spectra. We adopted the same contimuum model as that in § 5.2.2, and a boxcar profile to describe the absorption (NOTCH model in XSPEC). This absorption model multiplies the continuum by a factor of

$$\begin{cases} (1-F) & \text{for } (\lambda_{\rm notch} - \frac{W_{\rm notch}}{2}) < \lambda < (\lambda_{\rm notch} + \frac{W_{\rm notch}}{2}) \\ 1 & \text{for all other,} \end{cases} \tag{5.4}$$

Table 5.5: Results of fitting the RGS spectra

Parameter	Unit	Value
		Continuum
$N_{\rm H}$	cm^{-2}	9.3×10^{19} (fixed)
Source Γ ($E < 0.75$ keV)		$1.71^{+0.21}_{-0.26}$
Source Γ ($E > 0.75$ keV)		2.35 ± 0.24
Source Normalization^a		$6.92^{+0.62}_{-0.33} \times 10^{-4}$
Background Γ ($E > 0.75$ keV)		$3.64^{+0.11}_{-0.19}$
Background Γ ($E < 0.75$ keV)		2.01 ± 0.21
Background Normalization^a		$(0.82 \pm 0.07) \times 10^{-4}$
		NeIX 13.447 Å
$\lambda_{\rm notch}{}^b$		0.0231 (fixed)
$W_{\rm notch}{}^b$		9.79×10^{-3}
F		0.41
EW^c		$3.7\ ^{+2.0}_{-2.2}$ eV
$N_{\rm ion}{}^c$	cm^{-2}	$4.7\ ^{+2.6}_{-2.9} \times 10^{16}$
		NeX 12.134 Å
$\lambda_{\rm notch}{}^b$		0.0231 (fixed)
$W_{\rm notch}{}^b$		9.79×10^{-3} (fixed to the NeIX value)
F		0.09
$EW^{c\ d}$	eV	0.8 (<4.7)
$N_{\rm ion}{}^{c\ d}$	cm^{-2}	1.9 (<10.5) $\times 10^{16}$
$EW/EW_{\rm NeIX}{}^d$		0.2 (<1.3)
$N_{\rm ion}/N_{\rm NeIX}{}^d$		0.4 (<2.3)
		OVII 21.602 Å
$\lambda_{\rm notch}{}^b$		0.0231 (fixed)
$W_{\rm notch}{}^b$		9.79×10^{-3} (fixed to the NeIX value)
F		0.04
$EW^{c\ d}$	eV	0.2 (<2.2)
$N_{\rm ion}{}^{c\ d}$	cm^{-2}	0.3 (<2.9) $\times 10^{16}$
$EW/EW_{\rm NeIX}{}^d$		0.06 (<0.59)
$N_{\rm ion}/N_{\rm NeIX}{}^d$		0.06 (<0.63)
		OVIII 18.969 Å
$\lambda_{\rm notch}{}^b$		0.0231 (fixed)
$W_{\rm notch}{}^b$		9.79×10^{-3} (fixed to the NeIX value)
F		0.06
$EW^{c\ d}$	eV	0.4 (<2.2)
$N_{\rm ion}{}^{c\ d}$	cm^{-2}	0.8 (<4.9) $\times 10^{16}$
$EW/EW_{\rm NeIX}{}^d$		0.10 (<0.59)
$N_{\rm ion}/N_{\rm NeIX}{}^d$		0.2 (<1.0)
C-statistic		834.33
Free parameters		11
Degrees of freedom		745

^{a}: In units of photons keV^{-1} cm^{-2} s^{-1} at 1 keV
^{b}: Wavelength converted to redshift
^{c}: Errors include covariance of $W_{\rm notch}$ and F
^{d}: Upper limit is at 2 σ confidence

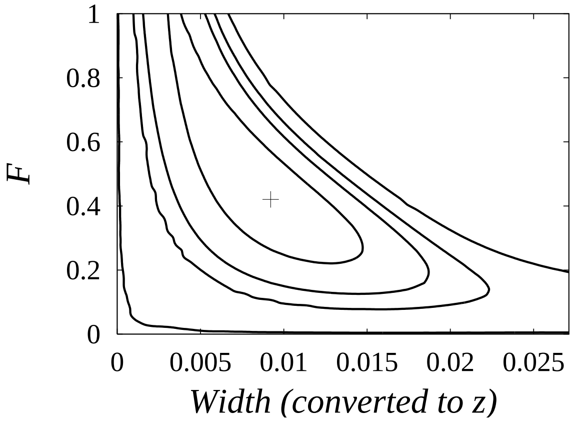

Figure 5.5: Contour plot of ΔC as a function of W_{notch} (converted to redshift) and F for the Ne IX line. Equivalent width is $W_{\mathrm{notch}} \times F$. The four contours are $\Delta C = 1.0$, 2.71, 4.0 and 6.6 corresponding to 68%, 90%, 95% and 99% confidence for one interesting parameter, respectively. These also correspond to 1σ, 1.6σ, 2σ and 2.6σ, respectively if the data were Gaussian distributed.

where λ_{notch}, W_{notch} and F correspond to the central wavelength, width and absorption factor, respectively. The equivalent width is given by $EW = W_{\mathrm{notch}} \times F$. Note that the width is presumably determined by Hubble flow or infall, not by thermal motion. We fixed λ_{notch} to be the value corresponding the redshift of the Coma cluster. Since the significances of the absorption features were low, except for Ne IX, we fitted the Ne IX absorption first and then fitted the other lines with W_{notch} fixed to the best fit Ne IX values (in z, not wavelength). All together the free parameters were: power law indices and normalizations of the source and background continua, W_{notch} and F for Ne IX absorption, and F for the other species. Data between 11.5–22.7 Å were used in the fit.

The best fit parameters are shown in Table 5.5, where λ_{notch} and W_{notch} were converted to redshift. The equivalent widths and their errors were determined taking into account the covariance between W_{notch} and F, as is shown in Figure 5.5 for Ne IX. Figure 5.5 indicates that this analysis is not sensitive to F or W_{notch} because the wavelength resolution of RGS is comparable to the width of the absorption. However, we can estimate the EW, the product of F and W_{notch}, more precisely than either F or W_{notch}. From this figure, the equivalent width of Ne IX is estimated to be $3.7^{+2.0}_{-2.2}$ eV (90% confidence errors). Best fit values and 2σ upper limits are also given in Table 5.5 for the Ne X, O VII and O VIII absorptions. The column density N_{ion} of each ion, estimated from the EW are tabulated in Table 5.5 as well. The derived equivalent widths are consistent within the errors with those obtained from the ratio of the data to the continuum model described in § 5.2.2. Note that these values are about one order of magnitude larger than the column densities of Galactic or local warm-hot gas detected in other observations.

The significance of the line was again calculated using Monte Carlo simulations. The C-statistic was improved by 7.57 when we added the Ne IX absorption line. The probability that the simulated data shows less improvement of the C-statistic was 99.2%, equivalent to 2.7σ if the data were Gaussian distributed (compared to 98.0% from the ratio method). We took this value as the significance of Ne IX line with boxcar-fitting. In the case of boxcar-fitting, the O VIII line is less significant than that found with the ratio method (82.4% compared to 94.1%) and hence combining Ne IX and O VIII absorption did not improve the significance (98.5%) compared to that of Ne IX alone. The significances obtained with boxcar-fitting were slightly different from those by the ratio method, particularly for O VIII. This is probably because the two methods are not exactly identical: with boxcar-fitting the detector response is convolved with an assumed absorption shape (boxcar) that is same for the four lines, while no shape was assumed for the ratio method.

5.2.4 Possible systematic errors

We detected the absorption feature with (statistically) 3.0σ significance, at the redshift of the Coma cluster. Here we investigate possible systematic errors and influence on the significance.

A candidate of systematic error may be that due to the detector response. However, this is negligible compared to the statistical errors. RGS is well calibrated using much brighter sources. We excluded in our analysis the events hit on known bad pixels of the CCD at the focal point of RGS, since bad pixels may cause an artificial structure. Note that uncertainties in the absolute effective area, which is more difficult to calibrate accurately, do not matter in our analysis, since we used ratio or EW.

?? pointed out that merging different observations may introduce artificial absorption features in RGS spectra. However, their suggested features have about one order of magnitude smaller equivalent widths than those we discuss below. They are smaller than our statistical errors. We tried the procedure to search for bad columns that may cause artificial absorptions according to their Appendix C. It showed no apparent artificial features within our statistics.

We also checked whether the distribution of ΔC-statistic is consistent with statistically expected one or not, where ΔC-statistic is the improvement of C-statistic by adding an emission or absorption line in model fitting at an arbitrary wavelength. Model fitting was performed with the line wavelength of every 0.16 Å from 10 Å to 24 Å, where there were sufficient counts. This yields 89 trials. The line width was fixed to the best-fit value of Ne IX absorption obtained in § 5.2.3. Figure 5.6 shows the obtained and statistically expected integrated probability, where integrated probability is defined as the ratio of the number of trials that has larger ΔC-statistic than the value at the horizontal axis, to the total trial number. The consistency of two curves of Figure 5.6 shows that the significance (improvement of C-statistic) is determined by statistics; systematic uncertainties are negligible. We thus concluded that the detection significance of absorption is 3.3σ, even with systematic uncertainties.

5.3 Emission Lines in the EPIC Spectra

5.3.1 Data reduction

After cleaning the duration of background flares, we obtained 240 ks clean EPIC-pn data. This exposure is among the longest ever made of a cluster with *XMM-Newton* and allows us to obtain statistically robust results. We made an ancillary response file (arf) assuming

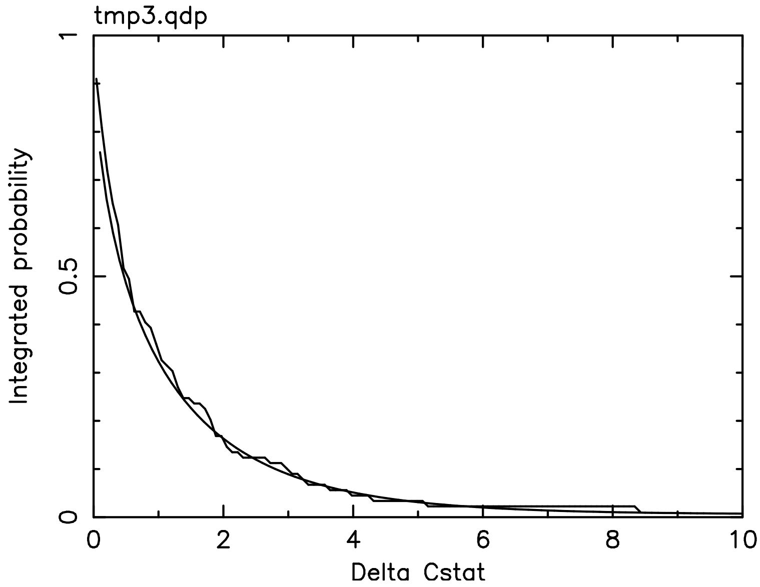

Figure 5.6: Integrated probability vs. ΔC-statistic. Two lines shows the distribution obtained by fitting the spectra of X Comae and one represents the statistically expected distribution, respectively.

Table 5.6: Observations used for Galactic Background estimation

Object	ObsID	Exp. (ksec)	Distance from NGC 4874 (arcmin)
Coma 0	0124711501	15.4	46.2
1253+275	0058940701	10.5	71.6
3C 284	0021740201	34.2	156.4
β Comae	0148680101	29.4	162.7
Average			109.2

a uniform spatial flux distribution of the source to correct the vignetting. Systematic uncertainty of the flux determination is 4%. Here we used only pn data because an improved response matrix for the pn (SAS v6.8) was available. Note that for our analysis the accuracy of the response matrix is much more important than having the highest possible energy resolution.

Determining a reliable background is crucial for this work because the temperatures of the WHIM and the Milky Way interstellar medium are similar and the soft emission in the X Comae field is not very bright. Many previous attempts by other people to measure the soft emission from the Coma cluster (Finoguenov et al., 2003; Kaastra et al., 2003) used *ROSAT* All-Sky Survey (RASS) data to obtain the normalization of the Galactic background model components. Since then there have been several *XMM-Newton* observations serendipitously located around the Coma cluster. Those observations provide data of much higher energy resolution than the RASS data and are therefore preferable for our analysis. We have examined the RASS data at the location of these fields to determine whether they are

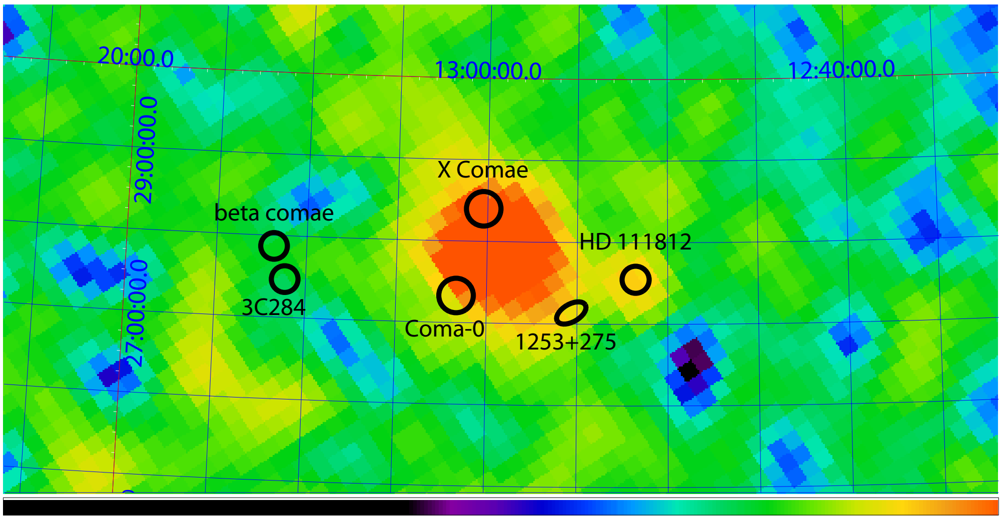

Figure 5.7: A map of *ROSAT* R4 band and the position of observation with *XMM-Newton*.

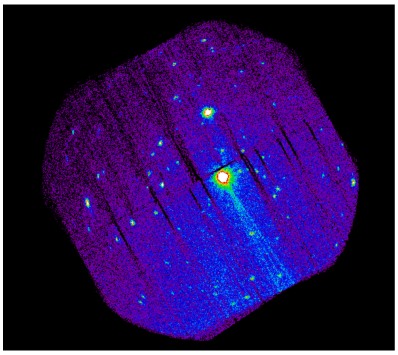

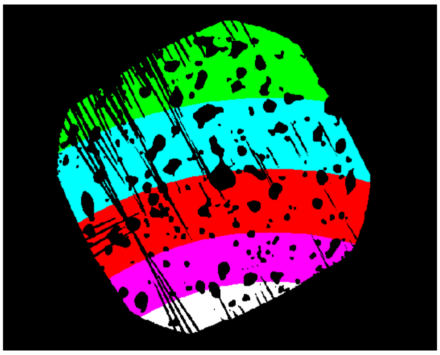

Figure 5.8: Left: X-ray image around X Comae obtained with EPIC-pn. Right: the area from which the spectra are extracted. The five colors correspond to the five fields used in the investigation of spatial variability of the spectrum. The center of the Coma cluster is in the south.

representative of the general background around the Coma cluster. The RASS R4 band map with the locations of these observations are displayed in Figure 5.7. One of them, HD111812 (ObsID 0008220201), was located on an unusually bright spot of the RASS maps and has been omitted from the analysis. The observations of the remaining fields and the distance from NGC 4874 are summarized in Table 5.6. We excised point sources (including X Comae of course) from the fields of X Comae and the four background pointings. We extracted a spectrum of each observation and subtracted the filter wheel closed data as an internal background spectrum. The image of X Comae field taken with EPIC-pn is shown in the left panel of Figure 5.8. The area from which the spectrum was extracted is shown in the right panel (the area including any colors was used).

5.3.2 Spectral analysis

We fitted the net vignetting corrected spectrum with a collisionally ionized thermal plasma model component (APEC in XSPEC) for the Coma hot gas, plus an APEC component for the Milky Way background, plus a power law component for the cosmic X-ray background. The free and fixed parameters of the models are given in Table 5.7. The energy range for the spectral fit was 0.4-7.0 keV, excluding the energies of strong detector lines (1.4–1.6 keV).

Our key finding is a clear detection of O VII and Ne IX lines from the X Comae field, as shown in Figure 5.9. In that figure we plot the ratio of the data to the smooth continuum fit described above. We tried to fit the excess of the spectrum by adding another lower temperature APEC model. However, the Ne IX line was not fitted, while O VII and O VIII structures were fitted. Next, we set the abundance of the warm thermal plasma zero and added three Gaussian lines to represent O VII, O VIII and Ne IX lines. The width of the three Gaussians were fixed to be 1 eV, which is far smaller than energy resolution of the detector. This model well fitted the data. The best fit values for the entire X Comae field are shown in Table 5.7.

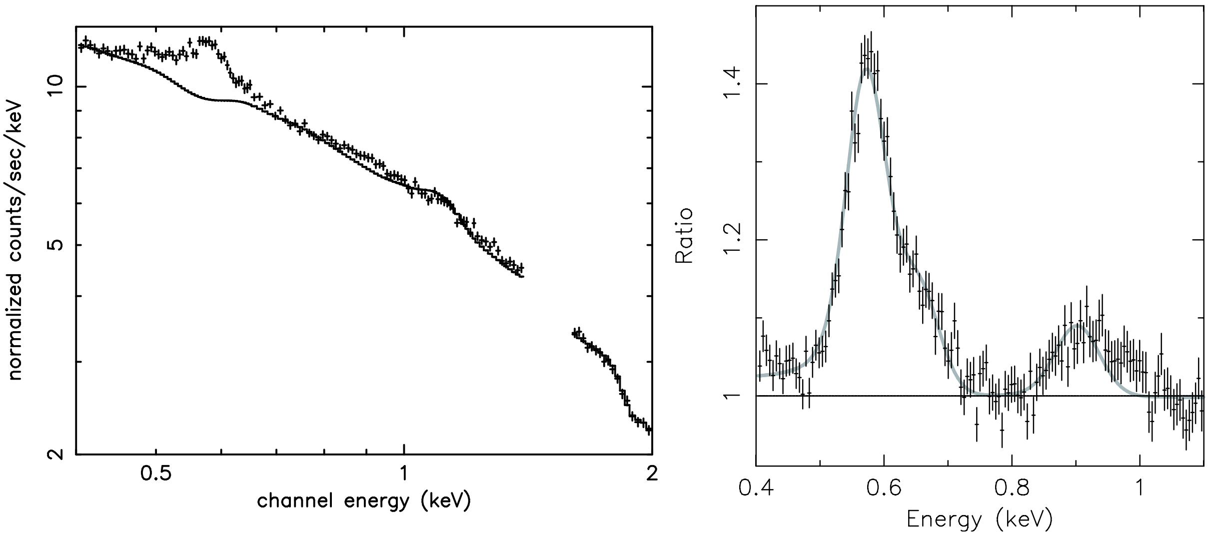

Figure 5.9: EPIC pn spectrum from the sum of the five regions around X Comae. Left: the spectrum with a model without metals. The discrepancy around 0.57 keV and 0.90 keV suggests the existence of O VII and Ne IX, respectively. Right: the ratio of the data to a smooth continuum (the model shown in the left panel. The smooth line is a fit of three narrow width (much less than the resolution) Gaussians to the residuals. The center of the lower-energy two Gaussians are fixed to O VII and O VIII at zero redshift, respectively, and that of the higher-energy Gaussian is fixed to Ne IX at the Coma redshift.

We also investigated the spatial variability of the O VII, O VIII and Ne IX lines. We divided the X Comae field into five concentric annuli approximately centered on the center of the cluster (see Figure 5.8 right), and fitted the spectra extracted from each region in the same way. The spectra of the four background fields were also fitted. Figure 5.10 shows the surface brightness of O VII , O VII and Ne IX vs. the radius from NGC4874. The five points with a small radius corresponds to the X Comae fields. The intensity of the Ne IX component increases toward the Coma cluster center. The intensity of this line in the background fields

Table 5.7: Fit results of EPIC-pn spectrum of diffuse gas around X Comae[a]

Component	Unit	Value
		Galactic absorption
$N_{\rm H}$	cm^{-2}	8.0×10^{19} (fixed)
		Coma hot ICM
kT	keV	$3.75^{+0.32}_{-0.50}$
Abundance	solar	0.47 ± 0.09
z		0.0231 (fixed)
Normalization[b]		$7.77^{+0.70}_{-0.85} \times 10^{-6}$
		Milky Way warm ISM
kT	keV	$0.174^{+0.002}_{-0.001}$
Abundance	solar	0, 1 (fixed)[c]
z		0 (fixed)
Normalization[b]		$5.5 \pm 0.2 \times 10^{-6}$
		Cosmic X-ray Background
Γ		1.40 (fixed)
Normalization[d]		$4.05^{+0.23}_{-0.18} \times 10^{-6}$
		O VII emission line
E	keV	0.574 (fixed)
I^e		$55.6^{+2.1}_{-1.8} \times 10^{-8}$
		O VIII emission line
E	keV	0.654 (fixed)
I^e		$15.4^{+1.3}_{-1.4} \times 10^{-8}$
		Ne IX emission line
E		0.901 (fixed)
I^e		$6.0 \pm 0.9 \times 10^{-8}$
Chi-squared		1305.15
Free parameters		9
Degrees of freedom		1272

[a]: Entire X Comae field (456.9 arcmin^2)

[b]: $\int n_{\rm e} n_{\rm H}\ dV/4\pi(D_{\rm A}(1+z))^2$ per solid angle in units of 10^{14} cm^{-5} arcmin^{-2}, where $n_{\rm e}$ is the electron density, $n_{\rm H}$ the hydrogen density, and $D_{\rm A}$ the angular size distance.

[c]: Abundance of He, C, Fe, and Ni is fixed to 1.0, while that of all other elements, including O and Ne, is fixed to 0.0

[d]: In units of photons keV^{-1} cm^{-2} s^{-1} arcmin^{-2} at 1 keV

[e]: In units of photons cm^{-2} s^{-1} arcmin^{-2}

Table 5.8: O and Ne lien intensity

Object	Distance from NGC 4874 (arcmin)	O VII I^a	O VIII I^a	NeIX I^a
X Comae	26.5	$55.6^{+2.1}_{-1.8}$	$15.4^{+1.3}_{-1.4}$	6.0 ± 0.9
X Comae 1	17.6	$61.7^{-12.8}_{-13.5}$	$12.9^{+9.2}_{-10.7}$	$11.5^{+6.4}_{-8.4}$
X Comae 2	20.6	$59.7^{-5.8}_{-5.5}$	$14.8^{+4.2}_{-3.9}$	$7.7^{+2.8}_{-2.7}$
X Comae 3	25.9	$54.7^{-3.7}_{-3.5}$	$15.0^{+2.4}_{-2.5}$	5.7 ± 1.7
X Comae 4	31.8	$53.5^{-2.8}_{-3.1}$	16.0 ± 2.1	$3.8^{+1.4}_{-1.3}$
X Comae 5	38.2	$53.2^{+4.1}_{-4.0}$	$15.6^{+2.7}_{-2.8}$	$5.2^{+1.7}_{-1.8}$
Coma 0	46.2	71.5 ± 5.1	28.1 ± 3.4	4.5 ± 1.8
1253+275	71.6	$44.9^{+6.5}_{-6.7}$	15.1 ± 4.5	1.1 (< 3.9)
3C 284	156.4	62.2 ± 4.0	26.4 ± 2.5	3.7 ± 1.2
β Comae	162.7	70.2 ± 5.5	17.5 ± 3.2	3.7 ± 1.6
Average bkgd	109.2	62.2 ± 9.8	21.8 ± 5.2	3.3 ± 1.2
Average bkgd [b]	130.2	59.1 ± 12.0	19.7 ± 5.5	2.8 ± 1.4
Wtd avg bkgd	109.2	63.6 ± 2.5	23.1 ± 1.6	3.5 ± 0.8
Wtd avg bkgd [b]	130.2	61.1 ± 2.9	21.8 ± 1.8	3.3 ± 0.9

[a]: Surface brightness in units of 10^{-8} photons cm^{-2} s^{-1} arcmin^{-2}

[b]: Except Coma 0 field, which may have a contribution from emission associated with the cluster.

is small compared to the regions projected near X Comae. The Coma intracluster medium is too hot to produce this line. We can also rule out a solar wind origin, as no variation with respect to the center of the Coma cluster in a single pointing is expected in that scenario. We thus conclude that we have detected Ne IX line emission from Coma cluster material that is cooler than most of the Coma intracluster medium.

The intensity of the O VII and O VIII Gaussian components did not vary in an obvious way as a function of position. The two oxygen lines show no enhancement at the position of the cluster: their intensity in the five X Comae sectors is the same or even lower than that in the background fields. We thus conclude that all of the oxygen emission comes from the Milky Way soft background and not from material in the Coma cluster.

The intensity of O VII and O VIII lines has a large scatter from one background field to another. The intensity in one of them (the 1253+275 field) is consistent with the soft X-ray background measured by McCammon et al. (2002) (they obtained 40.6 ± 10.9 and 13.5 ± 5.4 $\times 10^{-8}$ ph cm^{-2} s^{-1} arcmin^{-2}, for O VII and O VIII, respectively), while the intensity in the other fields are larger than their values. On the other hand, the scatter of the Ne IX intensity among the background fields is not as large and the average is consistent with the upper limit of McCammon et al. (2002). ($< 5.4 \times 10^{-8}$ ph cm^{-2} s^{-1} arcmin^{-2}, from their Figure 13).

Do we expect not to be able to detect Coma cluster oxygen emission given the strength of the cluster neon line? The O VII surface brightness is 1.67 times that of Ne IX, for a temperature of 4×10^6 K and a Ne/O number density ratio of 0.14 or more (see § 5.4.1 for a justification of these values). This expected O VII line intensity in the entire X Comae

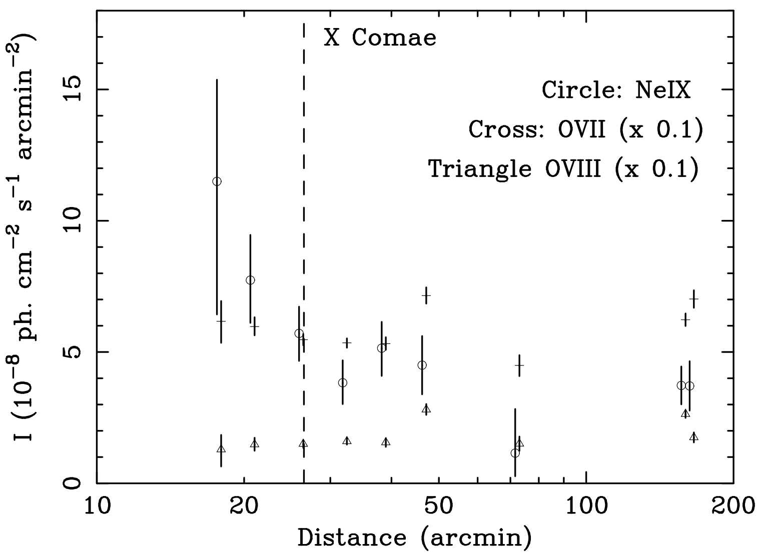

Figure 5.10: Surface brightness of O VII and O VIII (crosses (+) and triangles ($\triangle$), divided by ten) and Ne IX[(circles ($\circ$)) versus distance from NGC 4874, which we take as the center of the Coma cluster.

field is approximately the dispersion of the other nine measurements (10.0 versus 8.0 $\times 10^{-8}$ ph cm^{-2} s^{-1} arcmin^{-2}, respectively). Thus the different behavior of the neon and oxygen emission lines is probably due to the much lower galactic neon background intensity that allows the Coma neon emission to be detected. The higher galactic oxygen background intensity masks the Coma oxygen emission in the X Comae fields.

In the next section we will need the net Ne IX intensity at the position of X Comae. Of course this measurement requires an extrapolation to that position since the glare from the AGN prevents measurement of emission from the Coma cluster gas. We give in Table 5.8 the numerical and error-weighted average of all four background fields and the three fields excluding Coma 0. The numerical average is more appropriate if there are real variations from field to field. Excluding Coma 0 is appropriate if it has a higher intensity. Since none of the four averages are statistically distinguishable, we take for the Ne IX background the weighted average of all background fields since it has the lowest error. Similarly we take for the gross intensity the value from the entire X Comae field, since it is statistically indistinguishable from the sector closest to X Comae but has a lower error. The net intensity is thus $2.5 \pm 1.2 \times 10^{-8}$ ph cm^{-2} s^{-1} arcmin^{-2} (90% confidence errors or 3.4σ detection). The emission intensity corresponds to $Z\ EM = 4.1 \pm 2.0 \times 10^{15}$ cm^{-5} $Z_{\rm ISM}$, where EM is the emission measure defined as Eq.2.12

5.3.3 Possible systematic uncertainties

The intensity of Ne IX line is only 9% of the continuum level, as is seen in Figure 5.9. Such a low intensity may mean that its measurement is subject to systematic errors.The largest systematic uncertainty in determining the intensity of emission lines is that of continuum shape. The detector response is much better calibrated; the uncertainty of absolute effective area is $\sim 4\%$. Note that we didn't use the energy of strong detector lines in order to prevent increasing systematic errors.

Here we concentrate on the uncertainty of Ne IX emission, the most important parameter of this analysis. We found that the Ne IX intensity is affected by the abundance of the cluster hot gas, since there is Fe L structure around 1 keV. Although the abundance of cluster hot gas was statistically determined with 15% uncertainty, if we adopted 0.1 $Z_\odot$ or 0.5 $Z_\odot$, the Ne IX intensity would change by $\sim \pm 20\%$. We adopted $\pm 20\%$ as the upper limit of systematic uncertainty. This is comparable to the statistical error of the Ne IX intensity of the background field.

We summarize this section by noting that the weak Ne IX line intensities from the Milky Way interstellar medium combined with a very deep exposure allowed us to achieve a robust detection of Ne IX line emission from the Coma gas projected near X Comae.

5.4 Properties of the Warm-Hot Gas

We have detected absorption features in the RGS spectra of X Comae at the redshift of the Coma cluster with a combined confidence of 99.7% (equivalent to 3.0σ of a Gaussian distribution) and line emission features in the EPIC pn spectra of diffuse gas at the position of X Comae at the 3.4σ confidence level. Although the significance of either one is not very high, the fact that we observed *both* absorption and emission from Ne IX at the Coma cluster redshift or position is additional support for the detection of this ion. In this section we give the properties of the warm-hot gas that can be deduced from our observations under the assumption that the absorbing and emitting materials are the same and that material is uniformly distributed in a single phase in collisional ionization equilibrium. Although these assumptions have the virtue that they are simple and are consistent with the observations, it is entirely possible, even likely, that the actual situation is more complicated. In this case the properties we derive will be typical of the dominant phase of the material.

5.4.1 Temperature and Ne/O number density ratio

We can constrain the temperature of a plasma in ionization equilibrium from the ratios of absorption EWs between different ionization states of the same species. On the other hand, we can constrain the number density (or abundance) ratio of different elements from the ratio of absorption EWs between lines of different species.

First, we investigate the allowed temperature and abundance for the boxcar-fitting case. Figure 5.11 plots the ratio of the theoretically expected EWs of Ne X, O VII or O VIII to Ne IX divided by the observed upper limits to that ratio. That is, it plots a ratio of ratios. The expected values were calculated using the ionization fractions of a plasma under collisional ionization equilibrium given in Figures 2 and 3 of Chen et al. (2003). In this calculation we assumed $EW \propto N_{\rm ion} f_{\rm os}$, i.e. no saturation. The dotted line shows Ne X, while the dashed lines show the larger value for O VII or O VIII. The allowed temperature is the range for which both the Ne IX and O curves are below 1. The upper limit of Ne X/Ne IX ratio gives a robust upper limit of the temperature, $T < 5.8 \times 10^6$ K.

The theoretical O VII or O VIII to Ne IX EW ratios depend on the number density ratio of Ne/O, while Ne/O ratio is not well known even for solar or interstellar values as described in §2.4. The widely-used solar Ne/O number density ratio is 0.14 (Anders & Grevesse, 1989,

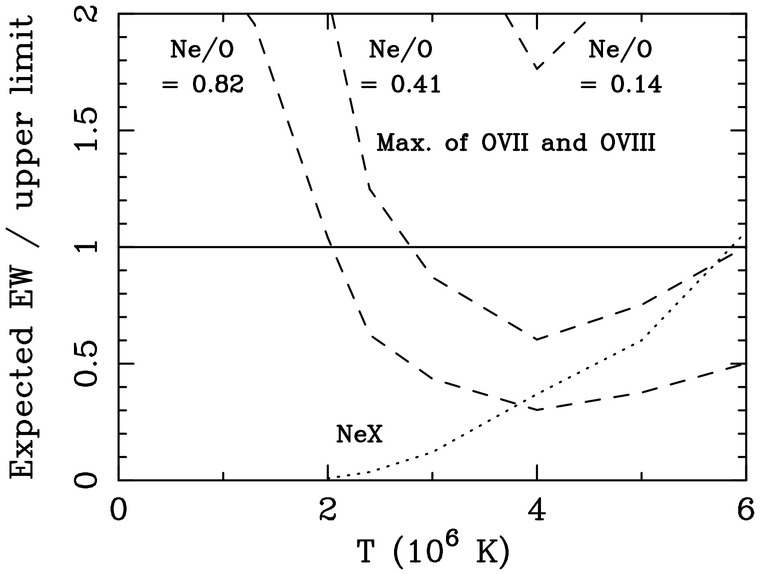

Figure 5.11: The ratio of the theoretically expected EWs of Ne X, O VII or O VIII to Ne IX divided by the observed upper limits to that ratio. The dotted line shows NeX, while the dashed lines show the larger value for OVII or OVIII. Since the theoretical OVII or OVIII to NeIX EW ratios depend on the number density ratio of Ne/O, we indicate three cases: 0.14 as the canonical value 0.41 as the highest one found from literature, and 0.82 as the extremely high Ne/O case. The allowed temperature is the range in which both NeIX and O curves are below 1. There is no allowed temperature range for Ne/O = 0.14, while it is 2.0×10^6 K $< T < 5.8 \times 10^6$ K for the extremely high Ne/O case. The ionization fraction given in Table 2 and 3 of Chen et al. (2003) for collisional ionization case was assumed.

$Z_\odot$ in this thesis). A higher Ne/O ratio, 0.41, was suggested by X-ray spectroscopy of mostly giant stars and multiple systems (Drake & Testa, 2005, $Z_{\rm ISM}$ in this thesis).

Since our boxcar-fitting cannot determine the Ne/O ratio, we indicate three cases in Figure 5.11: 0.14 as the canonical value, 0.41 as the highest one found in the literature, and 0.82 as an extremely high Ne/O case. We found that Ne/O > 0.25 (2σ) is necessary in order to reproduce the boxcar-fit results with an assumption of single temperature plasma; for example, there is no intersection of O curve and 1 for Ne/O = 0.14, i.e., $Z_\odot$. Thus, the canonical Ne/O ratio ($Z_\odot$) is rejected in this analysis. On the other hand, if Ne/O was larger than 0.25, there was allowed temperature range. Even if adopting an extremely high Ne/O ratio, Ne/O = 0.82, the temperature range can be constrained to be $T > 2.0 \times 10^6$ K. Combining this constraint with that from Ne X/Ne IX ratio, we obtained a conservative temperature range, 2.0×10^6 K $< T < 5.8 \times 10^6$ K.

We next used the EWs determined with the ratio method (§ 5.2.2). This method is independent of the intrinsic shape of the absorption. The left panel of Figure 5.12 shows the theoretical equivalent width ratios of O VII/O VIII and Ne X/Ne IX as a function of temperature T again based on Figures 2 and 3 of Chen et al. (2003) in the case of collisional ionization equilibrium. Note that here we use the O VII/O VIII ratio because O VIII was also detected at more than 90% confidence with the ratio method. We show the observed 2σ upper limits obtained in § 5.2.2 with horizontal lines in the left panel of Figure 5.12.

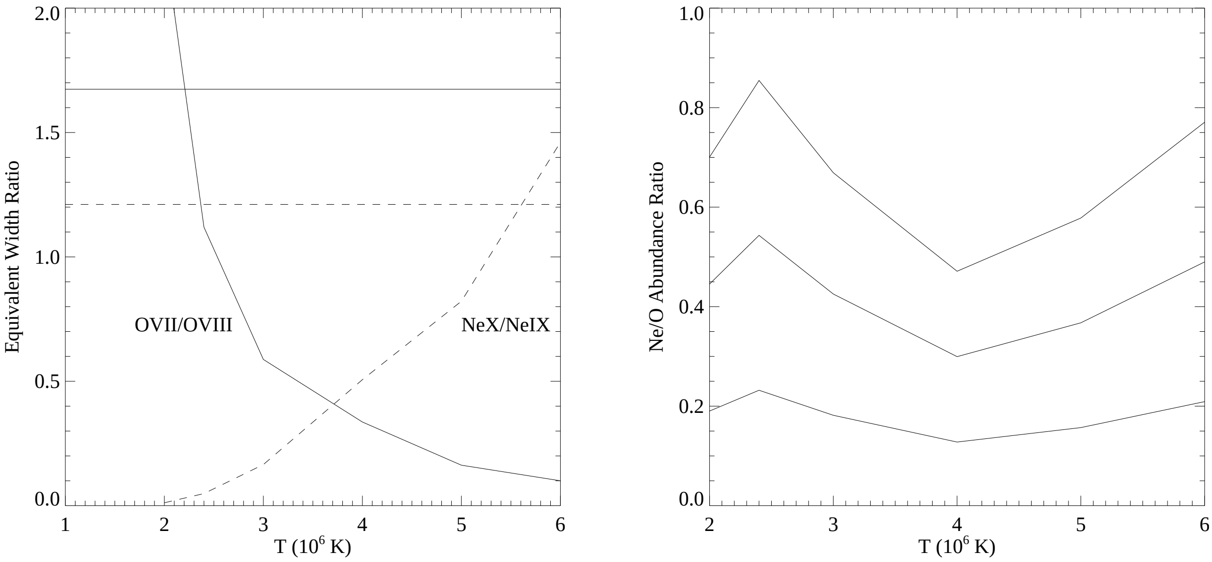

Figure 5.12: (left) Equivalent width ratio as a function of temperature T, based on Figure 2 and 3 of Chen et al. (2003) in the collisional ionization equilibrium case. Solid and dashed curves correspond to OVII/OVIII and NeX/NeIX, respectively. The horizontal lines represent the upper limits determined by this work. The allowed temperature is that for which the curved lines are below the horizontal upper limit lines of the same style, i.e., $T > 2.2 \times 10^6$ K for OVII/OVIII and $T < 5.7 \times 10^6$ K for NeX/NeIX. (right) Ne/O number density ratio as a function of temperature T. The three curves correspond to the best-fit values and $\pm 1\sigma$ errors, respectively, obtained from the observed Ne IX/O VIII ratio.

The allowed temperature range is that for which the curved lines are below the horizontal upper limits of that ratio, i.e., $T > 2.2 \times 10^6$ K for O VII/O VIII and $T < 5.7 \times 10^6$ K for Ne IX/Ne X. Combining these two constraints, we restricted the temperature of the plasma to be 2.2×10^6 K $< T < 5.7 \times 10^6$ K at the 2σ confidence level.

From the Ne IX/O VIII ratio, we can investigate the allowed Ne/O number density ratio as a function of temperature T. This is shown in the right panel of Figure 5.12. The $\pm 1\sigma$ error range is also shown. The allowed Ne/O ratio is not very sensitive to temperature; it is roughly 0.3 ± 0.15 to 0.5 ± 0.3 within the allowed temperature range found above. Although our best-fit Ne/O ratio suggests a Ne overabundance ($\sim Z_{\rm ISM}$), all of the above including the canonical value of 0.14 ($Z_{\odot}$) is within our $\sim 1\sigma$ confidence limit. Note that both temperature range and Ne/O ratio are consistent in the two estimates (boxcar fitting and ratio values).

5.4.2 Density, line of sight length and metallicity

We can constrain the average hydrogen density $n_{\rm H}$ of the warm-hot gas and its path length L along the line of sight by combining absorption and emission observations of the same ion, Ne IX in our case. The column density of an ion is

$$N_{\rm ion} = f_{\rm ion} Z n_{\rm H} L \tag{5.5}$$

where Z and $f_{\rm ion}$ are the abundance and the ionization fraction of a metal, respectively. Eq. (5.5) gives $N_{\rm ion}$ as a function of the observed EW. The surface brightness of an emission

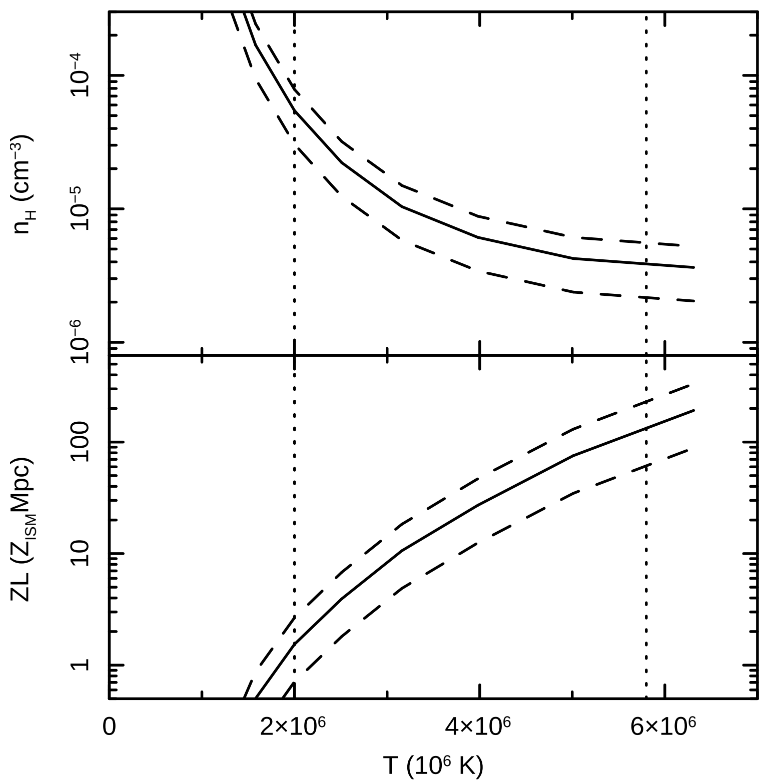

Figure 5.13: Derived $n_{\rm H}$ (upper) and ZL (lower) as a function of T. Solid and dashed curves represents best-fit values and 1σ confidence regions, respectively. Vertical dotted lines indicate allowed temperature range, 2.0×10^6 K $< T < 5.8 \times 10^6$ K (see Figure 5.12).

line I can be written as in proportion to the emission measure $\int n_{\rm e}^2 dV$, and thus $n_{\rm e}^2 SL$ assuming uniform distribution, as

$$I = \frac{C}{(1+z)^3} Z n_{\rm H}^2 L \tag{5.6}$$

where C is a coefficient depending on the temperature T but independent of the abundance. (c.f. Equation (2.11)). Here the exponent of $(1+z)$ is three instead of four because we measure surface brightness in photons, not ergs. Solving these two equations simultaneously gives

$$n_{\rm H} = \frac{f_{\rm ion}(1+z)^3}{C} \frac{I}{N_{\rm ion}} \tag{5.7}$$

and

$$ZL = \frac{C}{f_{\rm ion}^2 (1+z)^3} \frac{N_{\rm ion}^2}{I} \tag{5.8}$$

. Note that $n_{\rm H}$ can be determined without assumption of Z, while L depends on Z.

The coefficient C is

$$C = \frac{1}{4\pi} \left(\frac{n_{\rm e}}{n_{\rm H}} \right)^2 \frac{1}{Z(M)} \sum_j \frac{P'_j}{E_j}. \tag{5.9}$$

Here $n_{\rm e}/n_{\rm H} = 1.17$, $Z(M)$ is the abundance of the element assumed by Mewe et al. (1985) (8.32×10^{-5} for neon), P' is tabulated in Table IV of Mewe et al. (1985), E is the energy of the line and the sum is over all lines not resolved with CCD energy resolution. For the Ne IX emission C comes from six lines: Ne IX resonance line (13.44 Å), three satellite lines of Ne VIII (13.44 Å, 13.46 Å and 13.55 Å), Ne IX intercombination line (13.55 Å) and Ne IX forbidden line (13.70 Å).

We derive the parameters of the material producing the Ne IX absorption and emission as a function of temperature from its column density and intensity at the position of X Comae found at the ends of Sections 5.2.3 and 5.3, respectively. The derived values of $n_{\rm H}$ and ZL depend strongly on the temperature. We show in Figure 5.13 the values as a function of temperature, where solid and dashed curves represent best-fit values and 1σ confidence regions, respectively. Vertical dotted lines indicate the allowed temperature range, 2.0×10^6 K $< T < 5.8 \times 10^6$ K (see Figure 5.11). We constrained $n_{\rm H}$ to be 2×10^{-6} cm^{-3} $<$ $n_{\rm H}$ $<$ 8×10^{-5} cm^{-3} and ZL to be 0.7 $Z_{\rm ISM}$Mpc $< ZL <$ 300 $Z_{\rm ISM}$Mpc. These limits are at approximately the 3σ confidence level since they sum the 2σ limit on temperature and the 1σ limit on $n_{\rm H}$ and ZL (i.e., do not sum the errors in quadrature). The derived hydrogen density corresponds to $10 < \delta < 400$. Although the constraint we obtained on ZL is not tight, we note that the lower limit on L is > 0.7 Mpc $(Z/Z_{\rm ISM})^{-1}$. Assuming typical abundance of the ICM, $Z \lesssim 0.3\ Z_{\rm ISM}$, even this lower limit is comparable or larger than the cluster virial radius, $r_{\rm vir} = 2.3 h_{70}$ Mpc (Girardi et al., 1998). As the temperature goes high, the ionization fraction of Ne IX becomes smaller from 1.0 (2×10^6 K) to 0.1 (6×10^6 K). If assuming a realistic value $f_{\rm ion} = 0.75$, which corresponds to a temperature of 3.2×10^6 K

$$n_{\rm H} = 1.0 \times 10^{-5}\ {\rm cm}^{-3} \left(\frac{I}{2.5 \times 10^{-8}}\right) \left(\frac{N_{\rm NeIX}}{4.7 \times 10^{16}\ {\rm cm}^{-2}}\right)^{-1}, \tag{5.10}$$

$$(Z/Z_{\rm ISM})L = 11\ {\rm Mpc} \left(\frac{I}{2.5 \times 10^{-8}}\right)^{-1} \left(\frac{N_{\rm NeIX}}{4.7 \times 10^{16}\ {\rm cm}^{-2}}\right)^{2} \tag{5.11}$$

are given.

The distribution of galaxies in the Coma cluster is asymmetric in the line of sight direction (see Figure 3.2); the distribution looks like a sum of two Gaussians. The difference of the redshift of two centers are ~ 0.003. This difference of the velocity corresponds to ~ 15 Mpc, if assuming that the difference represents the position of two substructures, i.e., the Hubble flow origin. This distance is also consistent with L estimated above. Since the size of the Coma cluster is $\sim$ 3 Mpc, the two peaks of the galaxy distribution suggests a filament elongated in the line of sight direction five times larger than its transverse direction.

5.4.3 The mass of the WHIM

The mass of the material can be estimated by assuming its geometry. The object appears to be elongated along the line of sight, since L is much larger than any characteristic size of the Coma cluster across the line of sight. Therefore, we assumed a cylindrical distribution of the WHIM of radius $R_{\rm WHIM}$ ($< L$) and length L. The baryon mass is then

$$M_{\rm WHIM} = \frac{N_{\rm NeIX}}{f_{\rm ion} Z} \frac{m_{\rm p}}{X} \pi R_{\rm WHIM}^2, \tag{5.12}$$

or

$$M_{\rm WHIM} = 6.0 \times 10^{13}\ M_\odot \left(\frac{R_{\rm WHIM}}{1\ \rm Mpc}\right)^2 \left(\frac{N_{\rm NeIX}}{4.7 \times 10^{16}\ \rm cm^{-2}}\right) \left(\frac{f_{\rm ion\ NeIX}}{0.75}\right)^{-1} \left(\frac{Z}{0.2\ Z_{\rm ISM}}\right)^{-1}. \tag{5.13}$$

$M_{\rm WHIM}$ depends strongly on the most uncertain parameter $R_{\rm WHIM}$. Here we quote two values of $R_{\rm WHIM}$. The lower limit would be the distance of X Comae from NGC 4874, $r_{\rm QSO}$, i.e., $R_{\rm WHIM} = r_{\rm QSO} = 0.74$ Mpc, which corresponds to $M_{\rm WHIM} = 3.3 \times 10^{13}\ M_\odot$. If we adopt $R_{\rm WHIM} = r_{\rm vir} = 2.3 h_{70}^{-1}$ Mpc (Girardi et al., 1998), $M_{\rm WHIM}$ is calculated to be $M_{\rm WHIM} = 3.2 \times 10^{14}\ M_\odot$. The total mass (baryons and dark matter) $M_{\rm total}$ and the hot gas mass of the cluster $M_{\rm hot}$ are $M_{\rm total} = 1.3 \times 10^{15} h_{70}^{-1}\ M_\odot$ and $M_{\rm hot} = 2.2 \times 10^{14} h_{70}^{-5/2}\ M_\odot$, respectively (Briel et al., 1992). They summed up the mass within $3.6 h_{70}^{-1}$ Mpc from the cluster center (NGC 4874). $M_{\rm WHIM}$ and its ratio to $M_{\rm total}$ and $M_{\rm hot}$ are summarized in Table 5.9 for the two cases: $R_{\rm WHIM} = r_{\rm QSO}$ and $R_{\rm WHIM} = r_{\rm vir}$. Note that the dependence of emission intensity on the distance from the Coma center (see Figure 5.10) suggests $R_{\rm WHIM} \sim 50' = 1.4$ Mpc.

Table 5.9: $M_{\rm WHIM}$ and its ratio to the cluster mass

$R_{\rm WHIM}$	$M_{\rm WHIM}$	$M_{\rm WHIM}/M_{\rm hot}$	$M_{\rm WHIM}/M_{\rm total}$
$r_{\rm QSO} = 0.74$ Mpc	$3.3 \times 10^{13}\ M_\odot$	14%	2.7%
$r_{\rm vir} = 2.3$ Mpc	$2.2 \times 10^{14}\ M_\odot$	140%	25%

5.5 Discussion of possible systematic uncertainties

5.5.1 Can the Ne IX emission come from material within the cluster virial radius?

We investigate the suggestion by Cheng et al. (2005) that gas associated with merging subgroups inside the cluster virial region, which preserves its identity for a while before being destroyed by the hot intracluster medium, is responsible for the cluster soft excess. In particular, we determine whether this material can produce the Ne IX emission we observe. We disregard the constraints from the absorption measurements here. Rather we assume that the temperature of this material is 2×10^6 K, the peak of the Ne IX ion fraction, and that the material is in pressure equilibrium with the ICM. Neither of these assumptions is very constraining. Changing the temperature to 4×10^6 K, the midpoint of the allowed range found previously, changes the results calculated below by less than a factor of two. The second assumption yields a density of warm-hot material similar to the densest regions of groups, which we could have assumed at the outset since that is the suggestion we are investigating.

First we need the properties of the hot ICM. The emission-weighted temperature at the position of X Comae is 7.4 keV from the temperature map of Honda et al. (1996). The emission measure-weighted hydrogen density at the position of X Comae is $2 \times 10^{-4} h_{70}^{1/2}$ cm^{-3} (Briel et al., 1992). Next we need the properties of the warm-hot material. A temperature of 0.172 keV and pressure equilibrium with the ICM yields a hydrogen density of $8.6 \times 10^{-3} h_{70}^{1/2}$

cm^{-3}, or $\delta \sim 3.4 \times 10^4$, and entropy $\sim$ 4 keV $h_{70}^{-1/3}$ cm^2. The latter two values place the warm-hot material on the extreme high density tail of the phase plot in Figure 4 of Cheng et al. (2005). Equation (8) with C(2×10^6 K) $= 1.19 \times 10^{-13}$ photons cm^3 s^{-1} sr^{-1}, the above hydrogen density and the observed Ne IX surface brightness imply the path length through the material L is $\sim$ 100 pc. The sound crossing time across L is $\sim 5 \times 10^5$ years, during which the material travels $\sim$ 600 pc moving at σ_{gal} c. Thus pressure equilibrium is a good assumption because the ICM pressure hardly changes over such a small distance.

How long can this warm-hot material survive? We assume its size across the line of sight is also L, that is the warm-hot material is tiny blobs of diameter $\sim$ 100 pc. Following Cowie & McKee (1977), the classical heat conduction across the blob-cluster interface is saturated. The saturated evaporation time is $\sim 1 \times 10^4$ years, from their equation (64). Any blobs that might exist are very quickly destroyed. Further they are not replenished since the time for group gas at a temperature of 2 keV and the above density to cool to a temperature at which there is a significant population of Ne IX is $\sim 5 \times 10^{10}$ years.

Even after the blobs evaporate it takes some additional time for the Ne ion distribution to equilibrate to that appropriate to the new temperature in which the Ne finds itself. The longest lived ion capable of emitting the Ne IX resonace line we detect is Ne X, which it does by electron capture to an excited level followed by radiative deexcitation. The ionization time $\tau_{\rm ion}$ to convert Ne X to Ne XI is mostly determined by the collisional ionization efficiency $S_{\rm NeX}$; i.e., $\tau_{\rm ion} \sim 1/n_{\rm e} S_{\rm NeX}$. The recombination rate is negligibly small and the ionization time to convert Ne IX to Ne X is smaller than that for Ne X to Ne XI in our case. The empirical formula for $S_{\rm NeX}$ for coronal plasma is given in McWhirter (1965, equation 40 of Chapter 5) as

$$S_{\rm NeX} = 1.10 \times 10^{-5} \frac{(kT_{\rm e}/\chi)^{1/2}}{\chi^{3/2}\,(6 + kT_{\rm e}/\chi)}\ \exp\left(-\frac{\chi}{kT_{\rm e}}\right)\ {\rm cm^{-3}\ s^{-1}}, \tag{5.14}$$

where $T_{\rm e}$ and χ are the electron temperature and the ionization energy in eV, respectively. Substituting the properties of the hot gas, $T_{\rm e}$ = 7400 eV, χ = 1360 eV, and $n_{\rm e} = 2.3 \times 10^{-4}$ h$_{70}^{1/2}$cm^{-3}, we find $\tau_{\rm ion} = 3.7 \times 10^6$ years. The evaporation and the equilibration times are much smaller than the cluster crossing time, the characteristic scale of the situation. Thus we conclude that, under reasonable assumptions, material within the cluster virial radius is not capable of producing the observed Ne IX emission unless we are viewing the Coma cluster at a very special epoch.

5.5.2 Photo-ionization due to the cluster emission

In § 5.4.2, we estimated the allowed temperature range in the collisional ionization case and photo- and collisional ionization case. In the latter case, cosmic X-ray and UV backgrounds are assumed to be the photon source. However, cluster emission will dominate sufficiently near the cluster. This "proximity effect" is parameterized with an ionization parameter defined as the ratio between the ionizing photon and gas densities or $U \equiv \phi/cn_{\rm H}$, where ϕ is the photon flux and c is the speed of light.

We estimated U from the Coma cluster emission as follows. The spectrum of the cluster (hot) emission is roughly represented as a power-law with $\Gamma = 1.3$ (Briel et al., 1992), and the spectrum of the entire cluster is then

$$N(E) = 8.54 \times 10^{-2} \left(\frac{E}{1\ \mathrm{keV}}\right)^{-1.3} \ \text{photons cm}^{-2}\ \mathrm{s}^{-1}\ \mathrm{keV}^{-1}. \tag{5.15}$$

Integrating this spectrum between 20 eV and 10 keV, we find

$$\phi = 0.78 \ \text{photons cm}^{-2}\ \mathrm{s}^{-1} \tag{5.16}$$

at Earth. Assuming the Coma cluster is a point source, ϕ and U at distance D from the cluster center are

$$\phi = 875 \left(\frac{D}{3\ \mathrm{Mpc}}\right)^{-2} \ \text{photons cm}^{-2}\ \mathrm{s}^{-1},\ \text{and} \tag{5.17}$$

$$U = 0.18 \left(\frac{D}{3\ \mathrm{Mpc}}\right)^{-2} \ \delta^{-1}. \tag{5.18}$$

In comparison, the ionization parameter due to the X-ray and UV background radiation is $U = 0.15\ \delta^{-1}$ (Nicastro et al., 2005c). Thus, for $D \gtrsim 3$ Mpc, the background radiation dominates the cluster emission. On the other hand, for $D \lesssim 3$ Mpc, n_{H} of the cluster hot gas is larger than $10^{-5}\mathrm{cm}^{-3}$ (Briel et al., 1992). Hence, the material producing the Ne IX emission and absorption would be heated to the cluster temperature. We conclude that assuming that the UV and X-ray backgrounds are the source of photo-ionization is reasonable for a calculation of the properties of the warm-hot material around Coma.

5.5.3 Non-uniform distribution

In § 5.4.2, we estimated the hydrogen density n_{H} and line-of-sight length L assuming a uniform distribution. Here we investigate how the values change with different distributions.

If the distribution is "patchy" with the volume filling factor of f_{vol}, the column density of the ion N_{ion} and the surface brightness I are written as

$$N_{\mathrm{ion}} \propto n_{\mathrm{H}} f_{\mathrm{vol}} L, \tag{5.19}$$

$$I \propto n_{\mathrm{H}}^2 f_{\mathrm{vol}} L, \tag{5.20}$$

which reduce to Equations (5.5) and (5.6), respectively, if we rewrite them with $L' = f_{\mathrm{vol}} L$. This means that n_{H} is not affected, while L becomes $1/f_{\mathrm{vol}}$ compared to the values of § 5.4.2.

Next, we consider the case with n_{H} gradient in the line of sight direction, which is represented in Figure 5.14. In this case, n_{H} has the highest value n_0 at the center and decreases linearly. The line of sight length L is defined as shown in Figure 5.14. Then, N_{ion} and I are given by

$$N_{\mathrm{ion}} \propto \int n_{\mathrm{H}} dL = \frac{1}{2} n_0 L = n_{\mathrm{mean}} L, \tag{5.21}$$

$$I \propto \int n_{\mathrm{H}}^2 dL = \frac{1}{3} n_0^2 L = \frac{4}{3} n_{\mathrm{mean}}^2 L. \tag{5.22}$$

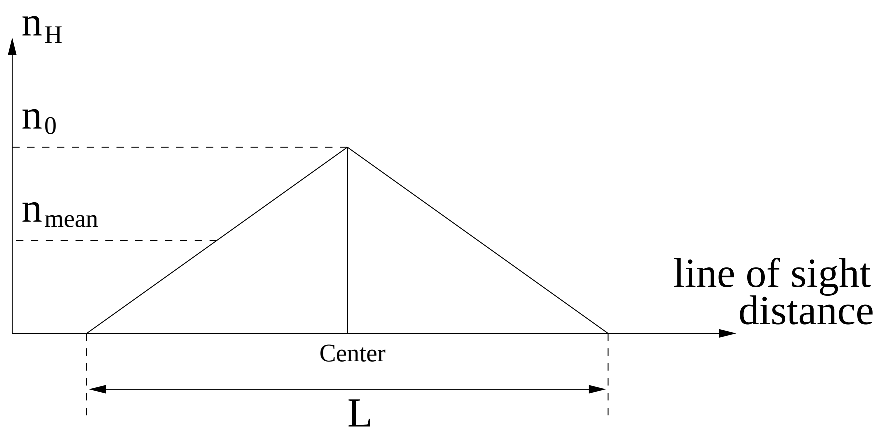

Figure 5.14: The assumed gradient of n_{H}.

These equations correspond to Equations (5.5) and (5.6) using n_{mean} and $3I/4$, instead of n_{H} and I, respectively. In this case, n_{mean} is 3/4 times n_{H} derived in § 5.4.2, while L is 4/3 times that derived in the section. The mass M_{WHIM} is calculated as

$$M_{\mathrm{WHIM}} = \int 2\pi R dR \int dL \; n_{\mathrm{H}}(R, L). \tag{5.23}$$

Therefore, M_{WHIM} is not changed if n_{H} is uniform in the direction perpendicular to sight line, while it becomes 1/3 if assuming the similar linear gradient of n_{H} in the transverse direction.

As long as we are looking the warm-hot gas forming a filament-like structure, the latter case (with n_{H} gradient) is more likely than the former (patchy) case. Note that smaller n_{mean} and larger L than those of § 5.4.2 are always derived with any non-uniformity.

Chapter 6

The Virgo cluster vicinity

6.1 Observation

The first analysis of this work has already been published as Fujimoto et al. (2004), of which I am one of the authors. Here I expand our previous work to further constrain the geometry and the mass of the WHIM.

We observed LBQS 1228+1116 with XMM-Newton, from 2003 July 13 to July 14. The observation ID is 0145800101. The instrument mode, filter, and the net exposure time are summarized in Table 6.1. Note that, although 100 ks was scheduled, the net observation time was only $\sim$ 50 ks due to background flares. LBQS 1228+1116 is located at 83.3' or $0.45 h_{70}^{-1}$ Mpc south of M87 (see Figure 3.4). Its redshift is $z = 0.237$ (Hewett et al., 1995), while the redshift of M87 is 0.00436. Galactic neutral hydrogen column density in this direction is measured to be $N_{\rm H} = 9.3 \times 10^{19}$ cm^{-2} (Dickey & Lockman, 1990).

6.2 Absorption in the LBQS 1228+1116 spectra

6.2.1 Data reduction

We reprocessed and cleaned the data in the similar way to § 5.2.1 using the XMM-Newton Science Analysis System (SAS), version 5.4.1, with standard parameters. We accumulated the signal photons only when the count rates in source-free region of CCD 9 were less than 0.15 cps for both RGS1 and 2. Since the observation data file (ODF) was divided into two files, we merged the two data sets. The net exposure time was 8.8 ks for the first file and 45.0 ks for the second. The background spectra were produced using the same data sets. All of the spectra were binned by a factor of four (0.042 Å bin around the O VIII Kα line, 18

Table 6.1: Observation mode and net exposure time.

Instrument	Mode	Filter	Net exposure
RGS	Spectrum+Q	—	53.8 ks
EPIC pn	Full frame	Thin1	44.9 ks
EPIC MOS	Full frame	Medium	56.9 ks

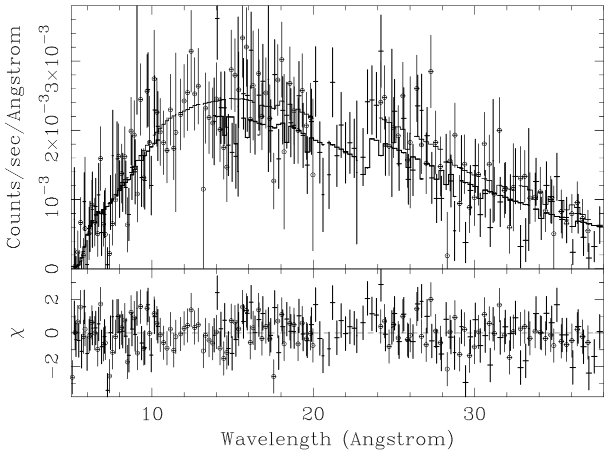

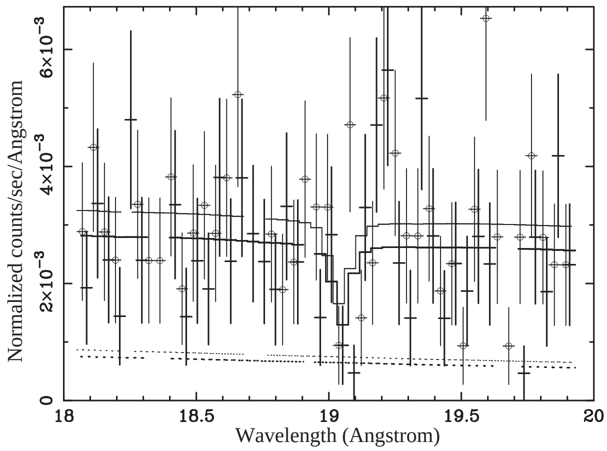

Figure 6.1: Spectra of LBQS 1228+1116 obtained with RGS1 and 2. Left: spectra of whole wavelength range after subtraction of background spectra (for illustrative purpose). Right: those around the O VIII Kα line. The cross and circle symbols represent the data points of RGS1 and 2, respectively. The thick and thin solid histograms show the best-fit models for RGS1 and 2. The backgrounds were not subtracted, but were instead simultaneously fitted with a constant model. The background levels are shown with dotted curves. For illustrative purposes, channels with flickering pixels were masked.

Å). Since the number of photons, especially near the absorption line, is small, we used the C-statistic (maximum-likelihood) method for model fitting of RGS spectra.

6.2.2 Fitting of the RGS spectra

The left panel of Figure 6.1 shows the spectra of LBQS 1228+1116 obtained with the RGS1 and 2. We searched the spectra of LBQS 1228+1116 for O VII, O VIII Ne IX and Ne X, and found a sign of absorption line of O VIII. The right panel of Figure 6.1 shows the spectra between 18 Å and 20 Å. There is an absorption-line feature at around 19.1 Å in both RGS1 and 2. We fitted the spectra with a power law and a negative Gaussian, multiplied by the Galactic absorption ($N_{\rm H} = 2.15 \times 10^{20}$ cm^{-2}), using XSPEC version 11.2. Background spectra were simultaneously fitted with a constant model. The results are summarized in Table 6.2; the best-fit model is shown in Figure 6.1. The line shape was consistent with a narrow line, with a 90% upper limit on a width of $\sigma < 5.1$ eV. Hence, the line width was fixed at 0.1 eV, which is small compared with the detector resolution ($\Delta\lambda \sim 0.06$–0.07 Å or $\Delta E \sim 2$ eV FWHM). When we calculated the errors of the absorption-line parameters, we also fixed the photon index of the power-law component. The observed line center energy and equivalent width were $650.9^{+0.8}_{-1.9}$ eV and $2.8^{+1.3}_{-2.0}$ eV, respectively. If we assume that this is an O VIII absorption line, the energy shift from the rest frame is $2.7^{+0.8}_{-1.9}$ eV, which corresponds to $cz = 1253^{+881}_{-369}$ km s^{-1}. This is consistent with that of M87 ($cz = 1307$ km s^{-1}). Note that the systematic error in the absolute energy scale of the RGS is 8 mÅ (rms) or 0.3 eV at 650 eV (den Herder et al., 2001), which is much smaller than the statistical errors.

Table 6.2: Best-fit parameters of the O VIII absorption line.

Galactic absorption	
$N_{\rm H}$	2.15×10^{20} cm^{-2} (fixed)
Absorption line	
Energy	$650.9^{+0.8}_{-1.9}$ eV
Width (σ)[a]	< 5.1 eV (90%)
Normalization	$(3.9^{+2.0}_{-2.8}) \times 10^{-6}$ photons cm^{-2} s^{-1}
Power law	
Index	3.2
Normalization[b]	$(3.57 \pm 0.35) \times 10^{-4}$
Background power-law	
Index	0 (fixed)
Normalization[b]	3.81×10^{-4}
C-statistic	177.02
d.o.f	167

[a] For all fits except for the determination of the statistical error for this parameter, it was fixed at 0.1 eV.
[b] In units of photons keV^{-1} cm^{-2} s^{-1} at 1 keV.

6.2.3 Evaluation of the detection significance

We evaluated the statistical significance of the absorption line in the following way. The best-fit model without an absorption line gives a C-statistic of 181.76. When we include an absorption line, but fix the center and the width to the energy of the O VIII Kα resonant line with $cz = 1307$ km s^{-1} and $\sigma = 0.1$ eV, respectively, we obtain the best-fit C-statistic of 177.43. Thus, the improvement, ΔC, is 4.33. The value of ΔC approximately follows the χ^2 statistic for 1 degree of freedom if the absorption line is just a statistical fluctuation (Cash, 1979).

In order to evaluate the statistical confidence of the line detection, we produced 10000 simulation spectra using the continuum model shown in Table 6.2 and the background without the absorption line. We then fitted the spectra with and without a Gaussian absorption or emission line model. We obtained $\Delta C \geq 4.33$ for 3.6% of the simulation spectra. This is consistent with the value expected from the χ^2 distribution (3.7%). We thus conclude that the chance probability for detecting such an absorption line at the very wavelength corresponding to O VIII Kα at the cluster redshift is 3.6%; in other words, the statistical confidence of the absorption line is 96.4%.

The width of the wavelength range where both the RGS1 and 2 operate is ~ 15.6 Å. Because the wavelength resolution is ~ 0.06 Å, there are about 260 independent wavelength bins. The probability for detecting an emission/absorption structure of $\Delta C \geq 4.33$ at *some* wavelength is almost unity with an expected occurrence of 9.4. We searched for such structures in the observed spectra, and actually found seven such structures other than that at 19.05 Å. However, none of them can be identified with any atomic emission/absorption line with a reasonable oscillator strength at $z = 0$, the cluster redshift, or the quasar redshift. Thus, these are all considered to be statistical fluctuations, and only the 19.05 Å feature can be real at a statistical confidence of 96.4%.

Table 6.3: Best-fit parameters of the O VII absorption line.

Galactic absorption	
$N_{\rm H}$	2.15×10^{20} cm^{-2} (fixed)
Absorption line	
Energy	571.46 eV (fixed)
Width (σ)	0.1 eV (fixed)
Normalization[a]	$< 5.3 \times 10^{-6}$ photons cm^{-2} s^{-1}
Power law	
Index	4.4
Normalization[b]	$1.58^{+0.35}_{-0.14} \times 10^{-4}$
Background power-law	
Index	2 (fixed)
Normalization[b]	1.76×10^{-4}
C-statistic	71.03
d.o.f	70

[a] 3σ upper limit.
[b] In units of photons keV^{-1} cm^{-2} s^{-1} at 1 keV.

We then investigated the systematic errors. First, we checked the RGS spectra of bright X-ray sources in the archival data to ensure that there is no instrumental feature at that wavelength. Then, since the estimation of an absorption line could be influenced by the determination of the continuum, we examined the dependence of the equivalent width on the wavelength region used in the fits and the choice of the continuum model. For this purpose, we changed the width of the wavelength band for fits from 1.0 to 2.8 Å and added a fifth-order polynomial to the continuum. We found that, as long as the width of the fitting region is wider than 1.6 Å, the variation of the equivalent width is smaller than 0.2 eV. When the fitting region is too narrow, the continuum level is not well constrained, and is strongly coupled to the equivalent width of the line.

6.2.4 OVII absorption line

There was no sign of an O VII absorption line at around 21.6 Å, where only the RGS1 operates. We fitted the spectrum between 20.5 Å and 22.5 Å. Background spectrum was fitted with a power-law of the index = 2. The best-fit parameters and errors are shown in Table 6.3. The 99.7% upper limit of the equivalent width was 2.8 eV at 21.69 Å (571.6 eV). The upper limit is not changed if the line energy is set to 21.60Å, i.e., O VII Kα energy of $z = 0$.

6.2.5 Column density of O VIII and O VII

Assuming that the absorption line is not saturated, the equivalent width is related to the ion column density as Equation (**??**). We used $f_{\rm os} = 0.70$ for the O VII resonance absorption line and $f_{\rm os} = 0.42$ for that of O VIII (Verner et al., 1996). Then, the O VIII column density was $(6.2^{+3.3}_{-4.4}) \times 10^{16}$ cm^{-2}, while the 99.7% upper limit on the O VII column density was

Figure 6.2: X-ray images obtained with EPIC-pn in the energy of 0.3 keV $< E <$ 3.0 keV. The left and right panels show the image before and after point source exclusion, respectively.

3.7×10^{16} cm^{-2}.

6.3 Excess Emission

6.3.1 Data reduction

We also analyzed the EPIC data, and searched for diffuse emission. Since we are mostly interested in the low-energy band, the pn detector is suitable for our analysis. Hence, we describe the results obtained from the pn data here. We confirmed that the MOS data gave similar results, but with larger errors. Figure 6.2 shows the images taken with EPIC-pn. The right panel displays the image after point sources were removed, that is, the area from which the spectrum was extracted.

The number of events above 10 keV is regarded as a good indicator of the internal background. Thus, we discarded the data where the rate of pattern 0 events in this energy range was larger than 0.7 cps. Then, we excluded LBQS 1218+1116 and other point sources using SAS edetect_chain, and accumulated photons from the diffuse emission in the 0.3–3 keV band over the field of view. To remove any contribution from the internal background, we subtracted data taken with the filter wheel in the closed position from the spectrum. After removing the point sources including LBQS 1228+1116 itself, the spectrum was extracted from 247.25 arcmin^{-2} region. The ancillary response file (arf) for flat (uniform) emission was created and used in the model fitting.

6.3.2 Fitting of the EPIC-pn spectrum

We modeled the spectrum with four components: hot intracluster medium (ICM) of the Virgo cluster, cosmic X-ray background (CXB), Milky Way halo (MWH), and Local Hot Bubble (LHB). For the CXB, MWH, and LHB, we used parameters obtained by Lumb et al. (2002) as a template. When we fixed the temperature of the MWH (0.20 keV), the temperature of the LHB (0.07 keV), and all of the CXB parameters, the temperature of

Table 6.4: Best-fit parameters of the emission spectrum.

Intracluster medium (ICM)	
Temperature kT	$2.17^{+0.14}_{-0.16}$ keV
Normalization K^a	$(1.21 \pm 0.08) \times 10^{-5}$
Abundance Z	$0.22^{+0.07}_{-0.05}$ $Z_\odot$
Excess emission	
Temperature kT	0.21 ± 0.01 keV
Normalization K^a	$(6.1 \pm 0.8) \times 10^{-6}$
Abundance Z	0.1 $Z_\odot$ (fixed)
$Z\ EM$	$(1.4 \pm 0.2) \times 10^{16}$ cm^{-5} $Z_{\rm ISM}$
Local hot bubble (LHB)	
Temperature kT	0.074 keV (fixed)
Normalization K^a	9.82×10^{-6} (fixed)
Abundance Z	1.0 $Z_\odot$ (fixed)
Milky-way halo (MWH)	
Temperature kT	0.204 keV (fixed)
Normalization K^a	6.42×10^{-7} (fixed)
Abundance Z	1.0 $Z_\odot$ (fixed)
Cosmic X-ray background (CXB)	
Index	1.42 (fixed)
Normalization^b	7.64×10^{-7} (fixed)
χ^2	205.36
d.o.f.	146

[a] $\int n_{\rm e}^2\ dV/4\pi(D_{\rm A}(1+z))^2$ per solid angle in units of 10^{14} cm^{-5} arcmin^{-2}, where $n_{\rm e}$ is the electron density, and $D_{\rm A}$ the angular size distance.
[b] In units of photons keV^{-1} cm^{-2} s^{-1} arcmin^{-2} at 1 keV.

the ICM determined by the fit became $2.0^{+0.2}_{-0.1}$ keV, which is consistent with that obtained with ASCA (2.14 ± 0.12 keV, Shibata et al. (2001). The normalization of the MWH was, however, a factor of 2.3-times larger than that obtained by Lumb et al. (2002). From an analysis of eight data sets obtained with XMM-Newton, Lumb et al. (2002) indicated that the mean deviation of 0.2–1 keV flux is about 35% from field to field. Therefore, the level of the warm-hot emission around LBQS 1228+1116 is significantly higher than that of the typical Galactic background, even if we consider its fluctuation.

We then fixed the parameters of the MWH, LHB, and CXB to those obtained by Lumb et al. (2002), added another optically-thin thermal plasma component, and fitted the entire spectrum. The normalization of the additional component (K) strongly couples with the oxygen abundance (Z), because most of the emission of thermal plasma of $T < 1$ keV is due to emission lines; ZK, which is proportional to $Z\ EM$, is a good parameter to indicate the normalization of the emission. Here, EM is the emission measure which is defined as Equation (2.12). Hence, we fixed $Z = 0.1\ Z_\odot$ in the spectral fitting and using $Z\ EM$ as an indicator of the line strength in the later discussion. The results are summarized in Table 6.4, and the best-fit models are shown in Figure 6.3. We used 'mekal' model of

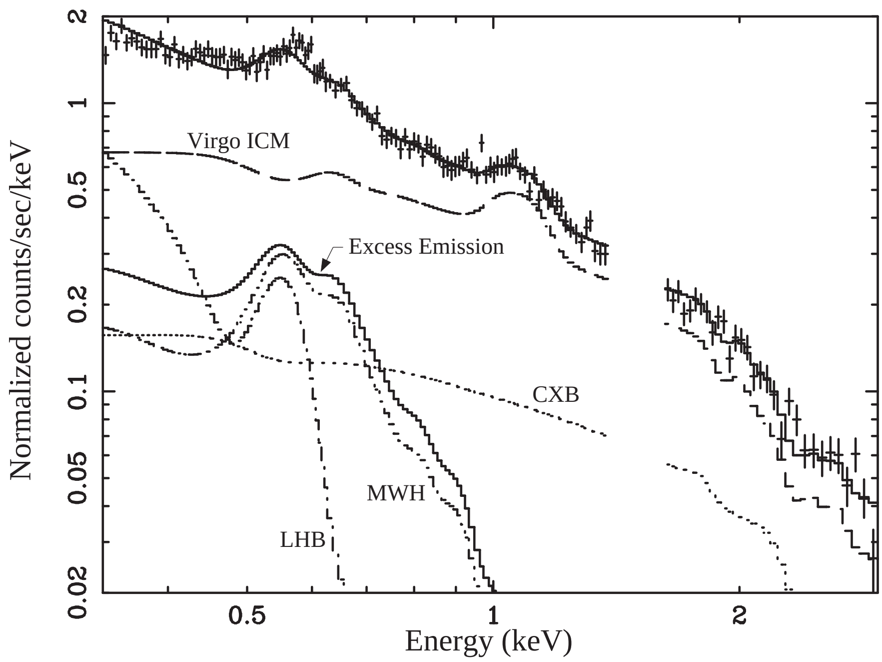

Figure 6.3: Soft X-ray spectrum of the diffuse emission obtained with EPIC pn. The aluminum line region was masked. Internal background was subtracted using data taken with a filter wheel in the closed position. The parameters of the cosmic X-ray background (CXB), Milky Way halo (MWH), and Local Hot Bubble (LHB) were fixed to those obtained by Lumb et al. (2002). The data require another component that can be modeled with an optically thin thermal plasma with $kT = 0.21$ keV.

XSPEC for the thermal plasma components. Note that the values in Table 6.4 is normalized to 1 arcmin^{-2} area and that the errors given in Table 6.4 do not contain the uncertainties of the background components. The normalization of the excess emission depends on the normalization, abundance, and temperatures of the MWH and LHB, while the temperature of the excess emission is sensitive to those of the MWH and LHB. $Z\ EM$ calculated from the product of K and Z is also shown in Table 6.4.

6.3.3 Comparison with the RASS map

It is known that the Virgo cluster is located close to the North Polar Spur (Loop I) (e.g., Irwin & Sarazin, 1996). To evaluate its effect, we inspected the RASS 3/4 keV map of the diffuse X-ray background (Snowden et al., 1997). The upper panel of Figure 6.4 shows a $25° \times 25°$ image centered at LBQS 1228+1116. The lower panel is a projection of the $0.5° \times 50°$ region shown in the upper panel. The levels of the background components (MWH, LHB, CXB) estimated from the data obtained by Lumb et al. (2002) and of the warm-hot emission plus LHB and CXB estimated from the present EPIC pn data are also shown in the panel with a dashed line and a solid line, respectively. The level of the west side of the Virgo cluster ($\lesssim -3°$) is consistent with that of Lumb et al. (2002) while that of the east side ($\sim +4°$) is significantly higher and comparable with the level of the warm-hot emission plus LHB and CXB at LBQS 1228+1116.

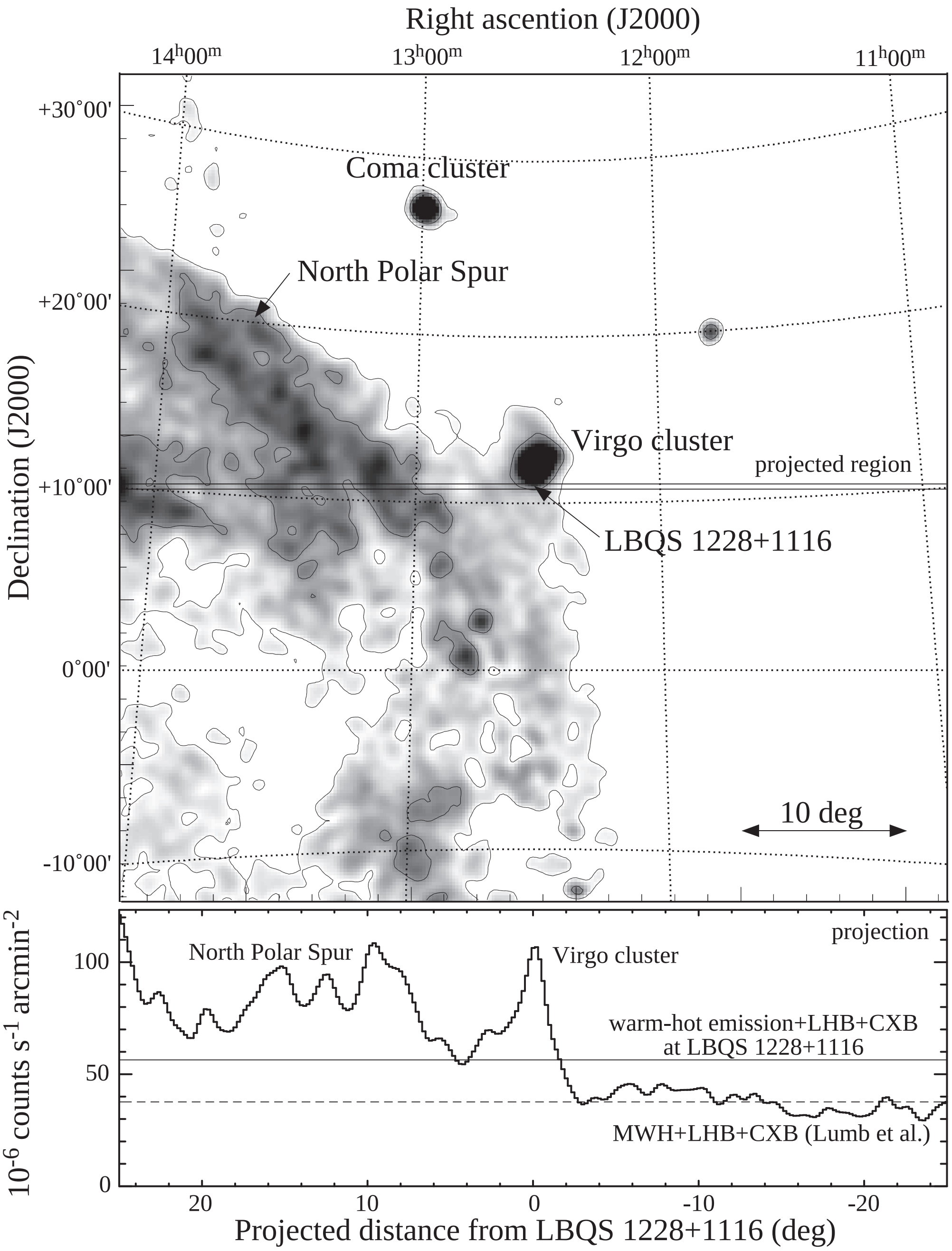

Figure 6.4: (Upper panel) $25° \times 25°$ image centered at LBQS 1228+1116, obtained from the RASS 3/4 keV map of the diffuse X-ray background (Snowden et al., 1997). The contours represent 80, 120, and 180 $\times\, 10^{-6}$ counts $\mathrm{s}^{-1}\,\mathrm{arcmin}^{-2}$. (Lower panel) Projection of the $0.5° \times 50°$ region shown in the upper panel. The solid line represents the level of the warm-hot emission plus LHB and CXB estimated from the present EPIC data, while the dashed line represents the background level (MWH, LHB, CXB) estimated from Lumb et al. (2002).

The consistency of the intensity of the multi-component model with the RASS map just outside of the Virgo cluster in the north and the west regions strongly suggests that the excess emission is associated with the Virgo cluster. However, a possible contribution by emission from the North Polar Spur cannot be excluded completely. We thus take the emission intensity as the upper limit for the emission from the WHIM around the Virgo cluster.

6.4 Properties of the WHIM

We detected (marginal) O VIII absorption and emission of warm-hot thermal plasma. Though either of them is not conclusive, the fact we observed both of them supports our detection of the WHIM.

6.4.1 Possible effect of saturation

Our results suggest the existence of a red-shifted O VIII resonance absorption line with a statistical confidence of 96.4% due to limited statistics. The velocity shift is 1253^{+881}_{-369} km s^{-1}, which is consistent with that of M87 ($cz = 1307$ km s^{-1}). Thus, we claim detection of the WHIM associated with the Virgo cluster. The equivalent width of the O VIII Kα line is $2.8^{+1.3}_{-2.0}$ eV. The intrinsic width of the line was not resolved, with an upper limit of $\sigma < 5.1$ eV (90%). This corresponds to a Doppler b parameter of < 3300 km s^{-1}. Because the Virgo cluster is thought to be elongated along the line of sight by 12–30 Mpc (Yasuda et al., 1997), a velocity difference of 800–2100 km s^{-1} is expected due to cosmological expansion. On the other hand, a turbulent velocity of a few hundred km s^{-1} is expected for WHIM from simulations (e.g., Cen & Ostriker (1999). From the curve of growth of the O VIII Kα absorption line (see Futamoto et al., 2004), the O VIII column density $N_{\rm OVIII}$ is estimated to be 6.8×10^{16}, 9.6×10^{16}, and 2.4×10^{17} cm^{-2}, respectively, for $b = 2100$, 800, and 400 km s^{-1} with $EW = 2.8$ eV. $N_{\rm OVIII} \sim 1 \times 10^{17}$ cm^{-2} is close to the maximum column density predicted by Fang and Canizares (2000), who investigated the column density of the WHIM gas by Monte-Carlo simulations.

6.4.2 Temperature

In contrast to the detection of the O VIII line, no O VII absorption line was detected. From the upper limit, the ionization fraction ratio of O VIII to O VII is constrained to be > 1.7, assuming that both of the O VIII Kα and O VII Kα lines are not saturated. If we further assume collisional ionization equilibrium, this implies $kT > 0.20$ keV (Mazzotta et al., 1998). However, photo-ionization by the cosmic X-ray and UV background radiation would increase the ionization fraction of O VIII if the density is as low as 10^{-5} cm^{-3} (Chen et al., 2003). Since we can constrain only the upper limit of the density (see next paragraph), this could be the case for the WHIM around the Virgo cluster, and its temperature could be lower. Note that the temperature suggested by O VIII/O VII ratio is consistent with that determined by emission analysis.

6.4.3 Density and line of sight length of the WHIM

We can determine the hydrogen density $n_{\rm H}$ and the product of the abundance and path length ZL separately as shown in § 5.4.2. Note that we adopted newer abundance $Z_{\rm ISM}$ instead of $Z_\odot$, so that the derived values are different from Fujimoto et al. (2004).

Using $N_{\rm OVIII}$ and $Z\ EM$, obtained with the observation, and assuming $T = 0.2$ keV, i.e., $f_{\rm ion\ OVIII} = 0.4$, determined by the emission analysis, $n_{\rm H}$ and ZL can be constrained as follows:

$$n_{\rm H} \lesssim 3.6 \times 10^{-5}\ {\rm cm}^{-3} \left(\frac{Z\ EM}{1.4 \times 10^{16}\ {\rm cm}^{-5}\ Z_{\rm ISM}}\right) \left(\frac{f_{\rm ion\ OVIII}}{0.4}\right) \left(\frac{N_{\rm OVIII}}{6.2 \times 10^{16}\ {\rm cm}^{-2}}\right)^{-1}, \quad (6.1)$$

$$ZL \gtrsim 3.1\ {\rm Mpc\ Z_{ISM}} \left(\frac{Z\ EM}{1.4 \times 10^{16}\ {\rm cm}^{-5}\ Z_{\rm ISM}}\right)^{-1} \left(\frac{f_{\rm ion\ OVIII}}{0.4}\right)^{-2} \left(\frac{N_{\rm OVIII}}{6.2 \times 10^{16}\ {\rm cm}^{-2}}\right)^{2}. \quad (6.2)$$

The derived density corresponds to a baryon overdensity of $\delta \lesssim 220$. Then, the hydrogen column density and the line-of-sight distance are constrained as a function of the abundance to

$$N_{\rm H} = 1.7 \times 10^{21}\ {\rm cm}^{-2} \left(\frac{Z}{0.2\ Z_{\rm ISM}}\right)^{-1} \left(\frac{f_{\rm ion\ OVIII}}{0.4}\right)^{-1} \left(\frac{N_{\rm OVIII}}{6.2 \times 10^{16}\ {\rm cm}^{-2}}\right), \quad (6.3)$$

$$L \gtrsim 15.5\ {\rm Mpc} \left(\frac{Z\ EM}{1.4 \times 10^{16}\ {\rm cm}^{-5}\ Z_{\rm ISM}}\right)^{-1} \left(\frac{Z}{0.2\ Z_{\rm ISM}}\right)^{-2} \left(\frac{f_{\rm ion\ OVIII}}{0.4}\right)^{-2} \left(\frac{N_{\rm OVIII}}{6.2 \times 10^{16}\ {\rm cm}^{-2}}\right)^{2}. \quad (6.4)$$

The depth of $\gtrsim 15.5$ Mpc is much larger than the linear dimensions of the Virgo cluster in the sky, but is consistent with the elongation of 12–30 Mpc suggested by Yasuda et al. (1997), which is understood as being a filament of the large-scale hierarchical structure along the line of sight. Note that the line broadening due to the Hubble flow of the 15.5 Mpc line-of-sight distance corresponds to about 2.4 eV. This is much smaller than the 90% upper limit of the line width obtained from the present data. However, it could be resolved if the statistics were good enough, since it is comparable to the energy resolution of the RGS (~ 2 eV FWHM).

6.4.4 The mass of the WHIM

Here we estimate the mass of the WHIM assuming that the region that contains the WHIM has a uniform cylindrical shape. We do not assume spherical shape because the distribution of the galaxies seems elongated in the line-of-sight direction. The mass of the WHIM is calculated as

$$M_{\rm WHIM} = \frac{N_{\rm OVIII}}{f_{\rm ion\ OVIII} Z} \frac{m_{\rm p}}{X} \pi R_{\rm WHIM}^2, \quad (6.5)$$

or

$$M_{\rm WHIM} = 6.0 \times 10^{13}\ M_\odot \left(\frac{R_{\rm WHIM}}{1\ {\rm Mpc}}\right)^2 \left(\frac{N_{\rm OVIII}}{6.2 \times 10^{16}\ {\rm cm}^{-2}}\right) \left(\frac{f_{\rm ion\ OVIII}}{0.4}\right)^{-1} \left(\frac{Z}{0.2\ Z_{\rm ISM}}\right)^{-1}, \quad (6.6)$$

where $R_{\rm WHIM}$ is the radius of the cylindrical region.

We cannot determine $R_{\rm WHIM}$ from our observation. If we assume $R_{\rm WHIM} = r_{\rm QSO} = 0.45$ Mpc, where $r_{\rm QSO}$ is the distance of LBQS 1228+1116 from M87, the mass is $M_{\rm WHIM} =$

1.2×10^{13} $M_\odot$. This $R_{\rm WHIM}$ would be thought as the lower limit of the radius. If $R_{\rm WHIM} = r_{\rm vir} = 1.8h_{70}^{-1}$ Mpc (Girardi et al., 1998) is adopted, $M_{\rm WHIM} = 2.0 \times 10^{14} M_\odot$. The mass of the hot gas was estimated by Schindler et al. (1999). By extrapolating their result, we obtain the mass within 1.8 Mpc of $5 \times 10^{13} M_\odot$. The former value (the lower limit) of $M_{\rm WHIM}$ is 24% of the mass of the hot gas, while the latter is 390% of the hot gas mass. Note that the distribution of galaxies in the Virgo cluster suggests $L/R_{\rm WHIM} \sim 5$ (see Figure 3.5).

Chapter 7

A2218 vicinity

7.1 Observations

We carried out four observations to study the warm-hot gas in the A2218 vicinity with the XIS instrument onboard *Suzaku*: two on the cluster and two in offset regions whose locations are different from each other. The offset observations were performed to measure the foreground Galactic contribution, which can produce a large ambiguity in the study of soft emission around clusters. Fig. 7.1 is a map of the *ROSAT* R4 band after removing bright point sources (Snowden et al., 1997). This energy band is sensitive to O VII and O VIII emission lines, which are strong in the Galactic emission, and hence is suitable to study their fluctuations.

We examined the *ROSAT* map (Fig. 7.1) and selected the location of offset pointings so that the Galactic emission level is similar to that in the vicinity of A2218. Also, the distance from A2218 is large ($\gtrsim 1^\circ$ or 10.7 Mpc at the A2218 redshift), so the data from the offset regions should be free from the putative large-scale filament around A2218. The observed locations are shown in Fig. 7.1 and Table 7.1, as well as the position of A2218. Hereafter we call the four observations A2218-1, A2218-2, Offset-A, and Offset-B, respectively. A2218-1 and Offset-A were observed in early October, 2005, and the others in late October. The observation sequence numbers and dates are summarized in Table 7.2.

Table 7.1: Position of the A2218 and offset pointing

	(RA, Dec)	(l, b)
A2218	($16^h35^m54^s$, $66^\circ13'00''$)	(97.7449, 38.1235)
Offset-A	($16^h17^m48^s$, $65^\circ27'36''$)	(97.7423, 40.1239)
Offset-B	($16^h39^m31^s$, $66^\circ13'31''$)	(96.4000, 38.1002)

The XIS instrument was operated in normal mode in all the observations presented in this paper. We used event files of version 0.7 products[1]. Events of 3×3 and 5×5 observation modes were combined. The first few kiloseconds of each observation, when the pointing

[1]Version 0 processing is an internal processing applied to the Suzaku data obtained during the SWG phase. Aspect correction and fine tuning of the event time tagging are skipped in this version. Times when the elevations from the bright and dark Earth are $> 20^\circ$ and $> 5^\circ$ are excised in standard data processing.

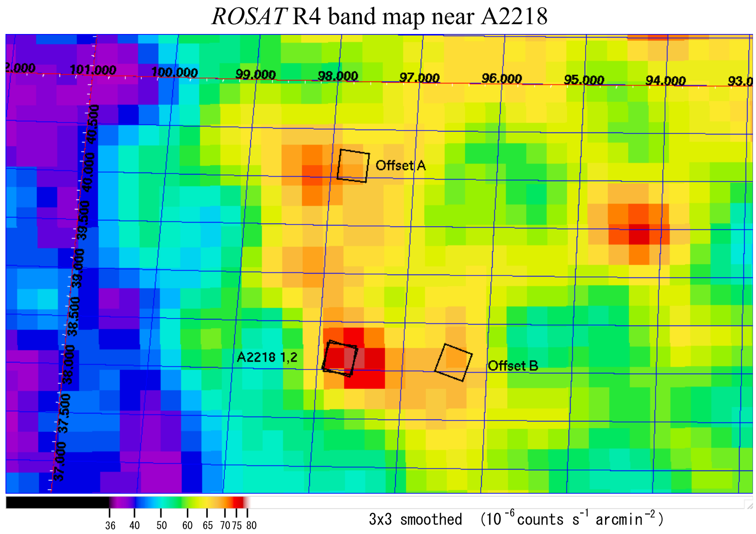

Figure 7.1: *ROSAT* R4 band image around A2218 (Snowden et al., 1997) in Galactic coordinates. The field of view of XIS in the four observations are indicated by black squares. Most of the emission in this band is O VII and O VIII line.

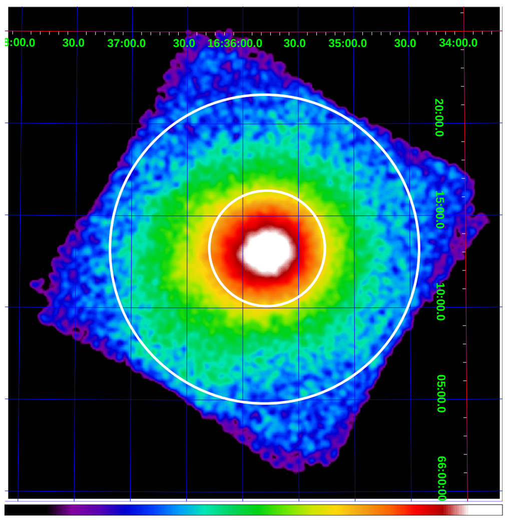

Figure 7.2: Image of A2218 in the 1.0–4.0 keV band observed with the XIS. The events of the two observations obtained by four CCDs were summed. The spectra were extracted from the annulus between the two white circles. Vignetting effects were not taken into account for this image and background events were not subtracted. The grid indicates the coordinates in J2000.0.

direction had not yet stabilized, were excluded. The resulting image of A2218 in the 1.0–4.0 keV energy band is shown in Fig. 7.2. Data from the two observations and the four CCDs are combined. The white circles indicate the region where we extracted the spectra. The radii are $3'$ and $8'$ from the cluster center, corresponding to 540 and 1430 kpc at the source, respectively.

After the launch of *Suzaku*, a time and position dependent contamination of the XIS optical blocking filter (OBF) was found. The source is probably outgassing from the satellite. The level of contamination increases with time and is different from sensor to sensor. The time and position dependence of the contamination thickness has been empirically modeled by the XIS team. At the time of our observations, the effective area at 0.5 keV was on average 25% lower than that of the pre-launch calibration. The two observations of A2218 were 25 days apart, and the count rates at 0.5 keV were different by 9% and 13% for the BI and the combined FI sensors, respectively. This is consistent with the expected drop of 8% for both sensors within statistical errors.

Table 7.2: *Suzaku* observations of A2218 and offset pointing

	Sequence number	Date	Exposure after processing	Net exposure using all COR	Net exposure using COR> 8 Gev c^{-1}
A2218-1	100030010	2005-10-01–2005-10-02	46.4 ks	44.9 ks	38.2 ks
A2218-2	800019010	2005-10-26–2005-10-27	32.8 ks	32.3 ks	28.8 ks
Offset-A	100030020	2005-10-02–2005-10-03	44.6 ks	44.6 ks	39.0 ks
Offset-B	800020010	2005-10-27–2005-10-27	15.0 ks	15.0 ks	12.0 ks

7.2 Spectral analysis

7.2.1 Analysis method

We removed flickering CCD pixels, which cause a large noise component below 0.5 keV. We also excluded apparent point sources that were found in the Offset-A image. Although the fluxes of these point sources were lower than the detection limit for the A2218 image, we removed them because we are interested in the upper limits of the soft excess emission. The spectra were then extracted in the annular region between $3'$ and $8'$ from the cluster center using XSELECT distributed in HEASOFT 6.0.4. We define the cluster center as (DETX, DETY) = (499, 530) in detector coordinates for all observations and all sensors. Note that the boresight of all XIS sensors coincide within $20''$. We have chosen the inner radius to be $3'$ in order to exclude the bright central region, in which the strong emission of the hot ICM hampers the study of warm-hot emission. We also excluded the region outside of $8'$ because the position dependence of the contamination on the OBF is not well known there. Although the XIS sensors are always illuminated by ^{55}Fe calibration sources at the field edge, we did not remove these regions in the present analysis.

To estimate and subtract the internal background, we also extracted spectra from night Earth observations distributed by the XIS team. It is known that the variation of the internal background spectrum is well correlated with the cut-off rigidity (COR) at the position of the satellite; the smaller the COR value is, the larger the background level becomes. To estimate accurately the internal background level, we collected events when the detector was looking at the dark Earth (night Earth events) and sorted them by COR. We extracted the spectrum for each 1 GeV c^{-1} interval of COR, and then added them weighted by exposure time for the respective COR range in the actual observation. This process gives different night Earth spectra for the four observations, since the detailed distribution of COR was different among the observations. The background spectra were extracted from the same region in detector coordinates as the corresponding observation in order to avoid possible systematic effects due to positional variation of the detector background.

We used response matrix files (RMFs) ae_xi[0123]_20060213(c).rmf distributed by the XIS team for spectral fitting. On the other hand, we generated the ancillary response files (ARFs) with the arf builder 'xissimarfgen', which is based on ray-tracing (Ishisaki et al. 2006). The change of the effective area with time in the soft X-ray energy range, due to the increase of OBF contamination, was taken into account by the following method. The ARFs were created separately for each observation, according to the observation date. We used the ae_xi[0123]_contami_20060525.fits contamination tables to model the composition and position dependence of the contaminant, in which the C/O ratio of contaminant was assumed to be 6. Note that the effective area for diffuse sources depends on the sky distribution of the flux, because the quantum efficiency varies with the detector position due to vignetting and contamination thickness. We adopted the Suzaku XIS image (1.0–4.0 keV) of A2218 for the incident flux distribution, in which the two observations by the four sensors were all summed (see Fig. 7.2). We assumed a uniform flux distribution for the offset pointings.

In the analysis shown below, the spectra and ARFs for A2218-1 and A2218-2 were added using the ftools mathpha and addarf, respectively. Further, the spectra and response (RMFs and ARFs) of the three FI sensors were combined using ftools mathpha and marfrmf, respectively. We confirmed that consistent results were obtained with this treatment within the statistical error. We fitted spectra of the offset observations in the 0.35 keV $< E <$ 5.0 keV energy range for the BI and 0.40 keV $< E <$ 5.0 keV except the energy of anomalous response at the Si K-edge, 1.825–1.840 keV, for the FI. When we fitted the spectra of A2218, the energy range was extended up to 7.0 keV in order to cover the Fe-K lines. We excluded 5.85–5.95 keV and 6.45–6.55 keV, because the slight difference in intensity of Mn K emission lines from the ^{55}Fe calibration sources between A2218 observations and night Earth observations causes relatively large residuals. The spectra of A2218 (black), Offset-A (red), and Offset-B (green), as well as the night Earth spectra (blue) are shown in Fig. 7.3. Left and right panels are for BI and FI spectra, respectively. The difference in the detector area due to point-source exclusion was corrected in the figure for illustrative purposes. We mainly performed simultaneous fits for the two spectra obtained by the BI and the combined FI sensors. However, it was also confirmed that the spectrum with the BI sensor only gave consistent results. This indicates that the uncertainty in the FI response around 0.5 keV is not crucial compared with the statistical errors in the BI spectrum.

Evaluation of the systematic uncertainties is crucial in constraining the emission from the WHIM. Firstly, the emission is in the soft X-ray region where the XIS has various systematic uncertainties, so we have to look into many possible effects. Secondly, the observation was carried out only three months after the launch of *Suzaku*, and time variation of the detector response needs to be carefully considered.

The first uncertainty is the detector response. The largest systematic uncertainty in the detector response is the thickness of contaminant on the OBF of the XIS. In the 0.4–0.6 keV band, most of the photons we observe are thermal emission from the ICM. If we underestimate the contaminant thickness, the flux from the ICM would be overestimated in $E \lesssim 1$ keV, because the temperature and abundance are strongly constrained by the data in the higher energy range $E \gtrsim 1$ keV. This naturally leads to an underestimation of the soft-excess flux. Therefore, we also considered a *thicker* contaminant model at the upper limit of the uncertainty range. We generated ARFs with 20% thicker contaminant using xissimarfgen assuming the observation occurred seventeen days later than it actually did. This 20% increase is a reasonable value, given the additional uncertainties in the response to diffuse emission and in early observations. The energy resolution of the XIS worsens with time. At the time of our observations, the energy resolution had degraded by ~ 20 eV (FWHM) at 5.9 keV (from 130 eV to 150 eV). This effect was investigated by smoothing the response with a Gaussian. Since we have no information about the degradation at ~ 0.5 keV, we tried Gaussians with sigmas of 5 eV, 10 eV, 15 eV, 20 eV, 30 eV and 35 eV. With this smoothing, the spectral resolution at $\sim$0.5 keV increases from 40 eV to 42 eV, 46 eV, 53 eV, 62 eV, 81 eV and 91 eV, respectively. The results are presented later. The internal background of the XIS is quite stable, and there were no "background flares" during our observations. However, when COR is low (COR$\lesssim 6$ GeV c^{-1}), the internal background level becomes comparable to the X-ray background in the $E > 3$ keV range. Therefore, we also extracted spectra with the condition COR > 8 GeV c^{-1} to examine this systematic effect.

Another uncertainty is the spatial variation of the Galactic emission. The *ROSAT* R4 map shows $\sim 10\%$ variations among the A2218, Offset-A and Offset-B fields. The purpose of the two offset observations (Offset-A and Offset-B) was to look at the spectral variation in the Galactic emission and to include it in the analysis. Besides the inclusion of this variation, we also extended our upper limit for the soft excess by assuming 10% fainter Galactic emission.

7.2.2 Offset pointings

Before the analysis of the A2218 spectrum, we analyzed data from the offset pointings to estimate the spectrum of the Galactic emission. The diffuse X-ray background at high Galactic latitude can be divided into three components: i.e. the local hot bubble (LHB), the Milky Way halo (MWH) and the extragalactic power-law (CXB) components (Snowden et al., 1998). Typical temperatures are about 0.1 keV for the LHB and 0.2–0.3 keV for the MWH, while the CXB spectrum has a photon index of 1.4. The LHB is thought to surround the solar system with a ~ 100 pc scale, and hence it has no Galactic absorption. The CXB component is extragalactic and known to be uniform over the entire sky. In contrast, the level of LHB and MWH components vary from position to position. Lumb et al. (2002) reported that the mean deviation of the 0.2–1.0 keV intensity is $\sim 35\%$ from field to field.

Our purpose here is to constrain the spectra of the two Galactic components so as to obtain reliable background data for the estimation of the warm emission around A2218. Spectra for an annular region with $r = 3' - 8'$ were produced for the Offset-A and Offset-B data. XSPEC v11.3.2r was used in the spectral analysis. The spectra, from which non X-ray background was subtracted, were fitted with a model for the sum of LHB, MWH and CXB. CXB and MWH components were absorbed by Galactic absorption characterized by $N_{\rm H} = 3.24 \times 10^{20}$ cm^{-2} (Dickey & Lockman, 1990). The collisionally ionized thermal plasma model APEC was used in XSPEC to fit the LHB and MWH spectra, with abundance and redshift fixed to 1 solar and 0, respectively. The photon index of the power-law CXB model and the temperature of the LHB were fixed to 1.4 and 0.08 keV, respectively. The normalizations of the FI and BI sensors were allowed to take different values.

The best-fit parameters and the model curves are shown in Table 7.3 and Fig. 7.4. In Table 7.3, parameters except for the FI/BI ratio are for the BI spectra. Acceptable fits were obtained for the two spectra and the parameters of the Galactic emission were

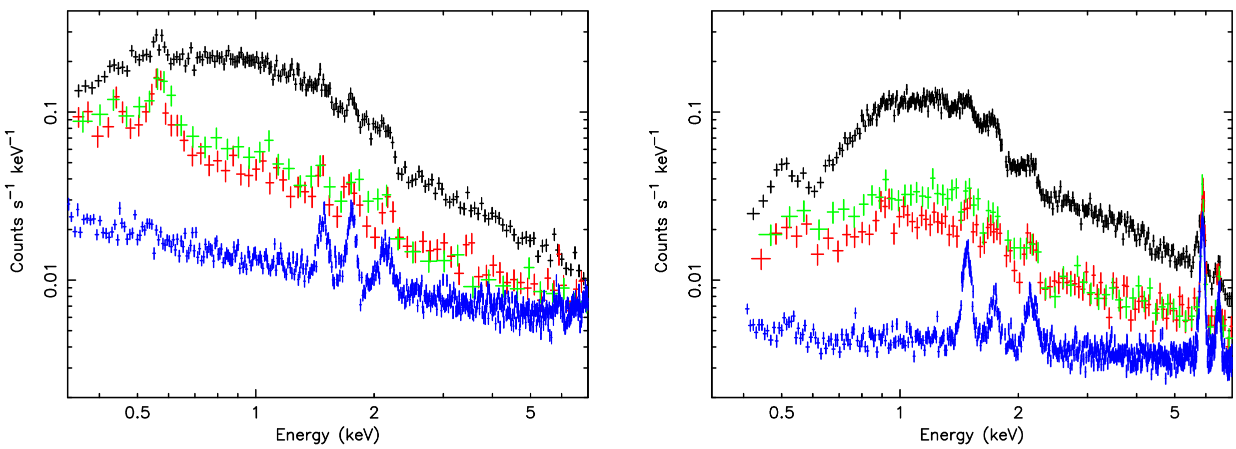

Figure 7.3: Spectra of A2218 taken with the (left) BI and (right) FI chips, where three FI spectra were averaged. Black, red, green and blue points show A2218, Offset-A, Offset-B, night earth spectra, respectively. The strong peaks at 5.9 keV and 6.5 keV in the right panel are due to the calibration sources.

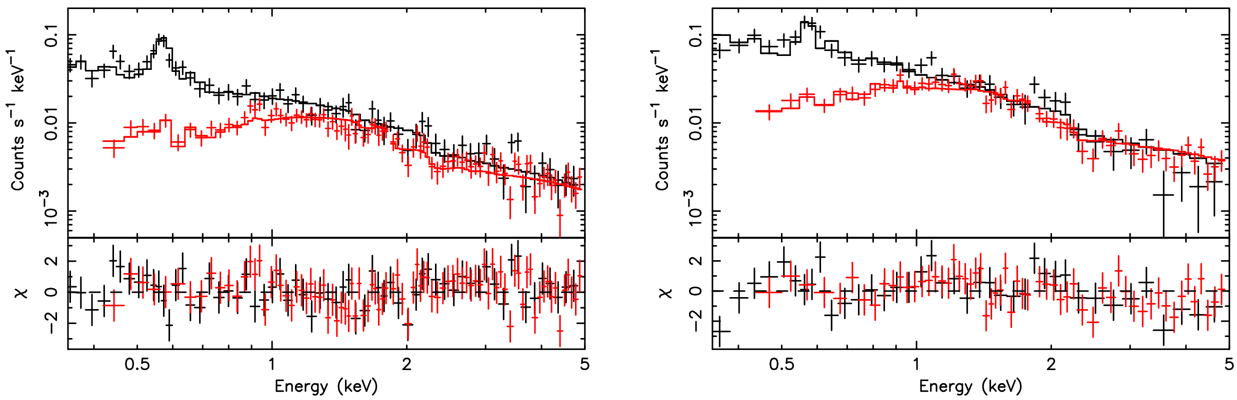

Figure 7.4: Spectra and best-fit models, and residuals of offset observations. (left) Offset-A, (right) Offset-B. Black and red represents BI and FI sensors.

well constrained. The normalization of the CXB component agrees with previous reports (Kushino et al., 2002). The flux in the 0.5–2.0 keV band of Offset-A and Offset-B observation differs by $\sim 10\%$. Not only the flux, but also the shape of the best-fit model is different between the two observations, which is either due to the poor statistics of the Offset-B observation or real variations in the Galactic emission.

7.2.3 A2218

7.2.3.1 Single temperature model

The A2218 spectrum for the radial region of $3' - 8'$ was analyzed here. The summed FI and the BI spectra were fitted simultaneously. Before testing the warm emission in the model, we first fitted with a model only including the thin thermal plasma (ICM) and the

Table 7.3: Best-fit parameters of offset pointings

Parameter	Offset-A	Offset-B
LHB kT (keV)	0.08 (fixed)	0.08 (fixed)
LHB Normalization[a]	$3.2 \pm 1.0 \times 10^{-6}$	$6.2^{+0.7}_{-1.7} \times 10^{-6}$
MWH kT (keV)	$0.158^{+0.028}_{-0.018}$	$0.248^{+0.033}_{-0.031}$
MWH Normalization[a]	$6.7^{+3.3}_{-2.5} \times 10^{-7}$	$5.0^{+1.5}_{-1.0} \times 10^{-7}$
CXB Photon index	1.4 (fixed)	1.4 (fixed)
CXB Normalization[b]	$8.5 \pm 0.5 \times 10^{-7}$	$8.5 \pm 0.7 \times 10^{-7}$
FI/BI ratio	0.84 ± 0.05	1.04 ± 0.09
χ^2/dof	154.03/149	100.45/93

[a] $\int n_e n_H \, dV/4\pi(D_A(1+z))^2$ per solid angle in units of 10^{14} cm^{-5} arcmin^{-2}, where n_e is the electron density, n_H the hydrogen density, and D_A the angular size distance.
[b] In units of photons cm^{-2} s^{-1} keV^{-1} arcmin^{-2} at 1 keV

Table 7.4: Best-fit parameters of A2218 with single temperature model

Parameter	Offset-A Case	Offset-B Case
LHB kT (keV)	0.08 (fixed)	0.08 (fixed)
LHB Normalization[a]	3.2×10^{-6} (fixed)	6.2×10^{-6} (fixed)
MWH kT (keV)	0.158 (fixed)	0.248 (fixed)
MWH Normalization[a]	6.7×10^{-7} (fixed)	5.0×10^{-7} (fixed)
CXB Photon index	1.4 (fixed)	1.4 (fixed)
CXB Normalization[b]	8.5×10^{-7} (fixed)	8.5×10^{-7} (fixed)
ICM kT (keV)	$5.40^{+0.27}_{-0.15}$	6.00 ± 0.22
ICM Z (solar)	0.20 ± 0.04	0.21 ± 0.04
ICM z	0.1756 (fixed)	0.1756 (fixed)
ICM Normalization[a]	$2.08 \pm 0.03 \times 10^{-5}$	$2.00 \pm 0.03 \times 10^{-5}$
FI/BI ratio	0.89 ± 0.01	0.90 ± 0.01
χ^2/dof	475.21/475	520.72/475

[a] $\int n_e n_H \, dV/4\pi(D_A(1+z))^2$ per solid angle in units of 10^{14} cm^{-5} arcmin^{-2}, where n_e is the electron density, n_H the hydrogen density, and D_A the angular size distance.
[b] In units of photons cm^{-2} s^{-1} keV^{-1} arcmin^{-2} at 1 keV

background emission determined from the offset-region spectra. We tried two models for the background: namely, the best-fit models for the BI spectra determined from the Offset-A and Offset-B observations. We fixed all the parameters for the background spectrum consisting of LHB, MWH and CXB at the best-fit values. The redshift of the hot ICM was fixed at 0.1756. We allowed the FI/BI normalization to be free again. The results of the fit are summarized in Table 7.4 and in Fig. 7.5. The different background (Offset-A or B) gives an ICM temperature differing by about 10%, while similar metal abundance values were obtained in the two cases. The temperature and abundance are generally consistent with previously determined values; *XMM-Newton* spectra indicates $kT \sim 5$ keV in $3' - 5'$ and

$Z = 0.13 \pm 0.04$ solar in the central $5'.1$ region (Pratt et al., 2005), while *Chandra* estimated kT to be 6.9 ± 0.5 and Z to be 0.20 ± 0.13 in the central $5'.1$ region (Machacek et al., 2002). The detailed analysis of the temperature and abundance of the ICM will be reported elsewhere.

The spectra were well fitted with this simple model, suggesting that no obvious soft excess is present. The residual of the spectral fit should indicate a feature, such as that caused by redshifted oxygen lines, if warm emission indeed gives a significant contribution. Both panels in Fig. 5 suggest some features around 0.57 keV and 0.68 keV: the former is a positive residual, while the latter negative. Both features are near the strong Galactic O emission lines: O VII at 574 eV and O VIII at 654 eV, and not identical to those of redshifted O lines at the redshift of A2218. Their levels are less than that of Galactic emission by a factor of 3–10. Hence, they may originate in the fluctuation or incomplete modeling of Galactic emission. Note that the O VIII line (654 eV) at the source is redshifted to 556 eV, which is close to the strong O VII line (574 eV) in the Galactic emission. Thus it is rather difficult to detect the warm gas with this line. The redshifted O VII line (574 eV shifts to 488 eV) is also close to the peak caused by the oxygen edge of the detector deadlayer and OBF, in particular for the FI sensors (see Fig. 4 of Koyama et al. 2007). These situations make the XIS sensitivity to warm gas for a source with redshift similar to that of A2218 poorer than it is at other redshifts. We will carry out a quantitative evaluation in the next section.

7.2.3.2 Constraint on redshifted O lines

We performed another spectral fit by adding two Gaussian emission lines to the model, in order to test for the existence of redshifted O lines. The energies of the lines were fixed to 488.22 eV and 555.99 eV, which correspond to O VII (resonance) and O VIII lines at $z = 0.1756$. Although the energy of the O VII line could be at most 10 eV lower due to the contribution of intercombination and forbidden lines, we confirmed that the results shown below are not affected by that difference in energy. The intrinsic widths were fixed to zero. The temperature and abundance of the ICM component were free parameters, while all the background parameters (for LHB, MWH and CXB) including the normalizations were fixed at the best-fit values determined with the Offset data described in § 7.2.3.1. The free parameters were the temperature kT, abundance Z and normalization of the ICM, the surface brightness I of redshifted O VII and O VIII lines, and FI/BI normalization ratio. We again tried the two background models, determined from the Offset-A and Offset-B observations, respectively.

The best-fit parameters and improvement in χ^2 values are shown in Table 7.5. The obtained surface brightness I of the lines is small and consistent with zero; the improvement in χ^2 is less than 2.71 (90% significance for 1 free parameter). We then constrained the allowed O line intensity range. The upper limits for the O VII and O VIII I were estimated from that causing an increment of the χ^2 value by 4.0 (2σ limit) over the minimum (best-fit) level. In this process, we allowed the other free parameters (i.e., the ICM temperature, abundance, normalization, and FI/BI ratio) to vary. The upper limits of the two lines were determined separately, and the values are also shown in Table 7.5 in parentheses. Fig. 7.6 shows the model with the upper-limit intensities of the O VII and O VIII lines in the upper 2 panels; the left panel is the case with the background of Offset-A, while the right panel is for Offset-B. The upper limits are shown with solid lines, while the background spectrum is

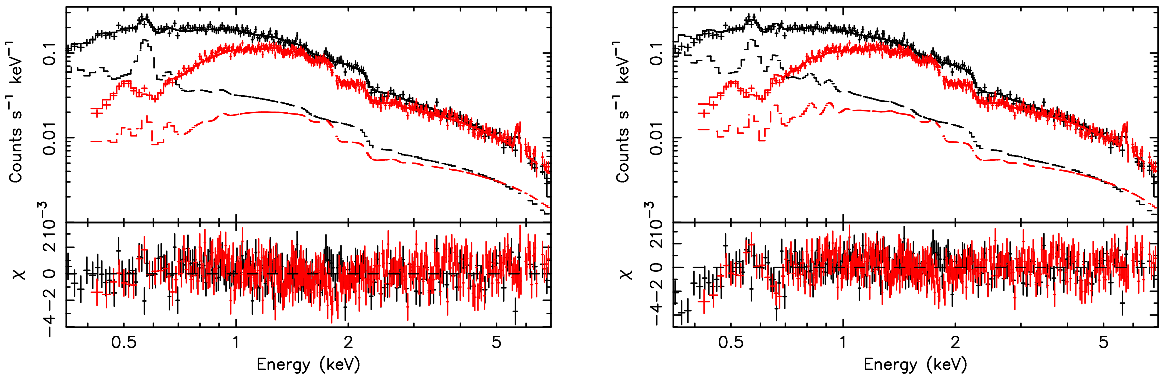

Figure 7.5: Spectra fitted with the best-fit models, and residuals of A2218 observations, in which the data from the two observations were merged. Galactic components are fixed to (left) Offset-A, and (right) Offset-B models, respectively. Black and red indicate BI and FI sensors. The contribution of the Galactic emission, determined by offset observations, are also indicated by dashed lines.

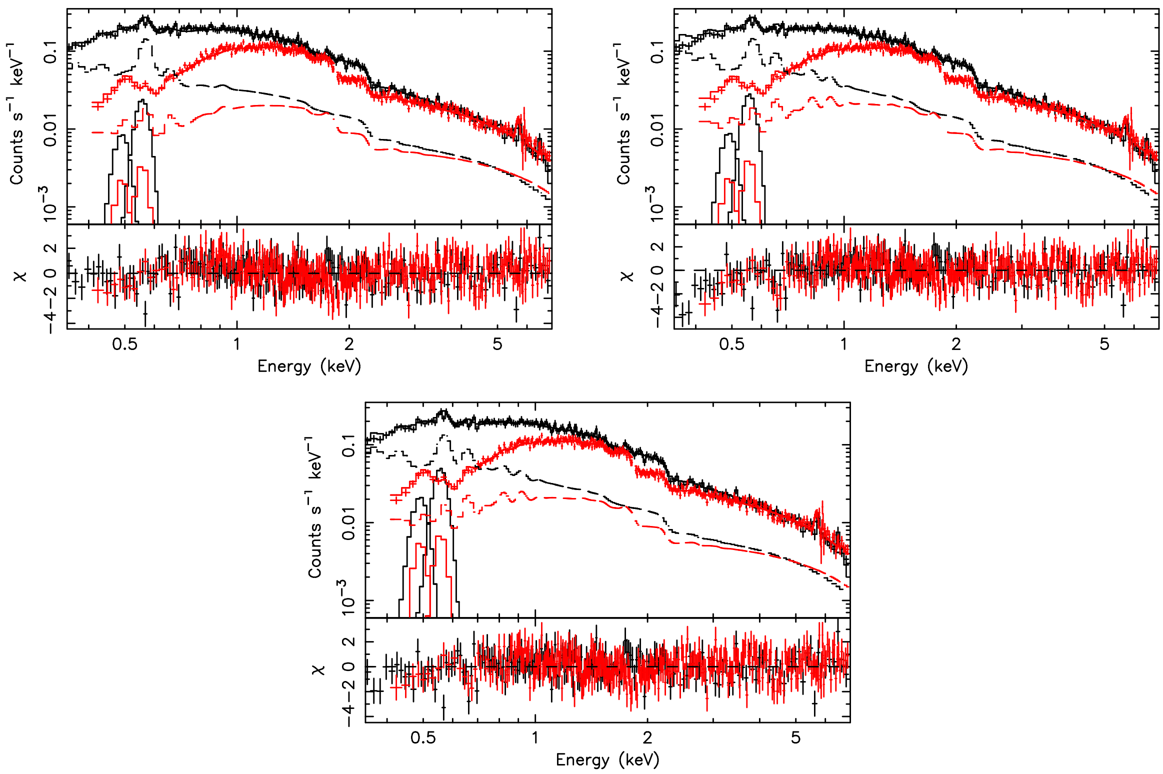

Figure 7.6: A2218 BI (black) and FI (red) spectra and models with redshifted O lines. The two emission lines indicated with solid lines in the 0.4–0.6 keV range show the maximum allowed level (2σ) of O VII and O VIII lines. Dashed lines indicate the background emission. (upper left) without considering systematic uncertainty, using the best-fit model of Offset-A observation as the Galactic emission. (upper right) without considering systematic uncertainty, using Offset-B observation. (bottom) the model of maximum O line intensity after considering systematic uncertainties: assuming no O in the ICM, with ARFs of 20% thicker contaminant and with 10% fainter Galactic model than the one determined from the Offset-B observation. The O VII and O VIII surface brightness was $1.1 \times 10^{-7}$and 3.0×10^{-7} photons cm^{-2} s^{-1} arcmin^{-2}, respectively.

shown with dashed lines. The upper limits of the two O lines are 10–20% of the background level at the center energy of each line.

It should be noted that the O VIII line is also produced by the ICM ($T \sim 5$ keV), while O VII is not. The intensity, which depends on the temperature and O abundance, is 2×10^{-8} photons cm^{-2} s^{-1} arcmin^{-2} assuming the parameters in Table 7.4. However, this value contains an uncertainty; while the abundance was mostly determined by the Fe K and L features in the fit, Fe and O abundances may have a different value. We estimated the upper limit of I for the redshifted O VIII line from the WHIM in the extreme case of no O in the ICM, because this situation gives the largest contribution from the WHIM. The upper limit then increased to 1.6×10^{-7} photons cm^{-2} s^{-1} arcmin^{-2} and 1.8×10^{-7} photons cm^{-2} s^{-1} arcmin^{-2} for the Offset-A and Offset-B backgrounds, respectively.

Next, we investigated how the upper limits of I change by considering the systematic uncertainties described in § 7.2.1. We already checked one of these uncertainties in Table 7.5: variation of the Galactic emission between Offset-A and Offset-B fields. The difference is $\lesssim 20\%$. When we used the ARFs with 20% thicker contaminant, the upper limits of the O VII and O VIII lines increased by $\sim 130\%$ and $\sim 30\%$, respectively. These limits further increase by $\sim 15\%$ and $\sim 30\%$ for the respective lines, if we adopt 10% fainter Galactic emission. On the other hand, the upper limits do not increase when we select the data for the low background condition (COR> 8 GeV c^{-1}) or when the energy resolution of the detector was artificially degraded by 5–35 eV. To summarize, the conservative upper limits are derived by assuming no O in the ICM and employing the ARFs with 20% thicker contaminant and 10% fainter Galactic model for the Offset-B observation; the values are 1.1×10^{-7} photons cm^{-2} s^{-1} arcmin^{-2} and 3.0×10^{-7} photons cm^{-2} s^{-1} arcmin^{-2} for O VII and O VIII lines, respectively. We adopt these values as the upper limits of the O line intensity around A2218, considering both statistical and systematic errors. The spectra with the model with these upper limits are shown in the lower panel of Fig. 7.6. Note that even after considering these systematic errors, the upper limits are still $\sim 30\%$ of the level of the Galactic emission at the same energy.

7.3 Discussion

We have observed A2218 with the XIS instrument onboard *Suzaku* to search for the redshifted O emission lines from the WHIM, which is possibly forming a large-scale filament around the cluster. The object was selected because its redshift ($z = 0.1756$) would allow the XIS to separate the WHIM lines from the Galactic ($z = 0$) ones, and because an elongated structure in the line-of-sight direction was suggested from the previous studies of this cluster. We detected no redshifted O lines, and set a constraint on their intensities. In this section, we compare our constraints on the line intensity with those reported in other works and also discuss the future prospect of studying the WHIM emission with the *Suzaku* XIS.

7.3.1 Comparison with other results

Kaastra et al. (2003) and Finoguenov et al. (2003) reported positive detections of O lines around clusters of galaxies based on *XMM-Newton* observations. Kaastra et al. (2003) detected significant O lines in three clusters, Sérsic 159–03, MKW 3s and A2052, and possible,

Table 7.5: Best-fit parameters using a model with redshifted O lines

Parameter	Offset-A Case	Offset-B Case
ICM kT (keV)	$5.41^{+0.28}_{-0.16}$	6.02 ± 0.22
ICM Z (solar)	0.20 ± 0.04	0.21 ± 0.04
ICM z	0.1756 (fixed)	0.1756 (fixed)
ICM Normalization[a]	$2.08 \pm 0.03 \times 10^{-5}$	$2.00 \pm 0.03 \times 10^{-5}$
O VII E (eV)	488.22 (fixed)	488.22 (fixed)
O VII I[b c]	$0\ (< 3.7 \times 10^{-8})$	$0\ (< 3.9 \times 10^{-8})$
O VIIII E (eV)	555.99 (fixed)	555.99 (fixed)
O VIII I[b c]	$4.0\ (< 13.4) \times 10^{-8}$	$6.8\ (< 15.8) \times 10^{-8}$
FI/BI ratio	0.89 ± 0.01	0.90 ± 0.01
$\Delta\chi^2/\Delta dof$	0.78/2	2.25/2

[a] $\int n_e n_H \, dV/4\pi(D_A(1+z))^2$ per solid angle in units of 10^{14} cm^{-5} arcmin^{-2}, where n_e is the electron density, n_H the hydrogen density, and D_A the angular size distance.
[b] In units of photons cm^{-2} s^{-1} arcmin^{-2}
[c] Upper limits are quoted in 2σ confidence level.

but not uniquely proven, O lines in the Coma and A1795 clusters. Finoguenov et al. (2003) detected the O lines in the outskirts of the Coma cluster, in particular, the Coma-11 field. Fig. 7.7 compares the O line surface brightness I for their observations and our results. The left and right panels are for the O VII and O VIII cases, respectively. The intensity of the O lines of Galactic emission measured by a microcalorimeter experiment of McCammon et al. (2002), the one compiled by Lumb et al. (2002) and the one estimated from our Offset-A observation are also shown. The surface brightness quoted for Kaastra et al. (2003) was calculated using the temperature and emission measure in their Table 7 and the metal abundance from Tables 4 and 5 of Tamura et al. (2004), assuming the solar abundance ratio Fe to O (Fe/O number density ratio of 0.55; Anders & Grevesse, 1989). The surface brightness levels of the O VII or O VIII emission lines that were reported so far from the *XMM-Newton* observations are similar to or higher than that of the Galactic emission. In contrast, the upper limit of O VII line intensity in the A2218 vicinity obtained in this work is about six times lower than the Galactic level. The upper limit for O VIII is also lower than the level reported as a positive detection in other works. The tight upper limit we obtained here demonstrates the good spectral capability of the XIS, in particular below 0.5 keV.

7.3.2 Constraint on the WHIM density

If we assume that the O VII emission line is produced in a cloud with uniform density and temperature under collisional ionization equilibrium, the surface brightness I is determined by the electron density n_e, the hydrogen density n_H, path length L, and metal abundance Z of the cloud as

$$I = C(T)\ (1+z)^{-3}\ n_e n_H\ ZL, \tag{7.1}$$

where $C(T)$ is a coefficient that depends on the temperature of the cloud. Here, we will constrain the density of the cloud assuming the temperature to be $T \sim 2 \times 10^6$ K, since

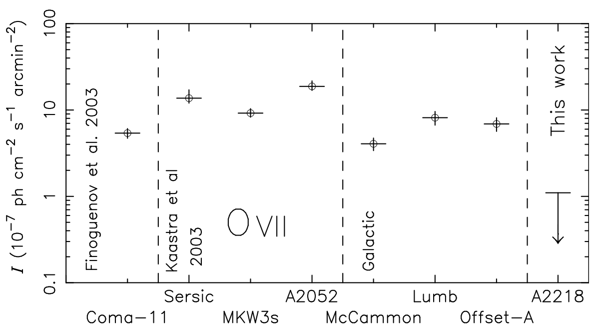

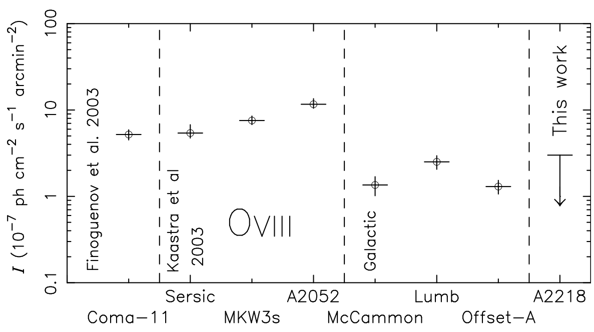

Figure 7.7: Comparison of O VII (left) and O VIII (right) surface brightness. From left to right, those in the Coma-11 field (Finoguenov et al., 2003), Sérsic 159–03, MKW 3s and A2052 (Kaastra et al., 2003), Galactic emission of McCammon et al. (2002), Lumb et al. (2002), and our Offset-A observation, and the upper limits in A2218 outskirts (this work) are plotted.

the O VII line is strongest at this temperature. Substituting $C(T = 2 \times 10^6\ \mathrm{K})$ with the value calculated with the SPEX code (Kaastra et al., 1996), our constraint, $I < 1.1 \times 10^{-7}$ photons cm^{-2} s^{-1} arcmin^{-2} at $z = 0.1756$, and electron-to-hydrogen number density ratio $n_\mathrm{e}/n_\mathrm{H} = 1.2$ for ionized gas, gives the following condition

$$n_\mathrm{H} < 7.8 \times 10^{-5}\ \mathrm{cm}^{-3} \left(\frac{Z}{0.1\ Z_\odot}\right)^{-1/2} \left(\frac{L}{2\ \mathrm{Mpc}}\right)^{-1/2}. \tag{7.2}$$

Note that $L = 2$ Mpc corresponds to $11'$, the average diameter of the annular region where we extracted the spectra. The overdensity $\delta \equiv n_\mathrm{H}/\bar{n}_\mathrm{H}$ of this cloud is

$$\delta < 270 \left(\frac{Z}{0.1\ Z_\odot}\right)^{-1/2} \left(\frac{L}{2\ \mathrm{Mpc}}\right)^{-1/2}, \tag{7.3}$$

where $\bar{n}_\mathrm{H} = X\Omega_\mathrm{b}\rho_\mathrm{crit}(1+z)^3/m_\mathrm{p} = 1.77 \times 10^{-7}\ (1+z)^3\ \mathrm{cm}^{-3}$ is the mean hydrogen density in the universe, in which $X = 0.71$ is the hydrogen-to-baryon mass ratio, $\Omega_\mathrm{b} = 0.0457$ is the baryon density of the universe, $\rho_\mathrm{crit} = 9.21 \times 10^{-30}$ g cm^{-3} is the critical density of the universe, and m_p is the proton mass. Even though this level of overdensity is much higher than the typical WHIM density ($\delta \sim 10$), it shows that Suzaku can certainly detect the high-density end of the WHIM distribution that is predicted to exist near clusters.

Chapter 8

Discussion

On the strength of our strategy of searching the cluster vicinities for the WHIM along the line of sight filament, we detected the warm-hot gas associated with the Coma cluster and the Virgo cluster. We determined for the first time the density n_{H} and the product of the abundance and the path length ZL separately for these cluster vicinities. We also set tight upper limits on the oxygen emission intensities and the overdensity in A2218 vicinity. Although we did not detect the WHIM signal in A2218 vicinity, The other two nearby clusters, for which we did emission/absorption combination analysis, show the existence of the WHIM associated with them. The observed properties such as column density, emission measure, and temprature, for the two clusters are quite similar. This suggests a kind of universality of the association of the cluster with a large amounts of warm-hot gas. The numerical simulations of large scale structure formation (Cen & Ostriker, 1999; Davé et al., 2001) also indicate that all the clusters of galaxies accompany one or more dense long WHIM filament.

In this chapter, we further discuss the properties of the WHIM by assuming their universality. We also estimate its contribution on the baryon budget and compare our result to the numerical simulations. The assumption we use here is that the properties (n_{H}, T, L, R_{WHIM}, Z, etc.) of the WHIM we observed are *typical* of the clusters; i.e., every cluster has similar WHIM in its vicinity. Of course, we had a bias in selecting clusters to observe. The assumption means that our observation bias is only on the direction of the WHIM; we observed the WHIM with typical properties but with non-typical alignment with the sight line.

8.1 Summary of the WHIM associated with the Coma and Virgo clusters

We detected a Ne IX line with 2.7σ significance in the Coma vicinity, as well as weak O VII, O VIII and Ne X lines. The combined significance was then 3.0σ. Not only the absorption, we also detected a Ne IX emission line with 3.4σ significance. The fact that both absorption and emission were detected provided us with confidence of real detection of the WHIM against statistical fluctuation. From the column density N_{NeIX} of the absorption and the surface brightness of the emission line I, we determined n_{H} and ZL as summarized in Table 8.1. With an assumption of Z, we further estimate L and M_{WHIM}. They are also shown in

Table 8.1: Properties of the WHIM and the hot gas

	Coma	Virgo
WHIM parameters obtained with this work		
$N_{\rm ion}$	4.7×10^{16} cm^{-2} ($N_{\rm NeIX}$)	6.2×10^{16} cm^{-2} ($N_{\rm OVIII}$)
$kT_{\rm WHIM}$	0.28 keV	0.21 keV
$Z\ EM$	4.1×10^{15} cm^{-5} $Z_{\rm ISM}$	1.4×10^{16} cm^{-5} $Z_{\rm ISM}$
$n_{\rm H}$	1.0×10^{-5} cm^{-3}	3.6×10^{-5} cm^{-3}
ZL	11 $Z_{\rm ISM}$Mpc	3.1 $Z_{\rm ISM}$Mpc
Cluster parameters from literature		
$kT_{\rm hot}$	8.7 keV	2.3 keV
$r_{\rm vir}$	$2.3h_{70}^{-1}$ Mpc	$1.8h_{70}^{-1}$ Mpc
$r_{\rm QSO}$	$0.74h_{70}^{-1}$ Mpc	0.45 Mpc
$M_{\rm hot}(r < r_{\rm vir})$	1.7×10^{14} $M_\odot$	5×10^{13} $M_\odot$
Parameters estimated assuming $Z = 0.2\ Z_{\rm ISM}$		
L	55 Mpc	15 Mpc
$M_{\rm WHIM}(R_{\rm WHIM} = r_{\rm QSO})$	3.3×10^{13} $M_\odot$	1.2×10^{13} $M_\odot$
$M_{\rm WHIM}(R_{\rm WHIM} = r_{\rm vir})$	3.2×10^{14} $M_\odot$	2.0×10^{14} $M_\odot$

Table 8.1.

In the Virgo vicinity, we detected an O VIII absorption line, with slightly lower significance compared to the absorption in the Coma, 96.4%. We also detected soft excess emission from thermal plasma in the spectrum of the cluster vicinity. Although the contribution of Galactic emission in the soft excess was not trivial, we estimated $n_{\rm H}$ and ZL shown in Table 8.1, by assuming that all the soft excess emission is due to the WHIM. The L and $M_{\rm WHIM}$ in the case of $Z = 0.2\ Z_{\rm ISM}$ is also tabulated.

The temperature of the WHIM was $T = 0.21$ keV for the Virgo WHIM and $T \sim 3.2 \times 10^6$ K $= 0.28$ keV for the Coma WHIM. These are higher than the temperature of the WHIM detected in others' works (e.g., Danforth & Shull, 2005; Nicastro et al., 2005b). Our study provided a unique knowledge of high-temperature WHIM. We also show the properties of the hot gas in the clusters in Table 8.1. No statistical errors are quoted in Table 8.1. See Chapter 5 and 6 for possible errors and uncertainties. Note that although the errors are not small, the simplification and assumption we use in this chapter lead comparable or larger uncertainties.

We have two unknown parameters not determined by our observations: $R_{\rm WHIM}$ and Z. On the other hand we had determined $N_{\rm ion}$, $Z\ EM$, kT, $n_{\rm H}$ and ZL of the WHIM with a combination of the observation of an absorption line and an emission line. To calculate the mass $M_{\rm WHIM}$ of the WHIM, we need the values of unknown parameters $R_{\rm WHIM}$ and Z, since $M_{\rm WHIM}$ is given by Equations (5.12) or (6.6). The dependence of $M_{\rm WHIM}$ on the unknown parameters is

$$M_{\rm WHIM} \propto R_{\rm WHIM}^2 L \propto R_{\rm WHIM}^2 Z^{-1} \propto \left(\frac{R_{\rm WHIM}}{L}\right)^2 Z^{-3}. \tag{8.1}$$

We constrain the unknown parameters by assuming universality of the WHIM properties, as shown in the following sections.

8.2 Geometry of the WHIM

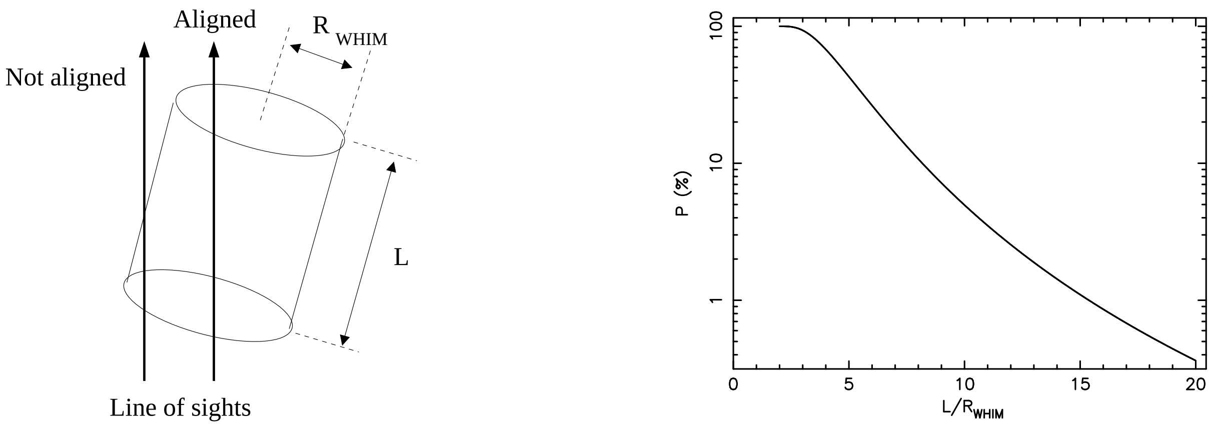

Figure 8.1: Left: schematic view of the shape of the filament. Right: P as a function of $L/R_{\rm WHIM}$.

According to a catalogue of X-ray bright clusters by Ikebe et al. (2002), there are 18 nearby ($z < 0.03$) clusters with $kT > 2$ keV (17 in their Table 1 and the Virgo cluster, which was excluded in their analysis). We know that two of them (the Coma and the Virgo cluster) indicate structure elongated in the line of sight direction, from the distribution of galaxies obtained with optical observation. We actually detected the WHIM with large column density, which strongly suggests a filament lying along the sight line. Thus we conclude that these two clusters associate an elongated filament directing our Galaxy.

The probability P that at least two clusters out of 18 have the WHIM aligned in the line-of-sight direction is given by

$$P = 1 - (1-p)^{18} - 18\,p(1-p)^{17}, \tag{8.2}$$

where p is the probability that a filament is in the line-of-sight direction, i.e., the sight line passes across both the upper and lower surface of the cylinder. The definition of alignment is schematically showed in the left panel of Figure 8.1 . When $L \gg R_{\rm WHIM}$, p is calculated to be

$$p = \frac{2\pi R_{\rm WHIM}^2}{4\pi (L/2)^2} = 2\frac{R_{\rm WHIM}^2}{L^2}. \tag{8.3}$$

The relation of $L/R_{\rm WHIM}$ and P is shown in Figure 8.1 right. Too large $L/R_{\rm WHIM}$ ratio is not likely since we did observe the filaments toward us in the two clusters. We adopt $L/R_{\rm WHIM} \lesssim 10$ as a conservative upper limit of $L/R_{\rm WHIM}$ in the later discussion. This limit corresponds to 5% probability of the alignment. The distributions of the galaxies in the Coma and Virgo clusters are ~ 5 times longer in the line-of-sight direction than the transverse direction. It suggests $L/R_{\rm WHIM} \sim 5$ if the galaxy distribution is similar to the WHIM one.

The absolute length of L and $R_{\rm WHIM}$ cannot be constrained without an assumption of Z. We take $Z < 0.5\ Z_{\rm ISM}$ conservatively, since the abundance Z is thought to be less than that of the cluster, $Z \sim 0.3\ Z_{\rm ISM}$. Assuming $Z = 0.5\ Z_{\rm ISM}$ and $L/R_{\rm WHIM} = 10$, the lower limit of L and $R_{\rm WHIM}$ of the WHIM in the Virgo vicinity are calculated to be 6.2 Mpc and 0.62 Mpc, respectively, while those in the Coma vicinity are 22 Mpc and 2.2 Mpc, respectively. Note that $r_{\rm QSO}$ of two clusters are smaller than the lower limit of $R_{\rm WHIM}$ obtained here.

The lower limit of $M_{\rm WHIM}$ can also be calculated to be $9.3\times10^{12}\ M_\odot$ and $1.1\times10^{14}\ M_\odot$, for the Virgo and the Coma, respectively, which corresponds to 28% and 65% of the hot gas mass of the cluster within $r_{\rm vir}$.

8.3 Mass and baryon budget in the warm-hot intergalactic medium in the cluster vicinities

In this section, we estimate the mass and baryon density residing in the WHIM with $T = 2-4\times10^6$ K. Since the estimate depends on Z and $R_{\rm WHIM}$ as shown in Equation (8.1), we quote two cases: $(Z, R_{\rm WHIM}) = (0.2\ Z_{\rm ISM}, r_{\rm vir})$ and $(Z, R_{\rm WHIM}) = (0.5\ Z_{\rm ISM}, L/10)$. The former and the latter can be thought to be a reasonably expected case, and a very conservative lower limit, respectively.

Table 8.2: Comparison of the baryon density

	Coma cluster		Virgo cluster	
	$Z = 0.2\ Z_{\rm ISM}$	$Z = 0.5\ Z_{\rm ISM}$	$Z = 0.2\ Z_{\rm ISM}$	$Z = 0.5\ Z_{\rm ISM}$
	$R_{\rm WHIM} = r_{\rm vir}$	$R_{\rm WHIM} = L/10$	$R_{\rm WHIM} = r_{\rm vir}$	$R_{\rm WHIM} = L/10$
$M_{\rm WHIM}$	$3.2\times10^{14}\ M_\odot$	$1.1\times10^{14}\ M_\odot$	$2.0\times10^{14}\ M_\odot$	$9.3\times10^{12}\ M_\odot$
$\Omega^a_{\rm WHIM}(2-4\times10^6\ {\rm K})$	0.56%	0.22%	0.85%	0.04%
$\Omega^b_{\rm WHIM}(2-4\times10^6\ {\rm K})$	0.71%	0.22%	0.43%	0.02%
$\Omega^c_{\rm cluster}$	$0.26^{+0.18}_{-0.12}\%$			
$\Omega_{\rm b}{}^d$	$4.57\pm0.18\%$			
$\Omega^e_{\rm WHIM}(10^{5-6}\ {\rm K})$	$0.22\pm0.03\%$			
$\Omega^f_{\rm WHIM}(\sim1.3\times10^6\ {\rm K})$	$2.7^{+3.8}_{-1.9}\%$			

^{a} : Our work; assuming the same ratio of $M_{\rm WHIM}/M_{\rm Abell}$ in all cluster vicinities.
^{b} : Our work; assuming the same mass of the WHIM in all cluster vicinities.
^{c} : Fukugita et al. (1998)
^{d}: Spergel et al. (2003)
^{e} : Danforth & Shull (2005)
^{f} : Nicastro et al. (2005b)

The baryon density in the cluster hot gas determined by Fukugita et al. (1998) is $\Omega_{\rm cluster} = 0.0026^{+0.0018}_{-0.0012}\ h_{70}^{-1}$. We can estimate the baryon density in the material of $T = 2-4\times10^6$ K from the ratio of the mass of the WHIM to that of the cluster. Fukugita et al. (1998) defined the cluster mass as the mass within a sphere of radius $2.1h_{70}^{-1}$ Mpc (the Abell radius). The mass of the hot gas $M_{\rm Abell}$ in $r < 2.1h_{70}^{-1}$ Mpc, is $M_{\rm Abell} = 6\times10^{13}\ M_\odot$ for the Virgo cluster (Schindler et al., 1999), while $M_{\rm Abell} = 1.5\times10^{14}$ Mpc for the Coma cluster (Briel et al., 1992). The baryon densities estimated from the ratios are shown in Table 8.2 as $\Omega^a_{\rm WHIM}$.

Next we estimate the baryon density assuming that all clusters connect with the WHIM of the same mass as the four cases of Table 8.2. Using the number density of clusters given by Ikebe et al. (2002), $n_{\rm cluster}(T > 2\ {\rm keV}) = 3\times10^{-6}h_{70}^3\ {\rm Mpc}^{-3}$, $\Omega_{\rm WHIM}$ is expressed as $\Omega_{\rm WHIM} = M_{\rm WHIM} n_{\rm cluster}/\rho_{\rm crit}$. The derived baryon density are shown in Table 8.2 as $\Omega^b_{\rm WHIM}$.

Table 8.2 also shows the baryon density obtained with others' works. By comparing the lowest value we obtained, $\Omega_{\rm WHIM} = 0.02\%$, to $\Omega_{\rm b}$ and $\Omega_{\rm cluster}$, we found that at least 0.5% of the baryon resides in the WHIM associated with the clusters. This baryon density corresponds to 8% of that in the clusters. Note that the *upper* limit of the amount of the WHIM in the cluster vicinities are not determined with our work.

In § 5.5.3, we estimated that $M_{\rm WHIM}$ decreases by a factor of 3 if a linear gradient of $n_{\rm H}$ is assumed. This calculation is correct if the same $R_{\rm WHIM}$ is used in the calculation like $R_{\rm WHIM} = r_{\rm vir}$. On the other hand, if we assume the same $L/R_{\rm WHIM}$ (like $R_{\rm WHIM} = L/10$), the factor is 16/27. That is, if assuming a linear gradient of $n_{\rm H}$, the lower limit of $M_{\rm WHIM}$ and $\Omega_{\rm WHIM}$ becomes 16/27 times that listed in Table 8.2.

8.4 Detection probability in the random direction

Numerical simulations predict the number of absorbers (WHIM filaments) per unit redshift. See Figure 2.7 for an example of the comparison of a simulation and an observation. In this section we estimate the probability of the detection of the WHIM associated with clusters.

When the center of a filament of the WHIM with a cylindrical distribution of radius $R_{\rm WHIM}$ and length L ($\gg R_{\rm WHIM}$) is at the distance d ($< R_{\rm WHIM}$) from the sight line, the probability that it aligns in the line of sight direction, i.e., the sight line passes across both the upper and lower surface of the cylinder, is written as

$$\frac{4\theta R_{\rm WHIM}^2 - 2R_{\rm WHIM}^2 \sin\theta\cos\theta}{4\pi(L/2)^2}, \tag{8.4}$$

where $\cos\theta = d/R_{\rm WHIM}$. The net cross section $\sigma_{\rm align}$ of an aligned filament is calculated to be

$$\sigma_{\rm align} = \frac{\pi}{2} R_{\rm WHIM}^2 \left(\frac{R_{\rm WHIM}}{L}\right)^2, \tag{8.5}$$

by integrating the probability from $d = 0$ to $d = R_{\rm WHIM}$. Then, the number of the aligned filament per unit redshift is

$$\frac{dN}{dz} = \sigma_{\rm align} n_{\rm cluster} \frac{c}{H_0} = 2.01 \times 10^{-2} \left(\frac{R_{\rm WHIM}}{1\ {\rm Mpc}}\right)^2 \left(\frac{R_{\rm WHIM}}{L}\right)^2. \tag{8.6}$$

Adopting $R_{\rm WHIM} \sim 1$ Mpc and $L/R_{\rm WHIM} \sim 10$, a conservative lower limit of dN/dz is calculated to be 2.0×10^{-4}. Even assuming that all these filaments contain both O VIII and Ne IX with a column of 6×10^{16} cm^{-2}, the derived value $dN_{\rm ion}/dz = 2.0 \times 10^{-4}$ is ~ 2 order of magnitude lower than the prediction of numerical simulations by e.g., Chen et al. (2003) or Fang et al. (2002). Note that no conflict is suggested because we have estimated only the lower limit. dN/dz may be consistent with the predicted value, because both $R_{\rm WHIM}$ and $R_{\rm WHIM}/L$ has uncertainty of a factor of ~ 3.

8.5 Comprison of observed δ to a numerical simulation

We have constrained the density of the WHIM in three cluster vicinities. Here we compare the observed overdensity δ to that from the simulation. Figure 8.2 shows a mass fraction as

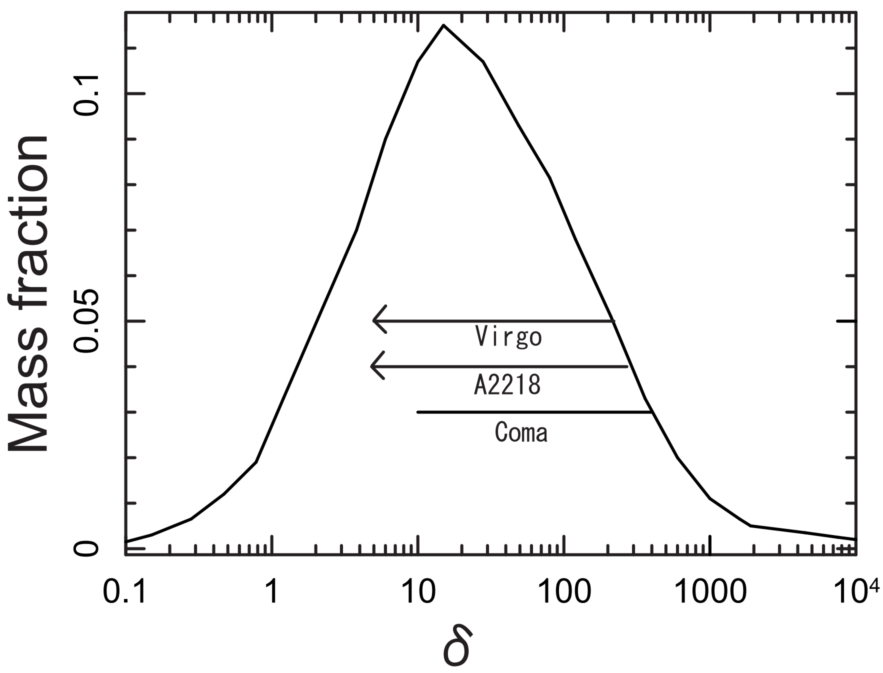

Figure 8.2: Comparison of observed δ to that from a numerical simulation (Davé et al., 2001).

a function of δ from a numerical simulation (Davé et al., 2001), overlaid with the δ obtained in this thesis. In the numerical simulation, most of the baryons resides in the region with $\delta > 10$. In the cluster vicinities, $\delta > 100$ is expected because of a deep gravitaional potential. Our constraint on the δ are $10 < \delta < 400$ in the Coma vicinity, $\delta < 220$ in Virgo, and $\delta < 270$ in A2218. Thus, the sensitivity of this work covers the expected range in cluster vicinities. We demonstrated that the WHIM in cluster vicinities can be studied in this manner. It is well expected that when similar works are extended, we can constrain cosmology models from the observations.

8.6 Summary

Many properties of the WHIM in the cluster vicinities were estimated in this work. We determined $N_{\rm ion}$, $Z\ EM$, T with the observations, constrained $n_{\rm H}$ and ZL with an assumption of a uniform distribution, and estimated Z, L, $M_{\rm WHIM}$ $\Omega_{\rm WHIM}$, dN/dz assuming universality of the properties. All of these values are consistent with the predictions of numerical simulations. The limits in the determination of parameters are mostly due to the low statistics of the obtained data and the small number of the clusters we can observe with the existent detectors. We, despite these difficulties, observationally estimated $n_{\rm H}$, Z and L for the first time. This work demonstrated that the sensitivity of such a study has enough sensitivity to constrain overdensity δ in cluster vicinities. We also showed a non-negligible WHIM in the cluster vicinities and demonstrated the capability and the effectiveness of the combination of absorption and emission for the study of the WHIM.

Chapter 9

Conclusion

We studied the WHIM in vicinities of three clusters that are thought to have elongated structure in the line of sight direction: the Coma cluster, the Virgo cluster and A2218. On the strength of our strategy, absorption and emission lines probably due to the WHIM were detected in the Coma and Virgo vicinities. A Ne IX absorption line with 2.7σ significance was detected in the Coma vicinity, as well as weak O VII, O VIII and Ne X lines. The combined significance was then 3.0σ. Not only the absorption, we also detected a Ne IX emission line with 3.4σ significance. We obtained $N_{\rm NeIX} = 4.7^{+2.6}_{-2.9} \times 10^{16}$ cm^{-2} and $Z\ EM = 4.1 \pm 2.0 \times 10^{15}$ cm^{-5} $Z_{\rm ISM}$, assuming that the absorption was not saturated. In the Virgo vicinity, we detected an O VIII absorption line with 96.4% significance. Soft excess emission from thermal plasma was also detected. Although the contribution of Galactic emission in the soft excess was not trivial, we determined $N_{\rm OVIII} = 6.2^{+3.3}_{-4.4} \times 10^{16}$ cm^{-2} and $Z\ EM = 1.4 \pm 0.2 \times 10^{16}$ cm^{-5} $Z_{\rm ISM}$, assuming that the absorption was not saturated and that all excess emission originated in the WHIM. The detection of both absorption and emission lines ensures our detection of warm-hot gas, not the statistical fluctuations. We set tight upper limits on O VII and O VIII line intensities and overdensity δ in A2218 vicinity.

We also showed the capability of studying the cluster vicinities for constraining the physical properties of the WHIM; the WHIM of higher temperature can be studied than that detected in others' works, and detection of both emission and absorption lines are expected. Combining absorption and emission lines allows us to constrain the parameters that are degenerate in either absorption or emission line intensity. We determined the properties of the WHIM associated with the Coma and Virgo clusters assuming a uniform distribution as follows (errors are quoted at 1σ confidence level):

- kT
  0.28 keV (0.17–0.51 keV) for the Coma and 0.21 ± 0.01 keV for the Virgo, determined from the ratio between absorption or emission line intensity of different ions.

- $n_{\rm H}$
  $0.2 - 8.0 \times 10^{-5}$ cm^{-3} for the Coma and $3.6^{+2.8}_{-0.9} \times 10^{-5}$ cm^{-3} for the Virgo.

- ZL
  $0.7 - 300$ $Z_{\rm ISM}$ Mpc for the Coma and $3.1^{+2.3}_{-2.1}$ $Z_{\rm ISM}$ Mpc for the Virgo.

These parameters are consistent with the predictions of numerical simulations. The similarity of the WHIM around the Coma and the Virgo supports our idea that all clusters associate with the WHIM of similar properties. Assuming that the detected WHIM is typical for clusters, we further estimated the physical properties of the WHIM:

- $L/R_{\rm WHIM} \lesssim 10$
  There are 18 clusters in $z < 0.03$ with $T > 2$ keV. The probability that at least two out of 18 filaments aligns the line of sight is less than 5% if $L/R_{\rm WHIM} \gtrsim 10$.

- $L \gtrsim 6$ Mpc; $R_{\rm WHIM} \gtrsim 0.6$ Mpc; $M_{\rm WHIM} \gtrsim 9.3 \times 10^{12}\ M_{\odot}$; $\Omega_{\rm WHIM} \gtrsim 0.02\%$
  By assuming $Z \lesssim 0.5\ Z_{\rm ISM}$, where $0.5\ Z_{\rm ISM}$ corresponds to the abundance in the cluster.

In summary, we constrained $n_{\rm H}$, L, and Z, from the observation for the first time. This work is also the first study of the WHIM with $T > 0.2$ keV. Although the constraint we obtained was too loose to restrict the predictions of numerical simulations, our work is still important and suggestive in demonstrating the capability and effectiveness of the study of cluster vicinities and the combination of absorption and emission.

Bibliography

Anders, E., & Grevesse, N. 1989, Geochimica et Cosmochimica Acta, 53, 197

Antia, H. M., & Basu, S. 2005, ApJ, 620, L129

Asplund, M., Grevesse, N., & Sauval, A. J. 2005, in ASP Conf. Ser. 336: Cosmic Abundances as Records of Stellar Evolution and Nucleosynthesis, 25–+

Böhringer, H., Briel, U. G., Schwarz, R. A., Voges, W., Hartner, G., & Trumper, J. 1994, Nature, 368, 828

Bonamente, M., Lieu, R., & Joy, Marshall K.and Nevalainen, J. H. 2002, ApJ, 576, 688

Branduardi-Raymont, G., Mason, K. O., Murdin, P. G., & Martin, C. 1985, MNRAS, 216, 1043

Briel, U. G., Henry, J. P., & Boehringer, H. 1992, A&A, 259, L31

Bristow, P. D., & Phillipps, S. 1994, MNRAS, 267, 13

Burles, S., Nollett, K. M., & Turner, M. S. 2001, ApJ, 552, L1

Cash, W. 1979, ApJ, 228, 939

Cen, R., & Ostriker, J. P. 1999, ApJ, 514, 1

Chen, X., Weinberg, D. H., Katz, N., & Davé, R. 2003, ApJ, 594, 42

Cheng, L.-M., Borgani, S., Tozzi, P., Tornatore, L., Diaferio, A., Dolag, K., He, X.-T., Moscardini, L., Murante, G., & Tormen, G. 2005, A&A, 431, 405

Colless, M., & Dunn, A. M. 1996, ApJ, 458, 435

Cowie, L. L., & McKee, C. F. 1977, ApJ, 211, 135

Cox, D. P. 2005, Annual Rev. A&A, 43, 337

Danforth, C. W., & Shull, J. M. 2005, ApJ, 624, 555

Davé, R., Cen, R., Ostriker, J. P., Bryan, G. L., Hernquist, L., Katz, N., Weinberg, D. H., Norman, M. L., & O'Shea, B. 2001, ApJ, 552, 473 den Herder, J. W., Brinkman, A. C., Kahn, S. M., Branduardi-Raymont, G., Thomsen, K., Aarts, H., Audard, M., Bixler, J. V., den Boggende, A. J., Cottam, J., Decker, T., Dubbeldam, L., Erd, C., Goulooze, H., Güdel, M., Guttridge, P., Hailey, C. J., Janabi, K. A., Kaastra, J. S., de Korte, P. A. J., van Leeuwen, B. J., Mauche, C., McCalden, A. J., Mewe, R., Naber, A., Paerels, F. B., Peterson, J. R., Rasmussen, A. P., Rees, K., Sakelliou, I., Sako, M., Spodek, J., Stern, M., Tamura, T., Tandy, J., de Vries, C. P., Welch, S., & Zehnder, A. 2001, A&A, 365, L7

Dickey, J. M., & Lockman, F. J. 1990, ARAA, 28, 215

Drake, J. J., & Testa, P. 2005, Nature, 436, 525

Fabian, A. C. 1997, Science, 275, 48

Fang, T., Bryan, G. L., & Canizares, C. R. 2002, ApJ, 564, 604

Fang, T., Marshall, H. L., Lee, J. C., Davis, D. S., & Canizares, C. R. 2002, ApJ, 572, L127

Ferrière, K. M. 2001, Reviews of Modern Physics, 73, 1031

Finoguenov, A., Briel, U. G., & Henry, J. P. 2003, A&A, 410, 777

Fouqué, P., Solanes, J. M., Sanchis, T., & Balkowski, C. 2001, A&A, 375, 770

Fujimoto, R., Takei, Y., Tamura, T., Mitsuda, K., Yamasaki, N. Y., Shibata, R., Ohashi, T., Ota, N., Audley, M. D., Kelley, R. L., & Kilbourne, C. A. 2004, PASJ, 56, L29

Fukugita, M., Hogan, C. J., & Peebles, P. J. E. 1998, ApJ, 503, 518

Futamoto, K., Mitsuda, K., Takei, Y., Fujimoto, R., & Yamasaki, N. Y. 2004, ApJ, 605, 793

Gavazzi, G., Boselli, A., Scodeggio, M., Pierini, D., & Belsole, E. 1999, MNRAS, 304, 595

Gavazzi, G., O'Neil, K., Boselli, A., & van Driel, W. 2006, A&A, 449, 929

Gehrels, N., & Williams, E. D. 1993, ApJ, 418, L25+

Girardi, M., Fadda, D., Escalera, E., Giuricin, G., Mardirossian, F., & Mezzetti, M. 1997, ApJ, 490, 56

Girardi, M., Giuricin, G., Mardirossian, F., Mezzetti, M., & Boschin, W. 1998, ApJ, 505, 74

Grevesse, N., & Sauval, A. J. 1998, Space Science Reviews, 85, 161

Hewett, P. C., Foltz, C. B., & Chaffee, F. H. 1995, AJ, 109, 1498

Holweger, H. 2001, in AIP Conf. Proc. 598: Joint SOHO/ACE workshop "Solar and Galactic Composition", 23–+

Honda, H., Hirayama, M., Watanabe, M., Kunieda, H., Tawara, Y., Yamashita, K., Ohashi, T., Hughes, J. P., & Henry, J. P. 1996, ApJ, 473, L71+

Hwang, C.-Y. 1997, Science, 278, 1917

Ikebe, Y., Reiprich, T. H., Böhringer, H., Tanaka, Y., & Kitayama, T. 2002, A&A, 383, 773

Inoue, H., Koyama, K., Matsuoka, M., Ohashi, T., Tanaka, Y., & Tsunemi, H. 1979, ApJ, 227, L85

Irwin, J. A., & Sarazin, C. L. 1996, ApJ, 471, 683

Jansen, F., Lumb, D., Altieri, B., Clavel, J., Ehle, M., Erd, C., Gabriel, C., Guainazzi, M., Gondoin, P., Much, R., Munoz, R., Santos, M., Schartel, N., Texier, D., & Vacanti, G. 2001, A&A, 365, L1

Kaastra, J. S., Lieu, R., Tamura, T., Paerels, F. B. S., & den Herder, J. W. 2003, A&A, 397, 445

Kaastra, J. S., Mewe, R., & Nieuwenhuijzen, H. 1996, in UV and X-ray Spectroscopy of Astrophysical and Laboratory Plasmas : Proceedings of the Eleventh Colloquium on UV and X-ray ... held on May 29-June 2, 1995, Nagoya, Japan. Edited by K. Yamashita and T. Watanabe. Tokyo : Universal Academy Press, 1996. (Frontiers science series ; no. 15)., p.411, ed. K. Yamashita & T. Watanabe, 411–+

Kaastra, J. S., Werner, N., Herder, J. W. A. d., Paerels, F. B. S., de Plaa, J., Rasmussen, A. P., & de Vries, C. P. 2006, ApJ, 652, 189

Krolik, J. H., & Raymond, J. C. 1988, ApJ, 335, L39

Kushino, A., Ishisaki, Y., Morita, U., Yamasaki, N. Y., Ishida, M., Ohashi, T., & Ueda, Y. 2002, PASJ, 54, 327

Lieu, R., Mittaz, J. P. D., Bowyer, S., Breen, J. O., Lockman, F. J., Murphy, E. M., & Hwang, C.-Y. 1996, Science, 274, 1335

Lieu, R., Mittaz, J. P. D., Bowyer, S., Lockman, F. J., Hwang, C.-Y., & Schmitt, J. H. M. M. 1996, ApJ, 458, L5+

Lumb, D. H., Warwick, R. S., Page, M., & De Luca, A. 2002, A&A, 389, 93

Machacek, M. E., Bautz, M. W., Canizares, C., & Garmire, G. P. 2002, ApJ, 567, 188

Matsumoto, H. 1998, Ph.D. Thesis

Mazzotta, P., Mazzitelli, G., Colafrancesco, S., & Vittorio, N. 1998, A&AS, 133, 403

McCammon, D., Almy, R., Apodaca, E., Bergmann Tiest, W., Cui, W., Deiker, S., Galeazzi, M., Juda, M., Lesser, A., Mihara, T., Morgenthaler, J. P., Sanders, W. T., Zhang, J., Figueroa-Feliciano, E., Kelley, R. L., Moseley, S. H., Mushotzky, R. F., Porter, F. S., Stahle, C. K., & Szymkowiak, A. E. 2002, ApJ, 576, 188

McCammon, D., & Sanders, W. T. 1990, Annual Rev. A&A, 28, 657

McWhirter, R. W. P. 1965, Plasma diagnostic techniques, ed. R. H. Huddlestone & S. L. Leonard (Newyork, London: Academic press)

Mewe, R., Gronenschild, E. H. B. M., & van den Oord, G. H. J. 1985, A&AS, 62, 197

Mittaz, J. P. D., Lieu, R., & Lockman, F. J. 1998, ApJ, 498, L17+

Neumann, D. M., Lumb, D. H., Pratt, G. W., & Briel, U. G. 2003, A&A, 400, 811

Nicastro, F., Elvis, M., Fiore, F., & Mathur, S. 2005a, Advances in Space Research, 36, 721

Nicastro, F., Mathur, S., Elvis, M., Drake, J., Fang, T., Fruscione, A., Krongold, Y., Marshall, H., Williams, R., & Zezas, A. 2005b, Nature, 433, 495

Nicastro, F., Mathur, S., Elvis, M., Drake, J., Fiore, F., Fang, T., Fruscione, A., Krongold, Y., Marshall, H., & Williams, R. 2005c, ApJ, 629, 700

Nicastro, F., Zezas, A., Drake, J., Elvis, M., Fiore, F., Fruscione, A., Marengo, M., Mathur, S., & Bianchi, S. 2002, ApJ, 573, 157

Persic, M., & Salucci, P. 1992, MNRAS, 258, 14

Peterson, J. R., Kahn, S. M., Paerels, F. B. S., Kaastra, J. S., Tamura, T., Bleeker, J. A. M., Ferrigno, C., & Jernigan, J. G. 2003, ApJ, 590, 207

Pratt, G. W., Böhringer, H., & Finoguenov, A. 2005, A&A, 433, 777

Rasmussen, A. P., Kahn, S. M., Paerels, F., Herder, J. W. d., Kaastra, J., & de Vries, C. 2007, ApJ, 656, 129

Rauch, M., Miralda-Escude, J., Sargent, W. L. W., Barlow, T. A., Weinberg, D. H., Hernquist, L., Katz, N., Cen, R., & Ostriker, J. P. 1997, ApJ, 489, 7

Rees, M. J. 1992, in NATO ASIC Proc. 366: Clusters and Superclusters of Galaxies, 1–10

Sarazin, C. L. 1989, ApJ, 345, 12

Savage, B. D., & Sembach, K. R. 1996, Annual Rev. A&A, 34, 279

Schindler, S., Binggeli, B., & Böhringer, H. 1999, A&A, 343, 420

Shibata, R., Matsushita, K., Yamasaki, N. Y., Ohashi, T., Ishida, M., Kikuchi, K., Böhringer, H., & Matsumoto, H. 2001, ApJ, 549, 228

Smith, G. P., Kneib, J.-P., Smail, I., Mazzotta, P., Ebeling, H., & Czoske, O. 2005, MNRAS, 359, 417

Snow, T. P., & Witt, A. N. 1996, ApJ, 468, L65+

Snowden, S. L., Egger, R., Finkbeiner, D. P., Freyberg, M. J., & Plucinsky, P. P. 1998, ApJ, 493, 715

Snowden, S. L., Egger, R., Freyberg, M. J., McCammon, D., Plucinsky, P. P., Sanders, W. T., Schmitt, J. H. M. M., Truemper, J., & Voges, W. 1997, ApJ, 485, 125

Snowden, S. L., Freyberg, M. J., Plucinsky, P. P., Schmitt, J. H. M. M., Truemper, J., Voges, W., Edgar, R. J., McCammon, D., & Sanders, W. T. 1995, ApJ, 454, 643

Solanes, J. M., Sanchis, T., Salvador-Solé, E., Giovanelli, R., & Haynes, M. P. 2002, AJ, 124, 2440

Spergel, D. N., Verde, L., Peiris, H. V., Komatsu, E., Nolta, M. R., Bennett, C. L., Halpern, M., Hinshaw, G., Jarosik, N., Kogut, A., Limon, M., Meyer, S. S., Page, L., Tucker, G. S., Weiland, J. L., Wollack, E., & Wright, E. L. 2003, ApJS, 148, 175

Struble, M. F., & Rood, H. J. 1999, ApJS, 125, 35

Strüder, L., Briel, U., Dennerl, K., Hartmann, R., Kendziorra, E., Meidinger, N., Pfeffermann, E., Reppin, C., Aschenbach, B., Bornemann, W., Bräuninger, H., Burkert, W., Elender, M., Freyberg, M., Haberl, F., Hartner, G., Heuschmann, F., Hippmann, H., Kastelic, E., Kemmer, S., Kettenring, G., Kink, W., Krause, N., Müller, S., Oppitz, A., Pietsch, W., Popp, M., Predehl, P., Read, A., Stephan, K. H., Stötter, D., Trümper, J., Holl, P., Kemmer, J., Soltau, H., Stötter, R., Weber, U., Weichert, U., von Zanthier, C., Carathanassis, D., Lutz, G., Richter, R. H., Solc, P., Böttcher, H., Kuster, M., Staubert, R., Abbey, A., Holland, A., Turner, M., Balasini, M., Bignami, G. F., La Palombara, N., Villa, G., Buttler, W., Gianini, F., Lainé, R., Lumb, D., & Dhez, P. 2001, A&A, 365, L18

Takei, Y., Fujimoto, R., Mitsuda, K., & Onaka, T. 2002, ApJ, 581, 307

Tamura, T., Kaastra, J. S., den Herder, J. W. A., Bleeker, J. A. M., & Peterson, J. R. 2004, A&A, 420, 135

Tanaka, Y., & Bleeker, J. A. M. 1977, Space Science Reviews, 20, 815

Tripp, T. M., Savage, B. D., & Jenkins, E. B. 2000, ApJ, 534, L1

Turner, M. J. L., Abbey, A., Arnaud, M., Balasini, M., Barbera, M., Belsole, E., Bennie, P. J., Bernard, J. P., Bignami, G. F., Boer, M., Briel, U., Butler, I., Cara, C., Chabaud, C., Cole, R., Collura, A., Conte, M., Cros, A., Denby, M., Dhez, P., Di Coco, G., Dowson, J., Ferrando, P., Ghizzardi, S., Gianotti, F., Goodall, C. V., Gretton, L., Griffiths, R. G., Hainaut, O., Hochedez, J. F., Holland, A. D., Jourdain, E., Kendziorra, E., Lagostina, A., Laine, R., La Palombara, N., Lortholary, M., Lumb, D., Marty, P., Molendi, S., Pigot, C., Poindron, E., Pounds, K. A., Reeves, J. N., Reppin, C., Rothenflug, R., Salvetat, P., Sauvageot, J. L., Schmitt, D., Sembay, S., Short, A. D. T., Spragg, J., Stephen, J., Strüder, L., Tiengo, A., Trifoglio, M., Trümper, J., Vercellone, S., Vigroux, L., Villa, G., Ward, M. J., Whitehead, S., & Zonca, E. 2001, A&A, 365, L27

Verner, D. A., Verner, E. M., & Ferland, G. J. 1996, Atomic Data and Nuclear Data Tables, 64, 1

Voges, W., Aschenbach, B., Boller, T., Bräuninger, H., Briel, U., Burkert, W., Dennerl, K., Englhauser, J., Gruber, R., Haberl, F., Hartner, G., Hasinger, G., Kürster, M., Pfeffermann, E., Pietsch, W., Predehl, P., Rosso, C., Schmitt, J. H. M. M., Trümper, J., & Zimmermann, H. U. 1999, A&A, 349, 389

Watanabe, M., Yamashita, K., Furuzawa, A., Kunieda, H., Tawara, Y., & Honda, H. 1999, ApJ, 527, 80

White, D. A. 2000, MNRAS, 312, 663

Yao, Y., & Wang, Q. D. 2005, ApJ, 624, 751

Yasuda, N., Fukugita, M., & Okamura, S. 1997, ApJS, 108, 417

Yoshida, N., Furlanetto, S. R., & Hernquist, L. 2005, ApJ, 618, L91